

**Numerical solution of the Non-equilibrium Boltzmann Equation
using the Discontinuous Galerkin Finite Element method**

*Submitted in partial fulfillment of the requirements for
the degree of
Doctor of Philosophy
in
Computational Mechanics*

Arnab Debnath

B.Tech., Civil Engineering, Indian Institute of Technology, Kharagpur
M.S., Civil Engineering, Carnegie Mellon University

Carnegie Mellon University
Pittsburgh, PA

December, 2018

Acknowledgements

Firstly, I would like to express my sincere gratitude to my advisor Prof. Kaushik Dayal for the continuous support of my Ph.D. study, for his patience and motivation and encouragement which has allowed me to grow as a research scientist, over the past five years. His guidance helped me in all the time of research and answer my questions.

I am grateful to Prof. Carmel Majidi, Prof. Matteo Pozzi and Dr. Yang Wang for taking out time to review my research work and serving on my thesis committee.

I would like to thank my current and former colleagues Hossein, Vaibhav, Prashant, Mahnoush, Matthew, Sabyasachi, Rajat, Ankit, Kshiteej and Shoham for holding technical discussions on a regular basis which cleared a lot of my doubts. The group meetings that are held every week to discuss research related topics of the different members in our group has been one of the enriching times I have spent in CMU. I am again thankful to my advisor for organizing these meetings. They have helped me to look into different realms of the field of Computational Mechanics with a wider view.

Had it not been some great friendships that I have made over the past few years, life would have become monotonous in Pittsburgh. I would like to thank my friends Devdutta, Ajay, Purvasha, Dipan, Sidzoo, Vaishnavh, Devansh, Saurabh, Satwik and Rithisha for all their support.

I thank the U.S. Army (ARMY: W911NF-17-1-0084), Air Force Office of Scientific Research (AFOSR: N00014-16-R FO05) and the National Science Foundation (NSF CAREER: 1150002-NSF) for the financial support to conduct this research work. But for the computational resource provided the Pittsburgh Supercomputing Center it would not have been possible to perform these computations.

Last but not the least, it would not have been possible to push through this period of rigorous research and hardship without the blessings of my parents and the continuous support of my brother.

Abstract

In this thesis, we describe a deterministic method of solving a four-dimensional reduced form of the spatially homogeneous non-equilibrium Boltzmann Equation from its original seven-dimensional form. We have used Discontinuous Galerkin discretization to seek solution in the velocity space for different kinds of affine and viscometric fluid flows given by the macroscopic Eulerian velocity field $\mathbf{v}(\mathbf{x}, t) = \mathbf{A}(\mathbf{I} + t\mathbf{A})^{-1}\mathbf{x}$ [15]. The symmetry properties of the Collision operator, the uniformity of our mesh and the construction of our nodal DG basis on Gauss-quadrature nodes have reduced the calculation of the collision kernel to $O(n^5)$, as shown by Josyula *et al.*[3], which has made it possible for us to look into non-equilibrium Boltzmann equation. In this method the collision operator is pre-computed and it is used to observe the evolution of the velocity distribution function for different kinds of flows including Couette flow, incompressible vortex-like structures. The computation of the Collision operator was parallelized using 351 processors with OpenMP API. The simulations run in this work are based on spatially homogeneous hard-sphere potentials although this method is generalized for any molecular potential. We have compared the predictions of all our simulations of the Boltzmann Equation with non-equilibrium molecular dynamics (NEMD).

Keywords: Non-equilibrium Boltzmann equation, Deterministic solution, Viscometric Flow, Discontinuous Galerkin methods, LAMMPS, Molecular Dynamics

Contents

Acknowledgement	ii
Abstract	iii
List of Figures	vi
1 Introduction	1
1.1 Why Boltzmann Equation?	3
1.2 The Boltzmann Equation	5
1.2.1 Binary Collisions	7
1.3 Why Discontinuous Galerkin Method?	11
2 Objective Molecular Dynamics and its Ansatz in Boltzmann Equation	14
2.1 Objective Structures	14
2.2 Isometry groups	16
2.3 Objective Molecular Dynamics	18
2.4 Viscometric Flows	20
2.5 Ansatz in Boltzmann Equation	21
2.6 Non-dimensionalization of the governing equation	23
3 Numerical Solution of The Boltzmann Equation using DG Method	25
3.1 The Discontinuous Galerkin Method	25
3.2 Discontinuous Galerkin velocity discretization	28
3.3 Numerical Approximation	29
3.3.1 Discrete Velocity discretization of the Collision operator	29

3.3.2	Time Discretization	34
3.4	Conservation Routines	35
4	Verification Results	38
4.1	Spatially homogeneous relaxation	38
4.1.1	Experiment 1	40
4.1.2	Experiment 2	48
4.2	Method of Manufactured Solution	56
4.2.1	Manufactured Solution for the reduced Boltzmann equation	57
5	Results and Discussion	61
5.1	Non-equilibrium flows	61
5.2	Simple Shear	62
5.3	Pressure Shear	74
5.4	Simple bi-directional Shear	83
5.5	Vortex-like Structure	93
5.6	Parallelization Scaling	102
5.7	Discussion	104
6	Appendix	106
6.1	Symmetry property of The Collision Operator	106
6.2	Notation	109

List of Figures

1.1	Molecule Scattering. (adapted from [25])	8
2.1	Extended (left) and contracted (right) tail sheath of bacteriophage T4. (from [27])	15
2.2	Illustration of the four groups in (2.2.0.3). The pictures are obtained by applying each of the groups to a single sphere. Coloring scheme is according to the powers of group elements, as noted. Group parameters conveniently chosen. (a) G_1 : all atoms blue; (b) G_2 : $m = 1$ red; $m = 2$ blue; (c) G_3 : $n = 6$; shading proportional to q ; (d) G_4 : $n = 6$; $m = 1$ green; $m = 2$ red/blue, shading proportional to q . (from [14])	17
4.1	Validation Experiment 1 with 27 elements: Evolution of g with $w_2 = w_3 = 0$	40
4.2	Validation Experiment 1 with 27 elements: Evolution of g with $w_1 = w_3 = 0$	41
4.3	Validation Experiment 1 with 27 elements: Evolution of g with $w_1 = w_2 = 0$	41
4.4	Validation Experiment 1 with 27 elements: Number Density	42
4.5	Validation Experiment 1 with 27 elements: Energy	42
4.6	Validation Experiment 1 with 27 elements: Input and output on different surfaces	43
4.7	Validation Experiment 1 with 125 elements: Evolution of g with $w_2 = w_3 = 0$	44
4.8	Validation Experiment 1 with 125 elements: Evolution of g with $w_1 = w_3 = 0$	44
4.9	Validation Experiment 1 with 125 elements: Evolution of g with $w_1 = w_2 = 0$	45
4.10	Validation Experiment 1 with 125 elements: Number Density	45
4.11	Validation Experiment 1 with 125 elements: Energy	46
4.12	Validation Experiment 1 with 125 elements: Input and output on different surfaces	47
4.13	Validation Experiment 2 with 27 elements: Evolution of g with $w_2 = w_3 = 0$	48
4.14	Validation Experiment 2 with 27 elements: Evolution of g with $w_1 = w_3 = 0$	49
4.15	Validation Experiment 2 with 27 elements: Evolution of g with $w_1 = w_2 = 0$	49
4.16	Validation Experiment 2 with 27 elements: Number Density	50
4.17	Validation Experiment 2 with 27 elements: Energy	50

4.18	Validation Experiment 2 with 27 elements: Input and output on different surfaces	51
4.19	Validation Experiment 2 with 125 elements: Evolution of g with $w_2 = w_3 = 0$	52
4.20	Validation Experiment 2 with 125 elements: Evolution of g with $w_1 = w_3 = 0$	52
4.21	Validation Experiment 2 with 125 elements: Evolution of g with $w_1 = w_2 = 0$	53
4.22	Validation Experiment 2 with 125 elements: Number Density	53
4.23	Validation Experiment 2 with 125 elements: Energy	54
4.24	Validation Experiment 2 with 125 elements: Input and output on different surfaces . .	55
4.25	Manufactured solution experiment: Solution at 100000 iterations	58
4.26	Manufactured solution experiment: Solution at 120000 iterations	58
4.27	Manufactured solution experiment: Solution at 140000 iterations	59
4.28	Manufactured solution experiment: Solution at 160000 iterations	59
4.29	Manufactured solution experiment: Error at regular time intervals	60
5.1	Experiment 1 with 27 Elements: Evolution of g with $w_2 = w_3 = 0$	62
5.2	Experiment 1 with 27 Elements: Evolution of g with $w_1 = w_3 = 0$	63
5.3	Experiment 1 with 27 Elements: Evolution of g with $w_1 = w_2 = 0$	63
5.4	Experiment 1 with 27 Elements: Number Density	64
5.5	Experiment 1 with 27 Elements: Energy	64
5.6	Experiment 1 with 27 Elements: Input and output on different surfaces	65
5.7	Experiment 1 with 125 Elements: Evolution of g with $w_2 = w_3 = 0$	66
5.8	Experiment 1 with 125 Elements: Evolution of g with $w_1 = w_3 = 0$	66
5.9	Experiment 1 with 125 Elements: Evolution of g with $w_1 = w_2 = 0$	67
5.10	Experiment 1 with 125 Elements: Number Density	67
5.11	Experiment 1 with 125 Elements: Energy	68
5.12	Experiment 1 with 125 Elements: Input and output on different surfaces	69
5.13	Experiment 1 in LAMMPS: Input and output on different surfaces	70
5.14	Temperature comparison of Boltzmann with molecular dynamics	71
5.15	Temperature comparison of Boltzmann with molecular dynamics with 2 different densities	72
5.16	Temperature comparison of Boltzmann with molecular dynamics with different box sizes	73

5.17 Schematic pressure-shear viscometer: vectors a and n as in the text. The leading edge of plate 1 moves at constant velocity in the direction a towards plate 2, which is stationary. Both plates are in general oblique to the velocity as shown. (from Dayal & James [15]) 74

5.18 Experiment 4 with 27 Elements: Evolution of g with $w_2 = w_3 = 0$ 75

5.19 Experiment 4 with 27 Elements: Evolution of g with $w_1 = w_3 = 0$ 75

5.20 Experiment 4 with 27 Elements: Evolution of g with $w_1 = w_2 = 0$ 76

5.21 Experiment 4 with 27 Elements: Number Density 76

5.22 Experiment 4 with 27 Elements: Energy 77

5.23 Experiment 4 with 27 Elements: Input and output on different surfaces 78

5.24 Experiment 4 with 125 Elements: Evolution of g with $w_2 = w_3 = 0$ 79

5.25 Experiment 4 with 125 Elements: Evolution of g with $w_1 = w_3 = 0$ 79

5.26 Experiment 4 with 125 Elements: Evolution of g with $w_1 = w_2 = 0$ 80

5.27 Experiment 4 with 125 Elements: Number Density 80

5.28 Experiment 4 with 125 Elements: Energy 81

5.29 Experiment 4 with 125 Elements: Input and output on different surfaces 82

5.30 Universal flow of the unit cube having outer normals I_1, I_2, I_3 . The values of the parameters are $\alpha = 1.4, v_1 = 0.9, v_3 = 0.7$. The figure shows the same set of material particles at successive instants of time. Time between pictures is 0.5 in consistent units. (from Dayal & James[15]) 83

5.31 Motion of the two planes with normal I_3 with parameters chosen as in Figure 5.30. Time between pictures is 0.2 in consistent units. (from Dayal & James[15]) 83

5.32 Experiment 2 with 27 Elements: Evolution of g with $w_2 = w_3 = 0$ 85

5.33 Experiment 2 with 27 Elements: Evolution of g with $w_1 = w_3 = 0$ 85

5.34 Experiment 2 with 27 Elements: Evolution of g with $w_1 = w_2 = 0$ 86

5.35 Experiment 2 with 27 Elements: Number Density 86

5.36 Experiment 2 with 27 Elements: Energy 87

5.37 Experiment 2 with 27 Elements: Input and output on different surfaces 88

5.38 Experiment 2 with 125 Elements: Evolution of g with $w_2 = w_3 = 0$ 89

5.39 Experiment 2 with 125 Elements: Evolution of g with $w_1 = w_3 = 0$ 89

5.40 Experiment 2 with 125 Elements: Evolution of g with $w_1 = w_2 = 0$ 90

5.41 Experiment 2 with 125 Elements: Number Density 90

5.42 Experiment 2 with 125 Elements: Energy 91

5.43 Experiment 2 with 125 Elements: Input and output on different surfaces 92

5.44 Vortex like structures. The values of the parameters are $\alpha = -1.3, v_1 = 1.3, v_3 = 0.7$. The velocity field on the plane $x_2 = cst.$ is shown, and this velocity field is independent of x_2 . The line perpendicular to this plane passing through the centre of this structure is a line of zero velocity. (from Dayal & James[15]) 93

5.45 Experiment 3 with 27 Elements: Evolution of g with $w_2 = w_3 = 0$ 94

5.46 Experiment 3 with 27 Elements: Evolution of g with $w_1 = w_3 = 0$ 94

5.47 Experiment 3 with 27 Elements: Evolution of g with $w_1 = w_2 = 0$ 95

5.48 Experiment 3 with 27 Elements: Number Density 95

5.49 Experiment 3 with 27 Elements: Energy 96

5.50 Experiment 3 with 27 Elements: Input and output on different surfaces 97

5.51 Experiment 3 with 125 Elements: Evolution of g with $w_2 = w_3 = 0$ 98

5.52 Experiment 3 with 125 Elements: Evolution of g with $w_1 = w_3 = 0$ 98

5.53 Experiment 3 with 125 Elements: Evolution of g with $w_1 = w_2 = 0$ 99

5.54 Experiment 3 with 125 Elements: Number Density 99

5.55 Experiment 3 with 125 Elements: Energy 100

5.56 Experiment 3 with 125 Elements: Input and output on different surfaces 101

5.57 Efficiency 102

5.58 Speed Up 103

Chapter 1

Introduction

The idea of observing physical properties of gases with the statistics of molecules was brought about by the Austrian physicist, Ludwig Boltzmann in the mid-nineteenth century. His belief, that tracking every particle and studying their trajectories later on to observe physical properties of gases is not very useful, gave birth to a new field of study in Physics, known as *Statistical Mechanics*. He explained how the physical properties of molecules like mass, charge, and structure describe the physical properties of matter. In 1872, Boltzmann devised the revolutionary transport equation describing the transient behaviors of gas from its statistics.

In the Kinetic theory of gases, the Boltzmann equation describes the evolution of a *molecular density function* describing the behavior of a gas because of external forces and collisions among the particles for very dilute gases. It describes the macroscopic states of a gas or a mixture of gases by taking into consideration the microscopic probabilistic representation of the gas which is a space and time-dependent velocity distribution function. Due to the interactions, according to known potentials, among the particles, the velocity distribution evolves with time which is modeled by a five-dimensional integral known as the collision operator. The complex nature of the collision operator suggests that the equation could only be solved approximately, for its application in engineering and science to model complex gas-to-gas interactions, using numerical methods. This equation is one of the most widely studied topics in the field of gas dynamics in the past few decades. The direct computation of the col-

lision operator is an expensive job to perform and several attempts have been made to reduce the cost of its calculation in the past. Even with the most evolved discretization methods, the collision operator remains extortionate computationally. Hence alternative methods in the form of statistical techniques known as the direct simulation Monte Carlo (DSMC) methods [7] were developed for practical engineering applications. A number of difficulties associated with DSMC had cropped up too. Stochastic noise had been an issue in its implementation. In cases of slow-moving flows, where flow speed is lesser than the thermal speed, statistical noise dominates the signals. To prevent that a huge number of statistical data are required which in turn makes the computation expensive. In an attempt to beat these difficulties, various deterministic methods had evolved, *e.g.* Lattice Boltzmann method [32], discrete velocity methods [43], model kinetic equations method [44], the method of moments and extended hydrodynamic methods [42]. The analytical calculation of error is quite complicated for these techniques and hence it was imperative to develop methods which could solve the full Boltzmann directly which could be used both for validation and obtain solutions where approximate methods fail to be accurate.

Several techniques involving the use of Fourier-Galerkin velocity discretization was proposed and was developed by Pareschi and Perthame [36] in 1996 along with a detailed research in accuracy and stability of the method [37, 38] in early 2000. Mouhot and Pareschi in [33, 34, 35] had adapted Carleman representation along with Fourier-Galerkin discretization in order to reduce the computational complexity of the method which was later applied in one and two dimensional flows [17, 18] by Filbet et al. In 2007, Kirsch and Rjasanow [28] proposed a method based on Fourier transform of the collision operator which was later extended by Gamba et al. in [19] and was applied to simulations of spatially inhomogeneous flows in [20, 22].

Despite the fact that the deterministic Fourier-Galerkin discretization method is extremely efficient, they require a large number of discretizations in order to approximate the solutions that are discontinuous or which possesses sharp gradients which are frequent occurrences in gas-to-surface interactions or strong shock waves. In [4] Aristov used locally-supported piecewise constant approximation functions to find the collision operator. Alekseenko and Josyula in [3] applied Discontinuous Galerkin (DG) method to perform higher order approximations which can accommodate for functions with disconti-

nities as well. Their studies show [1, 2] that DG methods are very accurate in maintaining the balance of mass, momentum, and energy even in solutions with discontinuities and sharp gradients, which motivated their study for the full Boltzmann equation for binary collisions. They have constructed the DG bases on a grid of Gauss quadrature nodes using Lagrange basis functions. This method reduces the computational complexity of the collision operator by 3 orders. The original pre-computed collision operator being a $O(n^8)$ computation which was reduced to $O(n^6)$ by the Fourier basis functions and was further reduced to $O(n^5)$ by the DG basis by virtue of uniformity of the mesh and local nature of the basis functions. In addition to the reduction in complexity, the method is well-suited for scalable parallelization.

Dayal and James in [14] discuss objective structures and isometry groups. They have shown in their work that translation groups satisfy the equations of molecular dynamics and the translation groups, $g_j = (\mathbf{Q}_j | \mathbf{c}_j)$, $\mathbf{Q}_j \in O(3)$, $\mathbf{c}_j \in \mathbb{R}^3$, should have an affine dependence with time. To add an interesting perspective to the Boltzmann Equation, which is an approximation to Molecular Dynamics, there should be an exact reduction of the equation for these affine motions. Dayal et al. in their work bring out an ansatz that reduced the dimensionality of the Boltzmann Equation from 7 dimensions to 4 for these particular flows. They argue that if the solution to the equation is known at the origin of physical space, the solution for the entire \mathbb{R}^3 could be obtained with the affine relation. In our work, we have attempted to find solutions to the reduced equation for different flows under *affine* class. It is the reduction in the number of variables by Dayal & James [14] and the efficient calculation of the collision operator by Josyula *et al.*[3], that has motivated us to look for solutions to the Boltzmann equation in non-equilibrium regimes of gas flows. These solutions will allow us to look into real-life situations like flows with high shear rates that are far-from-equilibrium which are difficult to find with experiments.

1.1 Why Boltzmann Equation?

Boltzmann's idea of studying the behavioral patterns of gases with the help of a velocity distribution function instead of tracking each particle with Newton's laws of motion had stemmed from the fact

that even for very dilute gases the number of particles in a space as small as 1 cm^3 has about 3×10^{19} molecules. Hence it is practically a more viable idea to deal with the velocity distribution to understand the behavior of a gas.

The Boltzmann equation today has a lot of applications in the study of non-equilibrium flows of dilute gases. The computation of its collision kernel still remains a difficult task even today, despite the advancement in computational power. The power of the Boltzmann equation to understand complex gas-gas and gas-surface interactions makes it imperative to seek approximate solutions of the Boltzmann equation for its applications in engineering and physics using numerical techniques. Boltzmann in one of his works in 1905[9] had authored the quote:

That is why I do not regard technological achievements as unimportant by-products of natural science but as logical proofs. Had we not attained these practical achievements, we should not know how to infer. Only those inferences are correct that lead to practical success.

One of the many applications of the Boltzmann equation is the study of upper-atmosphere flight where the gas is dilute enough to hold the assumptions of “molecular chaos”. Cercignani *et al.*[11] beautifully describes why the Boltzmann equation becomes indispensable to accurately study the fluid dynamics of the atmosphere. The validity of continuum models, like Euler and Navier-Stokes equations, to present an accurate description of atmospheric gas dynamics might be questioned. They showed that the mean free path of collisions for dilute gases as observed at high altitude is not negligible with respect to some characteristic length as is the assumption in case of continuum theory and in such cases one must resort to kinetic theory for high values of Knudsen number defined as $K_n = \lambda/L$ where λ is the mean free path and L is a characteristic length. In case of a simple Couette Flow (where L is the thickness of the viscous boundary layer) in rarefied gases, the Knudsen number becomes big enough so as to prevent one from neglecting the presence of a thin layer near the wall. This is known as the *slip regime* where the gas slips upon the boundary and has a temperature different from the boundary itself.

In [6], Bellomo *et al.* explores a wide variety of engineering problems that could be solved using

the Boltzmann equation. Generalized kinetic models, defined by one-body distribution functions of a large population of identical interacting entities. For example in traffic flow, the number density of cars at a certain time. Or in, cellular dynamics, the number of cells at an instant with a certain value of activation could be described by the distribution function of the Boltzmann equation. The modeling of traffic flow with the Boltzmann Transport Equation is motivated by the fact that traffic flow in a road is similar to one-dimensional molecular flow of gas particles. The vehicular lengths are negligible as compared to the lengths of roads and the average distance between vehicles are sufficiently large to avoid continuum models.

Another important application of the Boltzmann Equation in modern days is in understanding the behavior of semiconductors materials and metals by solving the equation for electrons and phonons adapted to account for quantum statistics. One of the most powerful tools to investigate the plasma state is the Boltzmann equation for electrons in weakly ionized gas.

Given the varied uses of the Boltzmann Equation and pertaining to the fact of dimensional-reduction in [14], we were motivated to look at its non-equilibrium solutions.

1.2 The Boltzmann Equation

In non-equilibrium statistical mechanics, Maxwell-Boltzmann is a well-known equation [46] describing the evolution of the molecular density function f . The molecular density function $f(t, \mathbf{x}, \mathbf{v})$ is a function of time, velocity vector and the position vector. It describes the velocity distribution of particles per unit phase space volume¹ at a particular instant of time t . Hence the quantity $f(t, \mathbf{x}, \mathbf{v}) d\mathbf{x} d\mathbf{v}$ denotes the number of molecules contained in a differential volume of $d\mathbf{v}$ in velocity space around a point \mathbf{v} and in a differential volume of $d\mathbf{x}$ in physical space around a point \mathbf{x} . The differential volume elements $d\mathbf{x} d\mathbf{v}$ are small enough to consider infinitesimal mathematically yet large enough to hold very large number of molecules in order to consider number density $f(t, \mathbf{x}, \mathbf{v})$ as a continuous

¹Number particles at \mathbf{x} and with \mathbf{v} per unit $d^3\mathbf{x}$ per unit $d^3\mathbf{v}$

function. Thus on integrating over the phase space $dx dv$ we obtain the total number of particles.

$$\int f(t, \mathbf{x}, \mathbf{v}) d\mathbf{x} d\mathbf{v} = N(t) \quad (1.2.0.1)$$

When we integrate the number density only over velocity we obtain the number density:

$$\int f(t, \mathbf{x}, \mathbf{v}) d\mathbf{v} = \rho(\mathbf{x}, t) \quad (1.2.0.2)$$

The idea of the Boltzmann equation is that the constant collision among the particles exchange of energy and momentum takes place and the velocity distribution f changes accordingly through time and space. In order to understand the evolution of the distribution, a molecular density function is considered at point A (\mathbf{x}, \mathbf{v}) in the phase space. In the presence of a velocity independent external force \mathbf{F}_{ext} the molecules located at point A at instant t will have a coordinate $(\mathbf{x} + \mathbf{v}\delta t, \mathbf{v} + [\mathbf{F}_{ext}/m] \delta t)$ (say point B) at the instant $t + \delta t$ with a volume $d\mathbf{x}' d\mathbf{v}'$. Thus the statement of Boltzmann equation becomes:

$$f(\mathbf{x} + \mathbf{v}\delta t, \mathbf{v} + [\mathbf{F}_{ext}/m] \delta t, t + \delta t) - f(\mathbf{x}, \mathbf{v}, t) = \left(\frac{\partial f}{\partial t} \right)_{coll} \delta t \quad (1.2.0.3)$$

The above equation (1.2.0.3) could be written because of the fact that the phase space volume remains conserved under dynamical evolution in time [25]. Now taking a Taylor series expansion up to first order in δt and taking the limit $\delta t \rightarrow 0$ we obtain:

$$\frac{\partial f}{\partial t} + \mathbf{v} \cdot \frac{\partial f}{\partial \mathbf{x}} + \frac{\mathbf{F}_{ext}}{m} \cdot \frac{\partial f}{\partial \mathbf{v}} = \left(\frac{\partial f}{\partial t} \right)_{coll} \quad (1.2.0.4)$$

The right hand side of the equation (1.2.0.4) is known as the collision operator which is because it describes how f evolves due to the collisions among the particles.

1.2.1 Binary Collisions

Now, to understand the right hand side of (1.2.0.4), let us consider the points A and B at instants t and $t + \delta t$ respectively. We assume that the point A is small enough that a collision will result in moving it out of the elemental volume and hence won't be present at B at $t + \delta t$. Similarly, some molecules outside of the point A before collision would end up entering the elemental volume B at $t + \delta t$.

$$\left(\frac{\partial f}{\partial t}\right)_{coll} = \dot{n}_{in} - \dot{n}_{out} \quad (1.2.1.1)$$

where \dot{n}_{in} is the number of particles entering the phase point A due to collisions and \dot{n}_{out} is the number of particles leaving the phase point A after collisions. By considering the gas to be dilute, we could safely consider binary collisions only for evaluation of \dot{n}_{in} and \dot{n}_{out} .

So we could say that the number of molecules at point B, at instant $t + \delta t$, would be the overall gain in the number of molecules added to the number of molecules originally at point A at t . As of now, we assume the interaction potential among the particles to be hard spheres, *i.e.* only elastic collisions take place among particles with the same mass m , with d as the diameter of each particle and ω is the speed of approach (*i.e.* $|\mathbf{v} - \mathbf{v}_*|$)². From the conservation of momentum and energy, the following statements could be written.

$$\mathbf{v} + \mathbf{v}_* = \mathbf{v}' + \mathbf{v}'_* \quad (1.2.1.2a)$$

$$|\mathbf{v}|^2 + |\mathbf{v}_*|^2 = |\mathbf{v}'|^2 + |\mathbf{v}'_*|^2 \quad (1.2.1.2b)$$

Let us consider a beam of particles of velocity \mathbf{v}_* being incident on a particle with velocity \mathbf{v} .

$$I = \rho_{out} |\mathbf{v} - \mathbf{v}_*| \quad (1.2.1.3)$$

I is the incident flux which we define as the number of incident particles crossing a unit area in unit time, from the reference frame of the target and ρ_{out} is the number density of the incident beam.

²All expressions in this section §1.2.1 are in terms of the translated velocity field \mathbf{w} as shown in (2.5.0.3)

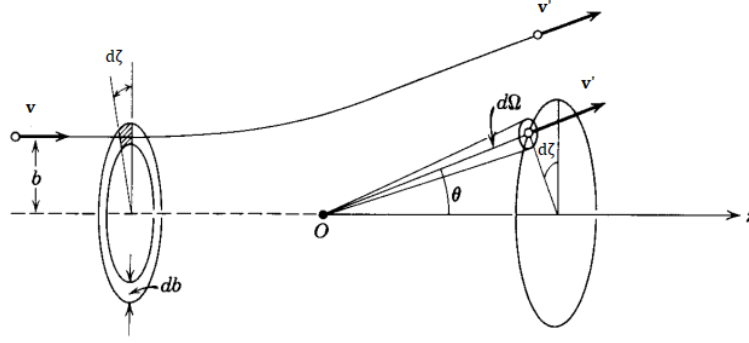


Figure 1.1: Molecule Scattering. (adapted from [25])

Now, the differential cross section could be computed from the intermolecular potential using classical mechanics. We transform the coordinate system to the center-of-mass system in which the total change in momentum is zero. We follow the trajectory of one particle and pretend that it was deflected from fixed point O as shown in Figure 1.1. The relative velocity of approach is \mathbf{v} and the relative velocity of retreat is \mathbf{v}' . Hence from the geometry in Figure 1.1 we could say that if we integrate over all b s and all ζ s we can compute,

$$\dot{n}_{out} = \int_S I b db d\zeta \quad (1.2.1.4)$$

In order to obtain ρ_{out} we say that the collision to occur in the first place because the particles \mathbf{v} and \mathbf{v}_* need to be located in the same physical space and the probability of that occurring is given by the product of the density functions for \mathbf{v} and \mathbf{v}_* ³. Now integrating over all such velocities \mathbf{v}_* other than \mathbf{v} , we can compute the complete expression for \dot{n}_{out} .

$$\dot{n}_{out} = f(\mathbf{x}, \mathbf{v}, t) \int_{\mathbb{R}^3} f(\mathbf{x}, \mathbf{v}_*, t) \int_S b db d\zeta |\mathbf{v} - \mathbf{v}_*| d\mathbf{v}_* \quad (1.2.1.5)$$

The number of particles that would enter the phase point B at instant $t + \delta t$ could be obtained from reversibility of spherically symmetric collisions. It could be written that as

$$\dot{n}_{in} = \int_{\mathbb{R}^3} f(\mathbf{x}, \mathbf{v}', t) f(\mathbf{x}, \mathbf{v}_*, t) \int_S b' db' d\zeta' |\mathbf{v}' - \mathbf{v}_*'| d\mathbf{v}_*' \quad (1.2.1.6)$$

From the conservation statements (1.2.1.2) it could be easily derived that the relative speed of approach

³This is one of the assumptions of “molecular chaos” made for the derivation of the Boltzmann Equation

and the relative speed of retreat are equal. Hence,

$$|\mathbf{v} - \mathbf{v}_*| = |\mathbf{v}' - \mathbf{v}'_*| \Rightarrow \omega = \omega' \quad (1.2.1.7)$$

Because of spherical symmetry of elastic collisions and (1.2.1.7), (1.2.1.6) could be written as:

$$\dot{n}_{in} = \int_{\mathbb{R}^3} f(\mathbf{x}, \mathbf{v}', t) f(\mathbf{x}, \mathbf{v}'_*, t) \int_S b db d\zeta |\mathbf{v} - \mathbf{v}_*| d\mathbf{v}_* \quad (1.2.1.8)$$

and the right hand side of the Boltzmann equation hence becomes,

$$\left(\frac{\partial f}{\partial t} \right)_{coll} = \int_{\mathbb{R}^3} \int_S (f'_* f' - f_* f) |\mathbf{v} - \mathbf{v}_*| dS d\mathbf{v}_* \quad (1.2.1.9)$$

Hence the closed form integro-differential equation, on neglecting any external body force, for a single component gas, turns out to be :-

$$\frac{\partial f}{\partial t} + \mathbf{v} \cdot \frac{\partial f}{\partial \mathbf{x}} = \int_{\mathbb{R}^3} \int_S (f'_* f' - f_* f) |\mathbf{v} - \mathbf{v}_*| dS d\mathbf{v}_* \quad (1.2.1.10)$$

The derivation of the unit vector \mathbf{e} could be sketched by a simple calculation by substituting (1.2.1.12) in (1.2.1.2b). For our model, we have $b_* = d$, which is the maximum distance of approach. The distance of maximum approach could be thought of the cut-off distance of potential to be observed by the molecules. In the case of hard spheres, it simply becomes the diameter of the molecules. The quantity b is the distance of closest approach as shown in Figure 1.1. The geometry of the collision implying, $\theta(b) = \pi - 2 \arcsin \left(\frac{b}{d} \right)$.

$$\begin{aligned} \int_S \dots \omega dS &= \int_0^{2\pi} d\zeta \int_0^d \dots r \omega dr \\ &= \int_0^{2\pi} \int_0^{b_*} \dots |\mathbf{v} - \mathbf{v}_*| b db d\zeta \end{aligned} \quad (1.2.1.11)$$

The post collisional velocities [5] for hard spheres are given by:

$$\begin{aligned} \mathbf{v}' &= \mathbf{v}_a + 0.5\omega\mathbf{e} \\ \mathbf{v}'_* &= \mathbf{v}_a - 0.5\omega\mathbf{e} \end{aligned} \tag{1.2.1.12}$$

where

$$\mathbf{v}_a = 0.5(\mathbf{v} + \mathbf{v}_*) \tag{1.2.1.13}$$

and unit vector \mathbf{e} represents the direction of the relative velocity before the collision of the particles. It is expressed as :

$$\mathbf{e} = (\mathbf{v} - \mathbf{v}_*) / |\mathbf{v} - \mathbf{v}_*| \tag{1.2.1.14}$$

We require to choose a set of coordinate axes in order to perform the computation of the post-collisional velocities. One of the choices for such a set of axes could be the components of vector \mathbf{e} as follows:

$$\begin{aligned} e_1 &= \frac{\omega_1}{\omega} \cos \theta - \frac{\omega_1\omega_3}{\omega\beta} \cos \zeta \sin \theta + \frac{\omega_2}{\beta} \sin \zeta \sin \theta \\ e_2 &= \frac{\omega_2}{\omega} \cos \theta - \frac{\omega_2\omega_3}{\omega\beta} \cos \zeta \sin \theta - \frac{\omega_1}{\beta} \sin \zeta \sin \theta \\ e_3 &= \frac{\omega_3}{\omega} \cos \theta + \frac{\beta}{\omega} \cos \zeta \sin \theta \\ \beta &= \sqrt{\omega_1^2 + \omega_2^2} \end{aligned} \tag{1.2.1.15}$$

It could be observed that while computing the Collision operator with quadrature rules, using these expressions for the post-collision velocities a typical problem could be faced. Since we had the same discretization along all the three axes, the term β vanished at quite a few occasions leading to undefined expressions for post-collisional velocities. To avoid that discrepancy of the coordinate system, we calculated the post-collisional velocities by choosing a different set of coordinate axes, whenever β vanished.

1.3 Why Discontinuous Galerkin Method?

When it comes to solving partial differential equations numerically, we have a large number of methodologies to choose from. Finite difference method, finite element method, and finite volume methods are a few of the widely used computational techniques to discretely represent the spatial gradient term in a partial differential equation *e.g.*

$$\frac{\partial u}{\partial t} + \frac{\partial f(u)}{\partial x} = g \tag{1.3.0.1}$$

These methods are successful and well-tested in a wide variety of problems but have their own strengths and weaknesses. In order to understand the limitation of these classic schemes we need to understand these two points:

- The approximate function $u_h(x, t)$ used to represent the solution $u(x, t)$.
- The sense in which the approximate solution satisfies the partial differential equation.

In the *Finite Difference Method*, a grid is laid down in space and the gradients are approximated using difference methods on a local grid of size $h^k = x^{k+1} - x^k$. Local polynomials are used to approximate the solution and the fluxes in the neighborhood of each grid point. Substituting the local approximation in the (1.3.0.1), the residual is obtained which clearly would not equal zero, in which case $u_h(x, t)$ would be the exact solution of the problem. For a K grid-point stencil, with K unknown coefficients, it makes sense to satisfy the approximate solutions exactly at the grid points. The simplicity and the robustness make it a great choice for a large class of problems[21]. However, relying on 1-D polynomial approximation is the biggest disadvantage for this scheme making it a dimension-by-dimension structure for higher dimension. Additional problems creep up with material discontinuity too. This makes the scheme unattractive for problems with complex geometries.

In order to bring in geometric resilience to the table, it is natural to create an element based discretization. Small simplexes or cubes, used to fill up the physical domain, are organized in an unstructured manner. This method of adding geometric flexibility to the old finite difference method is known as the *Finite Volume Method*. The approximation in this scheme, in its simplest form, is done

with a constant at the center of the element. The cell average of the residual is required to vanish identically in this scheme, for every cell. Because of the local nature of the approximation, there is no imposed condition on the meshing of the problem. Using the Gauss' divergence theorem, the flux term is reduced to a surface terms. In this method, a new challenge is faced in this scheme to compute the fluxes at the element boundaries because the unknowns in this scheme are the cell averages unlike nodal values in the finite difference method. In case of linear problems, the fluxes could be computed with the averages of the fluxes of the adjacent cell averages, which is not a great solution to adopt for non-linear problems. Hence, although the reconstruction of the nodal values at the cell interfaces is a local problem it doesn't restrict the generalization of the scheme to higher dimensional unstructured meshes. Interface fluxes could be computed in various ways as shown in [31] and [45]. However a fundamental problem emerges if one wishes to increase the order of accuracy of their calculation. To reconstruct the solution at the surfaces, in a higher order grid, one would face the requirement of that particular grid structure, which completely defeats the purpose of having geometric flexibility of the scheme. Thus, the general inextensibility to higher order unstructured meshing is the prime limitation of the scheme.

A natural intuition that develops in order to increase the flexibility of the finite volume method is by the introduction of more degrees of freedom on an element and by redefining the elements by the grid points $[x^k, x^{k+1}]$ with a total of K elements and $K + 1$ grid points. The solutions are locally represented by,

$$u_h(x) = \sum_{n=1}^{N_p} a_n \phi_n(x) \quad (1.3.0.2)$$

where $\phi_n(x)$ are local basis functions and the elements share the nodes with their adjacent elements. These local elements are finally assembled into a global representation:

$$u_h(x) = \sum_{k=1}^K u(x^k) N^k(x) \quad (1.3.0.3)$$

Now the residual is required to vanish in such a manner that it is orthogonal to all the test functions

chosen from a space V_h as

$$\int_{\Omega} \left(\frac{\partial u_h}{\partial t} + \frac{\partial f_h}{\partial x} - g_h \right) \psi(x) \, dx = 0; \quad \forall \psi(x) \in V_h \quad (1.3.0.4)$$

Choosing the same space for both the test and basis functions, it becomes the classic case of the *Continuous Galerkin Finite Element Method*[26, 41, 49]. A straightforward substitution of these functions in (1.3.0.1) yields the global mass and stiffness matrices and we have vectors of unknowns, $\mathbf{u}_h = \{u^1, u^2, \dots, u^{K+1}\}^T$, of fluxes, $\mathbf{f}_h = \{f^1, f^2, \dots, f^{K+1}\}^T$, and the forces, $\mathbf{g}_h = \{g^1, g^2, \dots, g^{K+1}\}^T$ at the N_p nodes. This method is quite easily extensible to higher order approximations and allows different element sizes, thereby allowing hp -adaptivity. In particular one could have different orders of approximations in different elements. The limitation of this scheme lies in the problem that the semi-discrete scheme becomes implicit and the mass matrix requires to be inverted. It is a clear disadvantage of the Finite Element method over the Finite Difference and the Finite Volume methods. Another subtle issue with this method is the symmetric nature of the basis functions in space. It becomes a natural choice for many types of problems, *e.g.* the diffusion problem. Nevertheless, in problems like the wave equation or transport equations, where there is a preferred direction of flow, it becomes a less natural choice and causes stability issues if not taken care of properly[26, 49]. In Finite Difference and Finite Volume approaches this issue is overcome by the use of upwinding, through the choice of mesh or through the introduction of fluxes.

A prudent way of combining the Finite Element and the Finite Volume methods harnessing the space of trial and test functions that imitates FEM but satisfying the equation in an FVM sense looks like would have a lot of desired features. This combination is what is known as the *Discontinuous Galerkin Finite Element method* (DG-FEM)[24]. This method would be explained in detail in section §3.1.

Chapter 2

Objective Molecular Dynamics and its Ansatz in Boltzmann Equation

2.1 Objective Structures

An *objective atomic structure* is a structure of a collection of atoms in which each of the atoms observes the same atomic environment up to a translatory and orthogonal rotatory transformations[27]. A simple example would be, if the positions of atoms are represented by $\mathcal{R} = \{\mathbf{r}_1, \mathbf{r}_2, \dots, \mathbf{r}_N\}$, where N could be finite or infinite, the collection of atoms is an objective atomic structure if a corresponding set of orthogonal matrices $\{\mathbf{R}_1, \mathbf{R}_2, \dots, \mathbf{R}_N\}$ exists such that \mathcal{R} is representable in the form:

$$\mathcal{R} = \{\mathbf{r}_i + \mathbf{R}_i (\mathbf{r}_j - \mathbf{r}_1) : j = 1, 2, \dots, N\} \quad (2.1.0.1)$$

for every fixed choice of $i \in \{1, 2, \dots, N\}$. The condition above (2.1.0.1) states that the entire collection of atoms can be recovered by adding to any atom i an admissible orthogonal transformation of the displacements of atoms relative to the position of atom 1 *i.e.* $(\mathbf{r}_j - \mathbf{r}_1)$.

An *objective molecular structures* is defined as a molecular structure comprised of a set of N identical molecules with M atoms each in which the corresponding atoms in each molecule sees the same

environment up to translational and orthogonal transformations. Thus, environments two corresponding atoms could be reconstructed using orthogonal transformations. The structure could be represented by

$$\mathcal{R} = \{\mathbf{r}_{i,j} : i = 1, 2, \dots, N, j = 1, 2, \dots, M\} \quad (2.1.0.2)$$

,where N could be infinite whereas M is finite, such that NM morthogonal matrices exist

$$\mathcal{R} = \{\mathbf{r}_{i,k} + \mathbf{R}_{i,k} (\mathbf{r}_{n,m} - \mathbf{r}_{1,k}) : n = 1, 2, \dots, N, m = 1, 2, \dots, M\} \text{ (no sum over } k) \quad (2.1.0.3)$$

for every choice of $i \in \{1, 2, \dots, N\}, k \in \{1, 2, \dots, M\}$. The Bacteriophage T4, is an ordered struc-

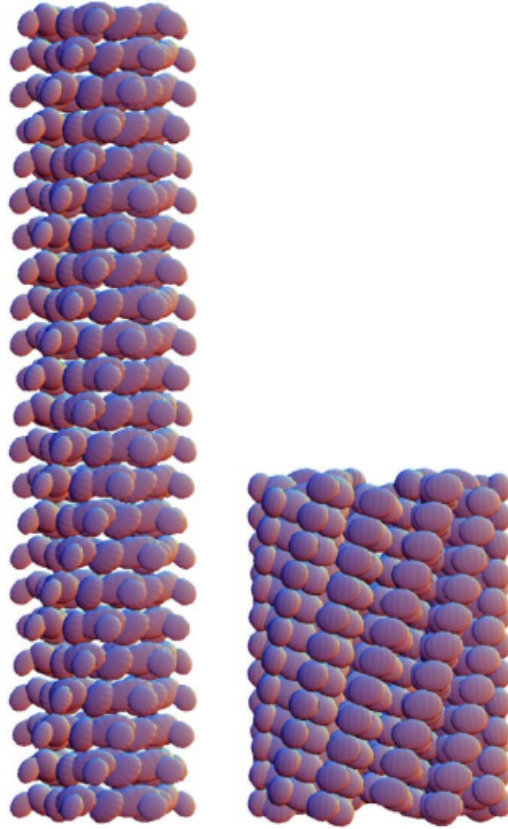


Figure 2.1: Extended (left) and contracted (right) tail sheath of bacteriophage T4. (from [27])

ture of identical protein molecules arranged on a cylindrical shaped lattice is an example of objective structure. The two forms are shown in Figure 2.1- extended and contracted. The tail sheath has 138 molecues in it indexd as $\{(i, j) : i = 0, 1, \dots, 5, j = 0, 1, \dots, 22\}$. Two vectors $\mathbf{t}, \hat{\mathbf{t}}$ and two rotation

matrices \mathbf{Q} , $\hat{\mathbf{Q}}$, are considered, with the form:

$$\hat{\mathbf{t}} = -\rho \mathbf{e}_1, \quad \mathbf{t} = \lambda \mathbf{e}_3 + (\mathbf{Q} - \mathbf{I}) \mathbf{y}_1, \quad \mathbf{Q} = \mathbf{Q}_\gamma, \quad \hat{\mathbf{Q}} = \mathbf{Q}_{\frac{\pi}{3}} \quad (2.1.0.4)$$

where ρ, λ, γ define the geometric parameters of the sheath. The structure in Figure 2.1 is represented by the formula $\{\mathbf{y}_{i,j} + \mathbf{R}_{i,j} \mathbf{p}_k : i \in \{0, 1, \dots, 5\}, j \in \{0, 1, \dots, 22\}, k \in \{0, 1, \dots, M\}\}$ where

$$\mathbf{y}_{i,j} = \mathbf{y}_1 + \sum_{l=0}^{i-1} \hat{\mathbf{Q}}^l \hat{\mathbf{t}} + \hat{\mathbf{Q}}^i \sum_{l=0}^{j-1} \mathbf{Q}^l \mathbf{t} \quad (2.1.0.5a)$$

$$\mathbf{R}_{i,j} = \hat{\mathbf{Q}}^i \mathbf{Q}^j \mathbf{R} \quad (2.1.0.5b)$$

$$\mathbf{y}_1 = \rho \left(\frac{1}{2} \mathbf{e}_1 + \frac{\sqrt{3}}{2} \mathbf{e}_3 \right) \quad (2.1.0.5c)$$

$$\mathbf{Q}_\theta = \begin{pmatrix} \cos \theta & -\sin \theta & 0 \\ \sin \theta & \cos \theta & 0 \\ 0 & 0 & 1 \end{pmatrix} \quad (2.1.0.5d)$$

Now for the structure to qualify for objective structure the sheath should extend to infinity which could be achieved by replacing the set $\{0, 1, \dots, 22\}$ with all integers. The sheath is an objective molecular structure if for every $i, j, k, (i, j) \in \mathbb{Z}^2, k \in \{0, 1, \dots, M\}$ there exists an orthogonal matrix $\mathbf{R}_{(i,j),k}$ such that $\mathbf{r}_{(i,j),k} + \mathbf{R}_{(i,j),k} (\mathbf{r}_{(p,q),m} - \mathbf{r}_{(0,0),k})$ reconstructs the whole structure. That could be shown true with the choice $\mathbf{R}_{(i,j),k} = \hat{\mathbf{Q}}^i \mathbf{Q}^j$.

2.2 Isometry groups

A discrete group G , comprised of elements of the form $g = (\mathbf{Q}|\mathbf{c})$, $\mathbf{Q} \in \mathbf{O}(3)$ and $\mathbf{c} \in \mathbb{R}^3$, is a group of isometries in 3 dimensions. Considering two groups of the form $g_1 = (\mathbf{Q}_1|\mathbf{c}_1)$ and $g_2 = (\mathbf{Q}_2|\mathbf{c}_2)$, group multiplication rule is given by the form $g_1 g_2 = (\mathbf{Q}_1 \mathbf{Q}_2 | \mathbf{Q}_1 \mathbf{c}_2 + \mathbf{c}_1)$ and the inverse rule by $g^{-1} = (\mathbf{Q}^T | -\mathbf{Q}^T \mathbf{c})$. The rules are derived from the isometries acting in the form of $\mathbb{R}^3 : g(\mathbf{x}) =$

$\mathbf{Q}\mathbf{x} + \mathbf{c}$. So $g_1 g_2$ could be obtained by composing the groups, *i.e.* $g_1 \circ g_2$:

$$g_1 \circ g_2 = g_1(g_2(\mathbf{x})) = \mathbf{Q}_1(\mathbf{Q}_2\mathbf{x} + \mathbf{c}_2) + \mathbf{c}_1 = \mathbf{Q}_1\mathbf{Q}_2\mathbf{x} + \mathbf{Q}_1\mathbf{c}_2 + \mathbf{c}_1 = g_1 g_2(\mathbf{x}) \quad (2.2.0.1)$$

Now considering 3 linearly independent vectors $\mathbf{e}_1, \mathbf{e}_2, \mathbf{e}_3$, (not orthogonal in general), the simplest case of 3-dimensional isometry group G_T , could be represented by $t_i = (\mathbf{I}|\mathbf{e}_i)$, $i = 1, 2, 3$. It is given as:

$$G_T = \{t_1^p t_2^q t_3^r : p, q, r \in \mathbb{Z}\} = \{(\mathbf{I}|p\mathbf{e}_1 + q\mathbf{e}_2 + r\mathbf{e}_3) : p, q, r \in \mathbb{Z}\} \quad (2.2.0.2)$$

It could be observed that unless a discrete isometry group contains translations or rotations only, it

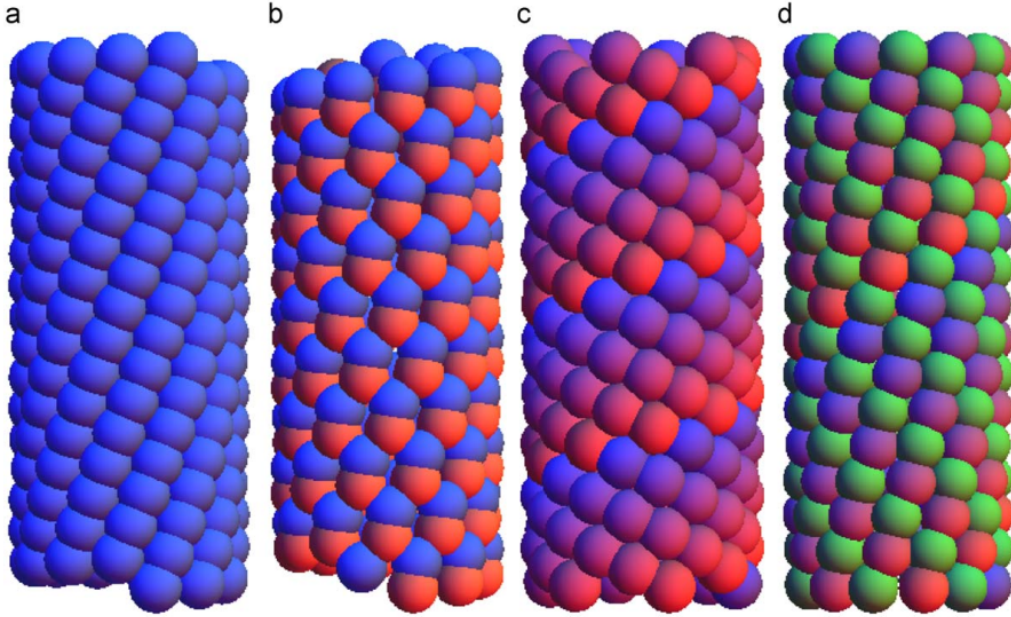


Figure 2.2: Illustration of the four groups in (2.2.0.3). The pictures are obtained by applying each of the groups to a single sphere. Coloring scheme is according to the powers of group elements, as noted. Group parameters conveniently chosen. (a) G_1 : all atoms blue; (b) G_2 : $m = 1$ red; $m = 2$ blue; (c) G_3 : $n = 6$; shading proportional to q ; (d) G_4 : $n = 6$; $m = 1$ green; $m = 2$ red/blue, shading proportional to q . (from [14])

would be expressible in one of the following forms[Dayal et al.]:

$$\begin{aligned}
 G_1 &= \{h^p : p \in \mathbb{Z}\}, \\
 G_2 &= \{h^p f^m : p \in \mathbb{Z}, m = 1, 2\}, \\
 G_3 &= \{h^p g^q : p \in \mathbb{Z}, q = 1, 2, \dots, n\}, \\
 G_4 &= \{h^p g^q f^m : p \in \mathbb{Z}, q = 1, 2, \dots, n, m = 1, 2\},
 \end{aligned}
 \tag{2.2.0.3}$$

where

1. $h = (\mathbf{R}_\theta | \tau \mathbf{e} + (\mathbf{R}_\theta - \mathbf{I}) \mathbf{x}_0)$, $\mathbf{R}_\theta \mathbf{e} = \mathbf{e}$, $|\mathbf{e}| = 1$, $\mathbf{x}_0 \cdot \mathbf{e} = 0$, $\mathbf{e}, \mathbf{x}_0 \in \mathbb{R}^3$, $\tau \neq 0$, and θ is an irrational multiple of 2π .
2. $g = (\mathbf{R}_\psi | (\mathbf{R}_\psi - \mathbf{I}) \mathbf{x}_0)$, $\mathbf{R}_\psi \mathbf{e} = \mathbf{e}$, is a proper rotation with angle $\psi = 2\pi/n$, $n \in \mathbb{Z}$, $n \neq 0$.
3. $f = (\mathbf{R} | (\mathbf{R} - \mathbf{I}) \mathbf{x}_1)$, $\mathbf{R} = -\mathbf{I} + 2\mathbf{e}_1 \otimes \mathbf{e}_1$, $|\mathbf{e}| = 1$, $\mathbf{e} \cdot \mathbf{e}_1 = 0$ and $\mathbf{x}_1 = \mathbf{x}_0 + \xi \mathbf{e}$, for some $\xi \in \mathbb{R}$.

As a converse statement, it could be stated that if f, g, h satisfies 1 – 3 then (2.2.0.3) represents discrete isometry groups with no translation. Static carbon nanotubes are generated with suitable parameters as illustrated schematically in Figure 2.2. Nanotubes of any chirality and any subgroup can be generated using these four groups (2.2.0.3). All one needs to do is change the values of the parameters.

2.3 Objective Molecular Dynamics

Objective molecular dynamics could simply be stated as the simulation of objective structures. In the context of fluid mechanics, OMD is based on *time-dependent translation group*. It is based on frame indifference of the forces acting on an atom due to other atoms. Again considering three linearly independent vectors $\mathbf{e}_1, \mathbf{e}_2, \mathbf{e}_3$ and \mathbf{A} , any transformation, in [15] Dayal *et al.* show that real life structures which could be observed as objective structures (which could as well be represented as isometry

groups),

$$\mathbf{x}_{\nu,k}(t) = g_{\nu}(\mathbf{x}_k(t), t) = \mathbf{x}_k(t) + (\mathbf{I} + t\mathbf{A})(\nu^1\mathbf{e}_1 + \nu^2\mathbf{e}_2 + \nu^3\mathbf{e}_3), k = 1, \dots, M, \forall \nu^i \in \mathbb{Z}^3 \quad (2.3.0.1)$$

satisfy the equation of molecular dynamics,

$$m\ddot{\mathbf{x}}_{\nu,k}(t) = -\frac{\partial\Psi}{\partial\mathbf{x}_{\nu,k}} \quad (2.3.0.2)$$

if a particular set of atoms (*i.e.*the simulated molecule) satisfies the equations of molecular dynamics. In other words, if a structure of N identical molecules with M atoms each, can be observed as an isometry group (or discrete objective structure), with the atoms of the simulated molecule satisfying the equations of molecular dynamics, the atoms in all the N molecules will satisfy the MD equations. An extension of the simulated atoms could be made with instantaneous periodicity with the 3 vectors, $(\mathbf{I} + t\mathbf{A})\mathbf{e}_1, (\mathbf{I} + t\mathbf{A})\mathbf{e}_2, (\mathbf{I} + t\mathbf{A})\mathbf{e}_3$. The simulated atoms diffuse out of the fundamental domain of simulation during a typical simulation. The non-simulated atoms are related to the simulated ones by (2.3.0.1). It could be imagined as a periodic Lagrangian grid-structure $\nu^1\mathbf{e}_1 + \nu^2\mathbf{e}_2 + \nu^3\mathbf{e}_3$, with periods in the order of tens of intermolecular dimensions. Although the molecules diffuse relative to the deformed grid given by the Lagrangian motion, (3.4.0.6), the center of mass of all images of the simulated atoms follow the Lagrangian motion making the macroscopic motion of the flow the same (3.4.0.6). The equation (2.3.0.1) could be well approximated to a continuum equation with a unit cell defined by $\mathcal{U}(t) = \{\Lambda^i(\mathbf{I} + t\mathbf{A})\mathbf{e}_i : 0 \leq \Lambda^i < 1, i = 1, 2, 3\}$ which would be deforming by the action of a Lagrangian description of the motion:

$$\mathbf{x}(\mathbf{y}, t) = (\mathbf{I} + t\mathbf{A})\mathbf{y} \quad (2.3.0.3)$$

And the Eulerian velocity description:

$$\mathbf{v}(\mathbf{z}, t) = \dot{\mathbf{x}}(\mathbf{x}^{-1}(\mathbf{z}, t), t) = \mathbf{A}(\mathbf{I} + t\mathbf{A})^{-1}\mathbf{z} \quad (2.3.0.4)$$

2.4 Viscometric Flows

Viscometric flows have been the most common flow used in the fundamental study of properties of complex fluids. The geometric interpretation of these flows could be seen locally as simple shearing flows with changing the direction of shearing and the normal to the slip surface. In [13], Coleman et al. define Viscometric flows by the following restriction on the relative deformation gradient:

$$\mathbf{F}_t(\mathbf{x}, \tau) = \mathbf{Q}_t(\mathbf{x}, \tau) (\mathbf{I} + (\tau - t) \mathbf{M}_t(\mathbf{x})), \mathbf{M}_t^2 = 0, \mathbf{Q}_t \in O(3), \tau \leq t, t > 0, \mathbf{x} \in \Omega_t \quad (2.4.0.1)$$

where the function $\mathbf{F}_t(\mathbf{x}, \tau), \tau \leq t, \mathbf{x} \in \Omega_t$, the *relative deformation gradient*, is the deformation gradient that maps the domain Ω_t of the body at t to its domain Ω_τ at an earlier time τ . From the condition, $\mathbf{M}_t^2 = 0$ it could be derived that \mathbf{M}_t should have the form $\mathbf{M}_t = \mathbf{a}_t \otimes \mathbf{b}_t$ with $\mathbf{a}_t \cdot \mathbf{b}_t = 0$. The relative deformation gradient, for the affine motion (2.3.0.3) is:

$$\mathbf{F}_t(\mathbf{x}, \tau) = (\mathbf{I} + \tau \mathbf{A})(\mathbf{I} + t \mathbf{A})^{-1} \quad (2.4.0.2)$$

Now comparing $\mathbf{F}_t^T \mathbf{F}_t$ of (2.4.0.1) and (2.4.0.2) and evaluating at $t = 0$, it was observed that an affine motion could describe a viscometric flow if and only if $\mathbf{A} = \mathbf{M}_0 = \mathbf{a} \otimes \mathbf{b}, \mathbf{a} \cdot \mathbf{b} = 0$. Viscometric flows that are universal flows, are only simple shearing flows represented by $\mathbf{A} = \mathbf{a} \otimes \mathbf{b}$ making $(\mathbf{I} + t \mathbf{A})^{-1} = \mathbf{I} - t \mathbf{a} \otimes \mathbf{b}$ and since $\mathbf{a} \cdot \mathbf{b} = 0$, the flow becomes independent of time,

$$\mathbf{v}(\mathbf{x}, t) = \mathbf{A} (\mathbf{I} + t \mathbf{A})^{-1} \mathbf{x} = (\mathbf{b} \cdot \mathbf{x}) \mathbf{a} \quad (2.4.0.3)$$

In an ansatz based on the statistics of objective molecular dynamics, an exact reduction of the Maxwell-Boltzmann equation was made, which have been explained briefly in section §1.2. In this thesis we describe a method to solve the reduced Boltzmann equation for affine and viscometric flows described by the macroscopic Eulerian velocity field:

$$\mathbf{v}(\mathbf{x}, t) = \mathbf{A} (\mathbf{I} + t \mathbf{A})^{-1} \mathbf{x} \quad (2.4.0.4)$$

[15].

Different kinds of fluid flows, even other than Viscometric Flows, could be represented by Universal Flows. These flows have been discussed in Chapter §5 in detail along with their evolution results with the help of the Boltzmann Equation.

2.5 Ansatz in Boltzmann Equation

According to the method of simulation described in §2.3, the trajectories of the atoms in $\mathcal{U} + (\mathbf{I} + t\mathbf{A})\nu^i\mathbf{e}_i$ could be obtained from the ones in the simulated cell \mathcal{U} according to the law: there is an atom in the cell $\mathcal{U} + (\mathbf{I} + t\mathbf{A})\nu^i\mathbf{e}_i$ moving with a velocity of $\mathbf{v} + \mathbf{A}\nu^i\mathbf{e}_i$ if and only if there is one in \mathcal{U} moving with velocity \mathbf{v} . Based on the statistics of OMD and (2.3.0.1) in [14], they have drawn the following inferences:

- The velocities at the origin of physical space are $\dot{\mathbf{x}}_i, i = 1, 2, \dots, M$.
- The velocities at $\mathbf{x} = (\mathbf{I} + t\mathbf{A})\mathbf{y}$ are $\dot{\mathbf{x}}_i + \mathbf{A}\mathbf{y}, i = 1, 2, \dots, M$.
- Alternatively, in Eulerian form, the velocities at \mathbf{x} are $\dot{\mathbf{x}}_i + \mathbf{A}(\mathbf{I} + t\mathbf{A})^{-1}\mathbf{x}, i = 1, 2, \dots, M$.

In terms of molecular density function $f(t, \mathbf{x}, \mathbf{v})$, it could be argued that the probability of finding a velocity $\mathbf{v} + \mathbf{A}(\mathbf{I} + t\mathbf{A})^{-1}\mathbf{x}$ at position \mathbf{x} is the same as the probability of finding a velocity \mathbf{v} at the origin of physical space.

$$f(t, \mathbf{x}, \mathbf{v} + \mathbf{A}(\mathbf{I} + t\mathbf{A})^{-1}\mathbf{x}) = f(t, 0, \mathbf{v}) \quad (2.5.0.1)$$

By rearranging,

$$\begin{aligned} f(t, \mathbf{x}, \mathbf{v}) &= f(t, 0, \mathbf{v} - \mathbf{A}(\mathbf{I} + t\mathbf{A})^{-1}\mathbf{x}) \\ &= g(t, \mathbf{v} - \mathbf{A}(\mathbf{I} + t\mathbf{A})^{-1}\mathbf{x}), \quad \mathbf{v} \in \mathbb{R}^3, \mathbf{x} \in \mathbb{R}^3, t > 0 \end{aligned} \quad (2.5.0.2)$$

This finally led to a deduction of the Boltzmann equation to the form:

$$\frac{\partial g}{\partial t} - \mathbf{A}(\mathbf{I} + t\mathbf{A})^{-1}\mathbf{w} \cdot \frac{\partial g}{\partial \mathbf{w}} = \int_{\mathbb{R}^3} \int_S (g'_*g' - g_*g) |\mathbf{w} - \mathbf{w}_*| dS d\mathbf{w}_* \quad (2.5.0.3)$$

where $\mathbf{w} = \mathbf{v} - \mathbf{A}(\mathbf{I} + t\mathbf{A})^{-1}\mathbf{x}$. Thus reducing the dependence of f to the independent variables t and \mathbf{w} . The macroscopic fields [15] of practical interest that follows from the ansatz (2.5.0.2) as per the definitions of kinetic theory are as follows:

- Density

$$\rho(t, \mathbf{x}) = mn(t, \mathbf{x}) = m \int_{\mathbb{R}^3} f(t, \mathbf{x}, \mathbf{v}) d\mathbf{v} = m \int_{\mathbb{R}^3} g(t, \mathbf{w}) d\mathbf{w} = \rho(t) \quad (2.5.0.4)$$

- Velocity

$$\begin{aligned} \mathbf{u}(t, \mathbf{x}) &= \frac{1}{n} \int_{\mathbb{R}^3} \mathbf{v} f(t, \mathbf{x}, \mathbf{v}) d\mathbf{v} = \frac{1}{n} \int_{\mathbb{R}^3} \mathbf{v} g(t, \mathbf{v} - \mathbf{A}(\mathbf{I} + t\mathbf{A})^{-1}\mathbf{x}) d\mathbf{v} \\ &= \frac{1}{n} \int_{\mathbb{R}^3} (\mathbf{w} + \mathbf{A}(\mathbf{I} + t\mathbf{A})^{-1}\mathbf{x}) g(t, \mathbf{w}) d\mathbf{w} \\ &= \frac{1}{n} \int_{\mathbb{R}^3} \mathbf{w} g(t, \mathbf{w}) d\mathbf{w} + \mathbf{A}(\mathbf{I} + t\mathbf{A})^{-1}\mathbf{x} \\ &= \mathbf{u}_0(t) + \mathbf{A}(\mathbf{I} + t\mathbf{A})^{-1}\mathbf{x} \end{aligned} \quad (2.5.0.5)$$

- Pressure

$$p(t, \mathbf{x}) = -\frac{1}{3} \text{tr} \boldsymbol{\sigma}(t, \mathbf{x}) = \frac{2}{3} \rho e(t) \quad (2.5.0.6)$$

- Internal Energy

$$\begin{aligned} e(t, \mathbf{x}) &= \frac{1}{n} \int_{\mathbb{R}^3} \frac{1}{2} |\mathbf{v} - \mathbf{u}(t, \mathbf{x})|^2 f(t, \mathbf{x}, \mathbf{v}) d\mathbf{v} \\ &= \frac{1}{n} \int_{\mathbb{R}^3} \frac{1}{2} |\mathbf{v} - \mathbf{u}(t, \mathbf{x})|^2 g(t, \mathbf{v} - \mathbf{A}(\mathbf{I} + t\mathbf{A})^{-1}\mathbf{x}) d\mathbf{v} \\ &= \frac{1}{n} \int_{\mathbb{R}^3} \frac{1}{2} |\mathbf{w} - \mathbf{u}_0(t)|^2 g(t, \mathbf{w}) d\mathbf{w} \\ &= \frac{1}{n} \int_{\mathbb{R}^3} \frac{1}{2} |\mathbf{w}|^2 g(t, \mathbf{w}) d\mathbf{w} - \frac{1}{2} |\mathbf{u}_0(t)|^2 = e(t) \end{aligned} \quad (2.5.0.7)$$

- Cauchy Stress

$$\begin{aligned}
 \boldsymbol{\sigma}(t, \mathbf{x}) &= -m \int_{\mathbb{R}^3} (\mathbf{v} - \mathbf{u}(t, \mathbf{x})) \otimes (\mathbf{v} - \mathbf{u}(t, \mathbf{x})) f(t, \mathbf{x}, \mathbf{v}) \, d\mathbf{v} \\
 &= -m \int_{\mathbb{R}^3} (\mathbf{w} - \mathbf{u}_0(t)) \otimes (\mathbf{w} - \mathbf{u}_0(t)) g(t, \mathbf{w}) \, d\mathbf{w} \\
 &= -m \int_{\mathbb{R}^3} (\mathbf{w} \otimes \mathbf{w}) g(t, \mathbf{w}) \, d\mathbf{w} + \rho(t) \mathbf{u}_0(t) \otimes \mathbf{u}_0(t) = \boldsymbol{\sigma}(t)
 \end{aligned} \tag{2.5.0.8}$$

- Heat flux

$$\begin{aligned}
 \mathbf{q}(t, \mathbf{x}) &= m \int_{\mathbb{R}^3} \frac{1}{2} |\mathbf{v} - \mathbf{u}(t, \mathbf{x})|^2 (\mathbf{v} - \mathbf{u}(t, \mathbf{x})) f(t, \mathbf{x}, \mathbf{v}) \, d\mathbf{v} \\
 &= m \int_{\mathbb{R}^3} \frac{1}{2} |\mathbf{w} - \mathbf{u}_0(t)|^2 (\mathbf{w} - \mathbf{u}_0(t)) g(t, \mathbf{w}) \, d\mathbf{w} \\
 &= m \int_{\mathbb{R}^3} \frac{1}{2} |\mathbf{w}|^2 \mathbf{w} g(t, \mathbf{w}) \, d\mathbf{w} + \boldsymbol{\sigma} \mathbf{u}_0 - \rho e \mathbf{u}_0 - \frac{1}{2} \rho |\mathbf{u}_0|^2 \mathbf{u}_0 = \mathbf{q}(t)
 \end{aligned} \tag{2.5.0.9}$$

2.6 Non-dimensionalization of the governing equation

In order to non-dimensionalize the reduced Boltzmann equation, we introduce the reference quantities ρ_0, t_0, v_0, T_0 and d_0 ; where v_0 is the *Most probable speed* or the *Reference speed*. The dimensionless variables are as follows :

$$g = \rho_0 v_0^{-3} \hat{g} = \frac{\rho_0}{\sqrt[3/2]{2RT_0}} \hat{g}, \quad b = d_0 \hat{b}, \quad w_i = v_0 \hat{w}_i, \quad v_0 = \sqrt{2RT_0}, \quad t = t_0 \hat{t}, \quad t_0 = \frac{\lambda}{v_0}, \quad \lambda = \frac{1}{\sqrt{2\pi} \rho_0 d_0^2} \tag{2.6.0.1}$$

Substituting (2.6.0.1) in our reduced Boltzmann equation (2.5.0.3) we get,

$$\begin{aligned}
 \frac{\rho_0}{v_0^3 t_0} \frac{\partial \hat{g}}{\partial \hat{t}} - \mathbf{A}(\mathbf{I} + t_0 \hat{t} \mathbf{A})^{-1} v_0 \hat{\mathbf{w}} \cdot \frac{\partial \hat{g}}{\partial \hat{\mathbf{w}}} \frac{\rho_0}{v_0^3} \frac{1}{v_0} &= \frac{\rho_0^2}{v_0^6} v_0^4 d_0^2 \int_{\mathbb{R}^3} \int_S (\hat{g}'_* \hat{g}' - \hat{g}_* \hat{g}) |\hat{\mathbf{w}} - \hat{\mathbf{w}}_*| \, d\hat{S} \, d\hat{\mathbf{w}}_* \\
 \Rightarrow \frac{\partial \hat{g}}{\partial \hat{t}} - t_0 \mathbf{A}(\mathbf{I} + t_0 \hat{t} \mathbf{A})^{-1} \hat{\mathbf{w}} \cdot \frac{\partial \hat{g}}{\partial \hat{\mathbf{w}}} &= t_0 \rho_0 d_0^2 v_0 \int_{\mathbb{R}^3} \int_S (\hat{g}'_* \hat{g}' - \hat{g}_* \hat{g}) |\hat{\mathbf{w}} - \hat{\mathbf{w}}_*| \, d\hat{S} \, d\hat{\mathbf{w}}_* \\
 \Rightarrow \frac{\partial \hat{g}}{\partial \hat{t}} - t_0 \mathbf{A}(\mathbf{I} + t_0 \hat{t} \mathbf{A})^{-1} \hat{\mathbf{w}} \cdot \frac{\partial \hat{g}}{\partial \hat{\mathbf{w}}} &= \frac{1}{\sqrt{2\pi}} \int_{\mathbb{R}^3} \int_S (\hat{g}'_* \hat{g}' - \hat{g}_* \hat{g}) |\hat{\mathbf{w}} - \hat{\mathbf{w}}_*| \, d\hat{S} \, d\hat{\mathbf{w}}_*
 \end{aligned} \tag{2.6.0.2}$$

We will be using the non-dimensional quantities for the rest of the work but the hat [$\hat{\cdot}$] is omitted

for simplicity. And we define the constant $K = \frac{1}{\sqrt{2\pi}}$. Thus the equation becomes :

$$\begin{aligned} \frac{\partial g}{\partial t} - t_0 \mathbf{A}(\mathbf{I} + t_0 t \mathbf{A})^{-1} \mathbf{w} \cdot \frac{\partial g}{\partial \mathbf{w}} &= K \int_{\mathbb{R}^3} \int_S (g'_* g' - g_* g) |\mathbf{w} - \mathbf{w}_*| dS d\mathbf{w}_* \\ \Rightarrow \frac{\partial g}{\partial t} + \mathbf{p} \cdot \frac{\partial g}{\partial \mathbf{w}} &= K \int_{\mathbb{R}^3} \int_S (g'_* g' - g_* g) |\mathbf{w} - \mathbf{w}_*| dS d\mathbf{w}_* \end{aligned} \quad (2.6.0.3)$$

where $\mathbf{H} = -t_0 \mathbf{A}(\mathbf{I} + t_0 t \mathbf{A})^{-1}$ and $\mathbf{p}(t, \mathbf{w}) = \mathbf{H} \mathbf{w} = -t_0 \mathbf{A}(\mathbf{I} + t_0 t \mathbf{A})^{-1} \mathbf{w}$

Chapter 3

Numerical Solution of The Boltzmann Equation using DG Method

3.1 The Discontinuous Galerkin Method

These are a class of Finite Element methods which uses discontinuous basis functions. This discontinuous nature of its shape functions gives this method an edge over its continuous counterpart, in terms of flexibility of meshing in an unstructured manner for complicated geometrical domains. Arbitrary meshing with hanging nodes. One is free to choose any number of degrees of freedom in an element irrespective of the number in the adjacent ones (p -adaptivity). The methodology is extremely local and only communicates with its neighbors no matter what the order of accuracy of the scheme is. This enables high parallel efficiency[8]. This method was first introduced by Reed and Hill in 1973[39].

The elements in this method is defined in a similar fashion as in finite elements. $\Omega^k = [x^k, x^{k+1}]$. The locality of the scheme is implemented by introducing duplicate nodes at the element interfaces. The unknown vector hence becomes,

$$\mathbf{u}_h = \{u^1, u^2, u^2, u^3, u^3, \dots, u^{K-1}, u^K, u^K, u^{K+1}\} \quad (3.1.0.1)$$

which is $2K$ long instead of $K + 1$ in FEM. The space of the basis functions is a space of piecewise polynomial functions. It could be noted that there is no restriction on the smoothness of shape functions at element edges. A local residual is formed by a local shape function $u_h \in V_h$ for each element,

$$\mathcal{R}_h(x, t) = \frac{\partial u_h}{\partial t} + \frac{\partial f_h}{\partial x} - g(x, t) \quad (3.1.0.2)$$

In CFEM, the residual requires to be orthogonal to all the test functions, making the mass and the stiffness matrices global in nature. In order to maintain the local behavior of the method the residual in DG requires to be orthogonal only to the test functions in the element,

$$\int_{\Omega^k} \mathcal{R}_h(x, t) c(x) dx = 0 \quad (3.1.0.3)$$

The fact that the interface nodes are duplicated and V_h being a broken space, results in the local nature of the scheme. This causes multiple solutions at the nodal interfaces which appears to result in non-unique global solutions at the element edges. Here is where the FVM part comes into the picture to resolve the non-uniqueness of the interface solutions. On applying Gauss' divergence theorem, the local statement is obtained,

$$\int_{\Omega^k} \frac{\partial u_h}{\partial t} l_j^k - f_h^k \frac{dl_j^k}{dx} - gl_j^k dx = - [f_h^k l_j^k]_{x^k}^{x^{k+1}} \quad (3.1.0.4)$$

The boundary term obtained on the right hand side of (3.1.0.4) is the only way to resolve the nonuniqueness of the solutions at the element interfaces and to enforce element connectivity weakly. It could be observed that the flux evaluations at x^{k+1} would be responsible for the computations in the elements Ω^k and Ω^{k+1} , since it is shared by both of them. An introduction of a *Numerical Flux*, f^* is made at this point, containing information from both the elements sharing the interface, as a unique value. The equation is then rewritten as,

$$\int_{\Omega^k} \frac{\partial u_h}{\partial t} l_j^k - f_h^k \frac{dl_j^k}{dx} - gl_j^k dx = - [f^* l_j^k]_{x^k}^{x^{k+1}} \quad (3.1.0.5)$$

Now all we are remaining to completely describe the DG-FE method is choice of the “Numerical Flux”. The dynamics of the problem could be of help in choosing the numerical flux. At this point we require to define a few notations to describe the flux terms. The “-” superscript denotes the interior information of an element and the “+” denotes the exterior. The average is defined as,

$$\{\{u\}\} = \frac{u^- + u^+}{2} \quad (3.1.0.6)$$

The jumps along a normal is defined as,

$$\llbracket u \rrbracket = \hat{\mathbf{n}}^- u^- + \hat{\mathbf{n}}^+ u^+, \quad \llbracket \mathbf{u} \rrbracket = \hat{\mathbf{n}}^- \cdot \mathbf{u}^- + \hat{\mathbf{n}}^+ \cdot \mathbf{u}^+ \quad (3.1.0.7)$$

The specification of the flux, naturally, is related to the dynamics of the equation to be solved. Its role is to ensure the stability of the formulation by imitating the information flow in the governing partial differential equation at hand. In transport equations two dominantly used fluxes are the *upwind flux* ($\alpha = 0$) and the *central flux* ($\alpha = 1$). They are defined as[24],

$$f^* = (au)^* = \{\{au\}\} + |a| \frac{1 - \alpha}{2} \llbracket u \rrbracket \quad (3.1.0.8)$$

for flux functions defined as $f^* = au$. The central flux is simply the average of the two nodal values at the interface whereas in case of upwind flux, the directional information, *i.e.* from where it is coming, is also embedded in it. There is a vast literature on the different choices of fluxes and the penalty to be implemented for depending on the type of the partial differential equation. The choice of flux in transport problems is generally the Lax-Friedrichs’ numerical flux which is simple yet most efficient[24].

3.2 Discontinuous Galerkin velocity discretization

In this method as described by Alekseenko et al. in [3], a cuboid is chosen to discretize in the velocity space, such that the contributions of the molecular velocity distribution function is negligible outside of it. The cuboid is divided into K_j other cuboids uniformly along all the three dimensions. Although in our work only uniform partitions are performed so as to obtain symmetrical advantages while calculating the collision operator. A finite-dimensional basis function $\phi_i(\mathbf{w})$, $i = 1, 2, \dots, s$ is defined on each of the velocity cells. In order to save on computational storage, the same basis functions are chosen for all of the velocity elements.

Let the components of \mathbf{w} to have components $w_i \forall i = 1, 2, 3$ and $s_i \forall i = 1, 2, 3$ being the degrees of polynomial basis functions in the corresponding velocity components. Let $K_j = [\alpha_L^j, \alpha_R^j] \times [\gamma_L^j, \gamma_R^j] \times [\delta_L^j, \delta_R^j]$. The basis functions are constructed in the following way. We locate the nodes at the Gauss quadrature points of order s_1, s_2 and s_3 in the intervals $[\alpha_L^j, \alpha_R^j]$, $[\gamma_L^j, \gamma_R^j]$ and $[\delta_L^j, \delta_R^j]$ respectively. Let the nodes be $\kappa_p^{j;1}, p = 1, 2, \dots, s_1$, $\kappa_q^{j;2}, q = 1, 2, \dots, s_2$ and $\kappa_r^{j;3}, r = 1, 2, \dots, s_3$ in each of the directions of velocity. The basis function in three-dimension is defined as the product of one dimensional Lagrange basis functions which are defined as follows:

$$\varphi_l^{j;1}(w_1) = \prod_{\substack{p=1 \\ p \neq l}}^{s_1} \frac{\kappa_p^{j;1} - w_1}{\kappa_p^{j;1} - \kappa_l^{j;1}}, \quad \varphi_m^{j;2}(w_2) = \prod_{\substack{q=1 \\ q \neq m}}^{s_2} \frac{\kappa_q^{j;2} - w_2}{\kappa_q^{j;2} - \kappa_m^{j;2}}, \quad \varphi_n^{j;3}(w_3) = \prod_{\substack{r=1 \\ r \neq n}}^{s_3} \frac{\kappa_r^{j;3} - w_3}{\kappa_r^{j;3} - \kappa_n^{j;3}} \quad (3.2.0.1)$$

Thus the 3-dimensional shape function would have the form $\phi_i^j(\mathbf{w}) = \varphi_l^{j;1}(w_1)\varphi_m^{j;2}(w_2)\varphi_n^{j;3}(w_3)$, where $i = 1, 2, \dots, s = s_1 s_2 s_3$ is the index running over the combinations of l, m and n for each element j . The computation of i in the algorithm is performed by the formula $i = (l - 1)s_2 s_3 + (m - 1)s_3 + n$.

Lemma 3.1 in [3]

$$\int_{K_j} \phi_p^j(\mathbf{w}) \phi_q^j(\mathbf{w}) d\mathbf{w} = \frac{\Delta \mathbf{w}^j}{8} \xi_p \delta_{pq} \quad (3.2.0.2)$$

, where $\Delta \mathbf{w}^j$ is the volume of the j^{th} element and $\xi_p := \xi_l^{s_1} \xi_m^{s_2} \xi_n^{s_3}$ is the product of the weights of

Gauss quadratures in each of the three dimensions, have simplified many calculations which will be discussed in the following section. All the calculations done in this work are performed with $s_i = 3$.

3.3 Numerical Approximation

3.3.1 Discrete Velocity discretization of the Collision operator

Now we seek solutions of the Boltzmann Equation in the following form of g . The trial & test functions respectively are :

$$g(t, \mathbf{w}) \approx \sum_j g_j(t) \phi_j(\mathbf{w}); \quad h(t, \mathbf{w}) \approx \sum_i h_i(t) \phi_i(\mathbf{w}) \quad (3.3.1.1)$$

On multiplying (2.6.0.3) with the test function $h(t, \mathbf{w})$ and integrating over each element Ω^k and repeating for all elements $k = 1, 2, \dots$, we obtain the weak form of the equation:-

$$\begin{aligned} \int_{\Omega^k} \left(\frac{\partial g}{\partial t} + \mathbf{p} \cdot \frac{\partial g}{\partial \mathbf{w}} \right) h(t, \mathbf{w}) \, d\mathbf{w} \\ = K \int_{\Omega^k} \left(\int_{\Omega^k} \int_S (g'_* g' - g_* g) |\mathbf{w} - \mathbf{w}_*| \, dS \, d\mathbf{w}_* \right) h(t, \mathbf{w}) \, d\mathbf{w} \end{aligned} \quad (3.3.1.2)$$

Now substituting (3.3.1.1) in the left hand side of (3.3.1.2), we get

$$\begin{aligned} \int_{\Omega^k} \dot{g}(t, \mathbf{w}) \left(\sum_i h_i(t) \phi_i(\mathbf{w}) \right) \, d\mathbf{w} + \int_{\Omega^k} \mathbf{p} \cdot \frac{\partial g(t, \mathbf{w})}{\partial \mathbf{w}} \left(\sum_i h_i(t) \phi_i(\mathbf{w}) \right) \, d\mathbf{w} \\ = \sum_i h_i(t) \left[\int_{\Omega^k} \dot{g}(t, \mathbf{w}) \phi_i(\mathbf{w}) \, d\mathbf{w} + \int_{\Omega^k} \phi_i(\mathbf{w}) \frac{\partial g(t, \mathbf{w})}{\partial \mathbf{w}} \cdot \mathbf{p} \, d\mathbf{w} \right] \\ = \sum_i h_i(t) \left[\int_{\Omega^k} \dot{g}(t, \mathbf{w}) \phi_i(\mathbf{w}) \, d\mathbf{w} + \int_{\Omega^k} \phi_i(\mathbf{w}) \frac{\partial g(t, \mathbf{w})}{\partial w_r} p_r \, d\mathbf{w} \right] \\ = \sum_i h_i(t) \left[\int_{\Omega^k} \sum_j \dot{g}_j(t) \phi_j(\mathbf{w}) \phi_i(\mathbf{w}) \, d\mathbf{w} + \int_{\partial \Omega^k} \phi_i(\mathbf{w}) \hat{g}^1(t, \mathbf{w}) p_r n_r - \int_{\Omega^k} g(t, \mathbf{w}) \frac{\partial [\phi_i(\mathbf{w}) p_r]}{\partial w_r} \, d\mathbf{w} \right] \end{aligned} \quad (3.3.1.3)$$

¹ \hat{g} is the Numerical flux explained below

Working with the 3rd integral now,

$$\begin{aligned}
 \int_{\Omega^k} g(t, \mathbf{w}) \frac{\partial [\phi_i(\mathbf{w}) p_r]}{\partial w_r} d\mathbf{w} &= \int_{\Omega^k} \left(\sum_j g_j(t) \phi_j(\mathbf{w}) \right) \frac{\partial [\phi_i(\mathbf{w}) p_r]}{\partial w_r} d\mathbf{w} \\
 &= \int_{\Omega^k} \sum_j g_j(t) \phi_j(\mathbf{w}) \left[\phi_i(\mathbf{w}) \frac{\partial p_r}{\partial w_r} + p_r \frac{\partial \phi_i(\mathbf{w})}{\partial w_r} \right] d\mathbf{w} \\
 &= \int_{\Omega^k} \sum_j g_j(t) \phi_i(\mathbf{w}) \phi_j(\mathbf{w}) \frac{\partial p_r}{\partial w_r} d\mathbf{w} + \int_{\Omega^k} \sum_j g_j(t) \phi_j(\mathbf{w}) \frac{\partial \phi_i(\mathbf{w})}{\partial w_r} p_r d\mathbf{w} \\
 &= \int_{\Omega^k} \sum_j g_j(t) \phi_i(\mathbf{w}) \phi_j(\mathbf{w}) (\text{tr } \mathbf{H}) d\mathbf{w} + \int_{\Omega^k} \sum_j g_j(t) \phi_j(\mathbf{w}) \frac{\partial \phi_i(\mathbf{w})}{\partial w_r} p_r d\mathbf{w}
 \end{aligned} \tag{3.3.1.4}$$

where

$$\begin{aligned}
 B_{ij} &= \int_{\Omega^k} \phi_i(\mathbf{w}) \phi_j(\mathbf{w}) d\mathbf{w} \\
 C_{ij} &= \int_{\Omega^k} \phi_j(\mathbf{w}) \left(\frac{\partial \phi_i(\mathbf{w})}{\partial \mathbf{w}} \cdot \mathbf{p} \right) d\mathbf{w} \\
 \Psi_i &= \int_{\partial \Omega^k} \phi_i(\mathbf{w}) \hat{g}(t, \mathbf{w}) p_r n_r
 \end{aligned} \tag{3.3.1.5}$$

On applying the Gauss divergence theorem in the derivation of equation (3.3.1.3), we obtain a boundary term where we introduce something known as the ‘‘Numerical Flux’’. Unlike continuous galerkin method (where we have a single node at the element boundary) in DG methods we might not have nodes at the element boundaries at all and the interface conditions are enforced weakly using numerical fluxes. The numerical flux \hat{g} is a single-valued function of the numerical solutions on both sides of the interface, *i.e.* g^- and g^+ because of the discontinuity in the solution g there. For hyperbolic transport equations upwind flux gives good results [47]. Implementation of upwind flux is basically choosing T In this work we have considered the general classical Lax-Friedrichs flux (3.3.1.6) and by setting α equal to zero we get back upwind flux.

$$\hat{g} = \{ \{ (\mathbf{p} \cdot \mathbf{n}) g \} \} + |\mathbf{p} \cdot \mathbf{n}| \frac{1 - \alpha}{2} \llbracket g \rrbracket \tag{3.3.1.6}$$

where $\{ \{ g \} \} = \frac{g^- + g^+}{2}$ and $\llbracket g \rrbracket = \hat{n}^- g^- + \hat{n}^+ g^+$. Unlike regular Finite Element Methods where element connectivity is ensured by the continuous nature of the shape functions even across element edges, in DG methods numerical flux is the only way element connectivity is enforced weakly.

Because of the Lemma 3.1 in [3], (3.2.0.2), which is a consequence of the orthogonality of the Lagrange polynomials chosen for the discretization, the matrix B turns out to be a diagonal matrix consisting of the s different weights in each of the element repeated j times. Also to be noted that despite choosing a finite domain for our calculation, all the integrations performed are over \mathbb{R}^3 space. It is done by extending the shape functions with zero beyond the chosen domain over the entire \mathbb{R}^3 space.

$$\begin{aligned}
 & K \int_{\Omega^k} \int_{\Omega^k} \int_S (g'_* g' - g_* g) |\mathbf{w} - \mathbf{w}_*| \left(\sum_i h_i(t) \phi_i(\mathbf{w}) \right) dS d\mathbf{w}_* d\mathbf{w} \\
 &= K \sum_i h_i(t) \int_{\Omega^k} \int_{\Omega^k} \int_S \phi_i(\mathbf{w}) (g'_* g' - g_* g) |\mathbf{w} - \mathbf{w}_*| dS d\mathbf{w}_* d\mathbf{w} \\
 &= K \sum_i h_i(t) \int_{\Omega^k} \int_{\Omega^k} \frac{|\mathbf{w} - \mathbf{w}_*|}{2} g_* g \int_S (\phi'_{*i} + \phi'_i - \phi_{*i} - \phi_i) dS d\mathbf{w}_* d\mathbf{w}
 \end{aligned} \tag{3.3.1.7}$$

Thus, the RHS of i^{th} equation becomes,

$$K \int_{\Omega^k} \int_{\Omega^k} \frac{|\mathbf{w} - \mathbf{w}_*|}{2} g(t, \mathbf{w}_*) g(t, \mathbf{w}) M_i d\mathbf{w}_* d\mathbf{w} \tag{3.3.1.8}$$

where M_i is :

$$M_i = M(\mathbf{w}, \mathbf{w}_*, \phi_i) = \frac{|\mathbf{w} - \mathbf{w}_*|}{2} \int_S (\phi'_{*i} + \phi'_i - \phi_{*i} - \phi_i) dS \tag{3.3.1.9}$$

The final i^{th} equations becomes :-

$$\begin{aligned}
 B_{ij} \dot{g}_j(t) + \Psi_i - (\text{tr } \mathbf{H}(t)) B_{ij} g_j(t) - C_{ij} g_j(t) &= K \int_{\Omega^k} \int_{\Omega^k} g(t, \mathbf{w}_*) g(t, \mathbf{w}) M_i d\mathbf{w}_* d\mathbf{w} \\
 &= F_i [g]
 \end{aligned} \tag{3.3.1.10}$$

where $F_i [g]$ is a non-linear function in g and is given by :

$$\begin{aligned}
 F_i [g] &= \int_{\Omega^k} \int_{\Omega^k} \left(\sum_j g_j(t) \phi_j(\mathbf{w}_*) \right) \left(\sum_k g_k(t) \phi_k(\mathbf{w}) \right) M_i d\mathbf{w}_* d\mathbf{w} \\
 &= F_{ijk} g_j(t) g_k(t)
 \end{aligned} \tag{3.3.1.11}$$

Thus F_{ijk} is expressed as :

$$F_{ijk} = \int_{\Omega^k} \int_{\Omega^k} M_i \phi_j(\mathbf{w}_*) \phi_k(\mathbf{w}) d\mathbf{w}_* d\mathbf{w} \quad (3.3.1.12)$$

To be noted here that both B_{ij} and F_{ijk} are independent of t and thus they need to be calculated only once before we start the forward march in time but on the other hand C_{ij} is time dependent and needs to be calculated at every time step.

The Lemmas 4.1 and 4.2 in [3] gave us a big advantage in calculation of the Collision operator. By using the symmetry property of the collision operator (section 2.4 in [29]) (explained in Appendix §6.1) the RHS of the equation could be simplified in the following way:

Lemma 4.1:

$$M(\mathbf{w}, \mathbf{w}_*, \phi_i) = M(\mathbf{w}_*, \mathbf{w}, \phi_i), \quad \forall \mathbf{w}, \mathbf{w}_* \in \mathbb{R}^3 \quad (3.3.1.13)$$

Also,

$$M(\mathbf{w}, \mathbf{w}, \phi_i) = 0, \quad \forall \mathbf{w} \in \mathbb{R}^3 \quad (3.3.1.14)$$

The above Lemma 4.1, holds good only for a system of gas with all the particles having the same mass and the potential of interaction of the particles is spherically symmetric.

Lemma 4.2:

$$M(\mathbf{w} + \boldsymbol{\eta}, \mathbf{w}_* + \boldsymbol{\eta}, \phi_i(\mathbf{w} - \boldsymbol{\eta})) = M(\mathbf{w}, \mathbf{w}_*, \phi_i), \quad \forall \boldsymbol{\eta} \in \mathbb{R}^3 \quad (3.3.1.15)$$

This Lemma 4.2, holds good only when the potential of the molecular interaction is dependent only on the molecular distance. It could be noticed that Lemma 4.2 lets us reduce the memory storage for the collision operator dramatically in case of a uniform mesh and the same shape functions in every element. In case of a uniform cubical mesh, all we need to do is to compute the collision operator for a single element (in our case, we compute for the central element of the domain) and the values for the

rest of the elements could be restored using the invariance property mentioned above. The sketches of the proofs of the Lemmas could be found in the Appendix of [3].

Now because of the orthogonal property of the Lagrange polynomials, (3.3.1.12) could be further reduced to the form,

$$F_{ijk} = \frac{\Delta \mathbf{w}^j \xi_j}{8} \frac{\Delta \mathbf{w}_*^k \xi_k}{8} M(\mathbf{w}^j, \mathbf{w}_*^k, \phi_i) \quad (3.3.1.16)$$

where $\Delta \mathbf{w}^i$ is the volume of the element to which the i^{th} node belongs. It could be observed that because of the orthogonal nature of the shape functions, the integrals which when performed by summing over the quadrature points, where the nodes were introduced, over \mathbf{w} and \mathbf{w}_* , we end up with just the combinations of weights of the Gauss quadrature rule. Hence the only integrations we needed to perform to compute the Collision operator (which was initially an eight dimensional integration) were over the spherical surface S (b and ζ). In order to achieve an accuracy of 10^{-8} in a velocity domain of $[-3, 3]^3$ as suggested by Josyula *et al.* in [3] in order to preserve moments and obtain correct relaxation times it is indispensable to use adaptive quadrature for the computation of $M(\mathbf{w}^j, \mathbf{w}_*^k, \phi_i)$.

In this work, we have used a cube with sides $[3, 3]$ for the dimensionless velocity domain. For all the problems we have used the discrete Galerkin basis with $s_1 = s_2 = s_3 = 3$ (piecewise quadratic). All the problems were run for a 27 element mesh and a 125 element mesh *i.e.*, with 9 and 15 nodes or degrees of freedom in each dimension over the entire domain of calculation. The reduced size of the Collision operator could be attributed to the local nature of the basis functions which results in making F_{ijk} a sparse matrix. The locally supported basis functions result in non-overlapping collision spheres for most pairs of \mathbf{w} and \mathbf{w}_* with most shape functions ϕ_i . Hence, most entries of the Collision operator F_{ijk} are zeros.

The simulations in this work were run with uniform cubical meshes for the velocity discretization and the same Lagrange basis functions for each dimension were used on each element. The collision operator was calculated only for the central element of the mesh and the values for the rest of the elements were restored using (3.3.1.15). Since the entries of the Collision operator are independent

of each other, their computation was possible to parallelize. The simulations run in this work were parallelized using OpenMP in 28 cores.

3.3.2 Time Discretization

The forward marching in time was performed by an explicit fifth order Adams-Bashforth method and the initial data was obtained by using fifth order Runge-Kutta method for the first four iterations [10].

Equating the LHS (3.3.1.3) and the RHS (3.3.1.7) of the discretized i^{th} equation, we get:

$$\begin{aligned}
 B_{ij}\dot{g}_j(t) + \Psi_i - (\text{tr } \mathbf{H}(t)) B_{ij}g_j(t) - C_{ij}g_j(t) &= F_{ijk}g_j(t)g_k(t) \\
 \Rightarrow \dot{g}_j(t) &= B_{ij}^{-1} [C_{ik}(t)g_k(t) + (\text{tr } \mathbf{H}(t)) B_{ij}g_j(t) + F_{ilk}g_l(t)g_k(t) - \Psi_i] \\
 \Rightarrow \dot{g}_j(t) &= \psi_j(t, \mathbf{g}(t))
 \end{aligned} \tag{3.3.2.1}$$

We apply fifth order RK method to obtain the first five initial data to start our multi-step method. Fifth order RK method:

$$\begin{aligned}
 k_j^1 &= \psi_j(t^s, \mathbf{g}^s), \\
 k_j^2 &= \psi_j\left(t^s + \frac{1}{4}\Delta t, \mathbf{g}^s + \frac{1}{4}\mathbf{k}^1\Delta t\right), \\
 k_j^3 &= \psi_j\left(t^s + \frac{1}{4}\Delta t, \mathbf{g}^s + \frac{1}{8}\mathbf{k}^1\Delta t + \frac{1}{8}\mathbf{k}^2\Delta t\right), \\
 k_j^4 &= \psi_j\left(t^s + \frac{1}{2}\Delta t, \mathbf{g}^s - \frac{1}{2}\mathbf{k}^2\Delta t + \mathbf{k}^3\Delta t\right), \\
 k_j^5 &= \psi_j\left(t^s + \frac{3}{4}\Delta t, \mathbf{g}^s + \frac{3}{16}\mathbf{k}^1\Delta t + \frac{9}{16}\mathbf{k}^4\Delta t\right), \\
 k_j^6 &= \psi_j\left(t^s + \Delta t, \mathbf{g}^s - \frac{3}{7}\mathbf{k}^1\Delta t + \frac{2}{7}\mathbf{k}^2\Delta t + \frac{12}{7}\mathbf{k}^3\Delta t - \frac{12}{7}\mathbf{k}^4\Delta t + \frac{8}{7}\mathbf{k}^5\Delta t\right), \\
 g_j^{s+1} &= g_j^s + \frac{\Delta t}{90} (7k_j^1 + 32k_j^3 + 12k_j^4 + 32k_j^5 + 7k_j^6)
 \end{aligned} \tag{3.3.2.2}$$

We use the above equations for $s = 0, 1, 2$ and 3 . After obtaining the first five initial data with the fifth order RK method, the following fifth order Adams-Bashforth formula was applied to perform time

integration and observe the evolution of the molecular velocity distribution function over time:

$$g_j^{s+1} = g_j^s + \frac{\Delta t}{720} [1901\psi_j(t^s, \mathbf{g}^s) - 2774\psi_j(t^{s-1}, \mathbf{g}^{s-1}) + 2616\psi_j(t^{s-2}, \mathbf{g}^{s-2}) - 1274\psi_j(t^{s-3}, \mathbf{g}^{s-3}) + 251\psi_j(t^{s-4}, \mathbf{g}^{s-4})] \quad (3.3.2.3)$$

where $s = 4, 5, \dots, N - 1$. The bottleneck for the time-stepping code was the computation of $\psi(t, \mathbf{g})$ in every step. It was possible to parallelize the calculation of $\psi(t, \mathbf{g})$ using 28 cores in OpenMP for every step which added to the performance of the time-stepping algorithm.

3.4 Conservation Routines

The Collision operator $F_i[\mathbf{g}]$ that we compute in (3.3.1.11) does not preserve moments as desired possibly due to domain truncation. As suggested by Gamba *et al.* [ZHANG and GAMBA] we force an intermediate conservation routine. The problem could be posed as a L^2 -distance minimization problem with the constraint of preserving the necessary moments. The problem is solved using *Lagrange Multiplier method*.

The conservation routine should hold for any time for the approximate solution function $\mathcal{F}(t, \mathbf{w})$,

$$\int_{\Omega_k} \mathcal{F}(t, \mathbf{w}) \Phi(\mathbf{w}) d\mathbf{w} = \int_{\Omega_k} \mathcal{F}(t=0, \mathbf{w}) \Phi(\mathbf{w}) d\mathbf{w} \quad (3.4.0.1)$$

where $\Phi(\mathbf{w})$ is one of the collision invariants. The desired conservation of the moments could be obtained by,

$$\mathbf{Q}\mathbf{F} = 0 \quad (3.4.0.2)$$

on the approximate collision vector \mathbf{F} where,

$$\mathbf{Q} = \begin{pmatrix} \int_{\Omega_k} \phi_i(\mathbf{w}) d\mathbf{w} \\ \int_{\Omega_k} \phi_i(\mathbf{w}) w d\mathbf{w} \\ \int_{\Omega_k} \phi_i(\mathbf{w}) |\mathbf{w}|^2 d\mathbf{w} \end{pmatrix} \quad (3.4.0.3)$$

where ϕ_i is the i^{th} basis function in the Ω_k element. Now the minimization problem becomes to find \mathbf{F}_c ,

$$\begin{aligned} \min \frac{1}{2} (\mathbf{F}_c - \mathbf{F})^T \mathbf{B} (\mathbf{F}_c - \mathbf{F}) \\ \text{s.t. } \mathbf{Q}\mathbf{F}_c = 0 \end{aligned} \quad (3.4.0.4)$$

By implementing Lagrange multiplier method, where Λ is the multiplier vector and \mathbf{B} is a positive definite diagonal matrix as earlier defined in (3.3.1.5). We have the objective function for our problem to be:

$$\mathcal{L}(\mathbf{F}_c, \Lambda) = \frac{1}{2} (\mathbf{F}_c - \mathbf{F})^T \mathbf{B} (\mathbf{F}_c - \mathbf{F}) - \Lambda^T \mathbf{Q}\mathbf{F}_c \quad (3.4.0.5)$$

Now the critical values of \mathcal{L} are obtained by,

$$\begin{cases} \frac{\partial \mathcal{L}}{\partial \mathbf{F}_c} = 0 \\ \frac{\partial \mathcal{L}}{\partial \Lambda} = 0 \end{cases} \quad (3.4.0.6)$$

Solving for the equations above, we obtain the minimizer \mathbf{F}_c ,

$$\mathbf{F}_c = \left[\mathbb{I} - \mathbf{B}^{-1} \mathbf{Q}^T (\mathbf{Q} \mathbf{B}^{-1} \mathbf{Q}^T)^{-1} \mathbf{Q} \right] \mathbf{F} \quad (3.4.0.7)$$

In our time discretization routines, for the homogeneous Boltzmann equation, where we substitute $\mathbf{A} = 0$, we implement the complete conservation routine with constraints for all the moments for mass, momentum and energy and implement the following scheme,

$$\frac{dg_i}{dt} = \mathbf{F}_c \quad (3.4.0.8)$$

For the case of the complete transport equation, the conservation routine is implemented on $\psi_j(t, \mathbf{g}(t))$ (3.3.2.1) instead of \mathbf{F} making it,

$$\frac{\partial g_i}{\partial t} = \left[\mathbb{I} - \mathbf{B}^{-1} \mathbf{Q}^T (\mathbf{Q} \mathbf{B}^{-1} \mathbf{Q}^T)^{-1} \mathbf{Q} \right] \psi_j(t, \mathbf{g}(t)) \quad (3.4.0.9)$$

Another important factor about the “Constraint matrix” \mathbf{Q} , in the case of non-zero \mathbf{A} , is that it contains only the mass preserving constraint only. It is because in the complete transport equation we apply shear force and thus imparting momentum and energy to the system. In this case, we expect the momentum and the energy of the system to rise and hence do not want to constrain them.

Chapter 4

Verification Results

4.1 Spatially homogeneous relaxation

Over the few decades, with the flourishing of efficient and swift computers, predictive modeling has become popular to cut down the search space for experiments. As simulation codes become more sophisticated, intensive check turns out to be progressively challenging and tedious, however more essential. Because of the complexity of the Collision operator of the Boltzmann transport equation, it becomes indispensable that we test our code in parts. The LHS of (2.6.0.3) is tested using the Method of Manufactured Solutions and the RHS is validated with the convergence of gas in perturbed states.

We run simulations for the relaxation of a monoatomic gas from perturbed states with the Boltzmann equation (2.6.0.3) for $\mathbf{A} = 0$ with hard sphere potential for molecular collisions using quadratic Lagrange shape functions and three and five elements in each velocity dimension. We have conducted two simulation experiments with $\mathbf{A} = 0$, leaving only the time derivative part in the reduced Boltzmann equation (2.6.0.3) from the total derivative on the left hand side (4.1.0.1).

$$B_{ij}\dot{g}_j(t) = F_{ijk}g_j(t)g_k(t) \tag{4.1.0.1}$$

This would allow us to observe the solution to the Boltzmann Equation at equilibrium. According

to Maxwell the solution to the equilibrium Boltzmann Equation in the absence of any gradient will always lead to a Gaussian distribution [12].

4.1.1 Experiment 1

In this experiment we take two equilibrium streams as a sum of two Gaussian distributions and the results are as follows. Figure 4.1, Figure 4.2, and Figure 4.3 are the sections of the molecular density function along the w_1, w_2 and w_3 axes with 27 elements in the entire domain. Figure 4.6a, Figure 4.6c, and Figure 4.6e are its sections on the planes $w_1 = 0, w_3 = 0,$ and $w_2 = 0$ respectively at time $t = 0$ and Figure 4.6b, Figure 4.6d, and Figure 4.6f are its sections on the planes $w_1 = 0, w_3 = 0,$ and $w_2 = 0$ respectively at the equilibrium state. The initial condition used to simulate this experiment was:

$$g(t = 0, \mathbf{w}) = \frac{\rho_1}{2\pi T_1^{\frac{3}{2}}} \exp\left(-\frac{1}{2T_1} |\mathbf{w} - \mathbf{v}_{avg1}|^2\right) + \frac{\rho_2}{2\pi T_2^{\frac{3}{2}}} \exp\left(-\frac{1}{2T_2} |\mathbf{w} - \mathbf{v}_{avg2}|^2\right) \quad (4.1.1.1)$$

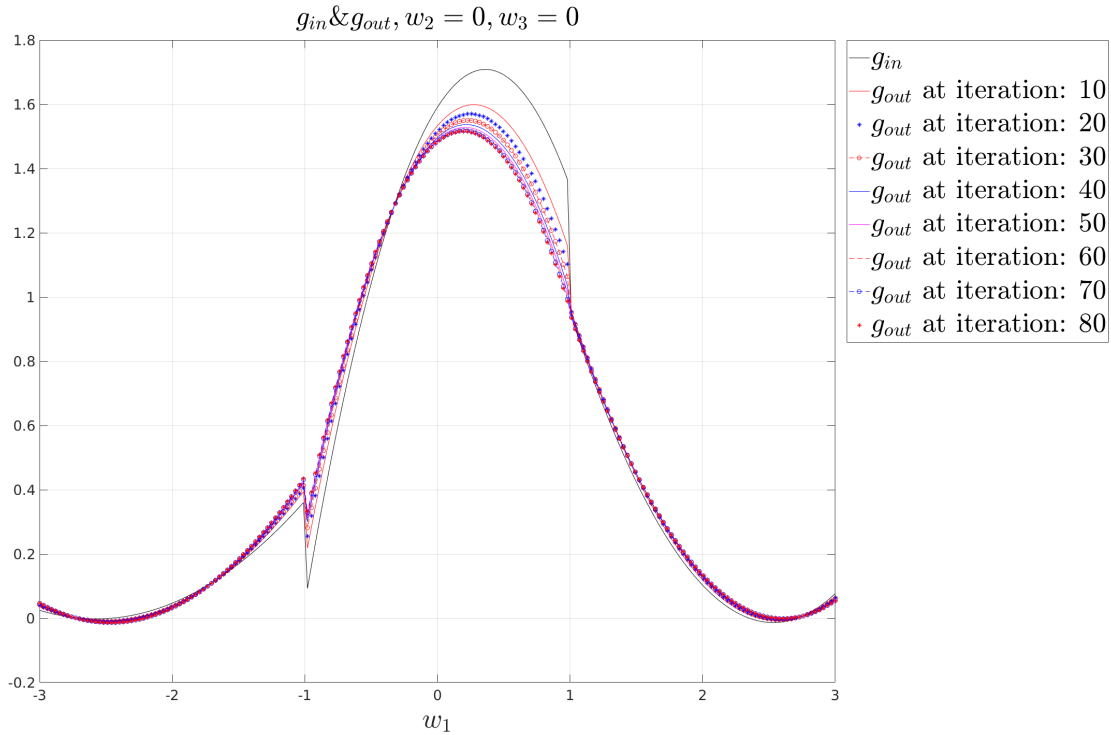


Figure 4.1: Validation Experiment 1 with 27 elements: Evolution of g with $w_2 = w_3 = 0$

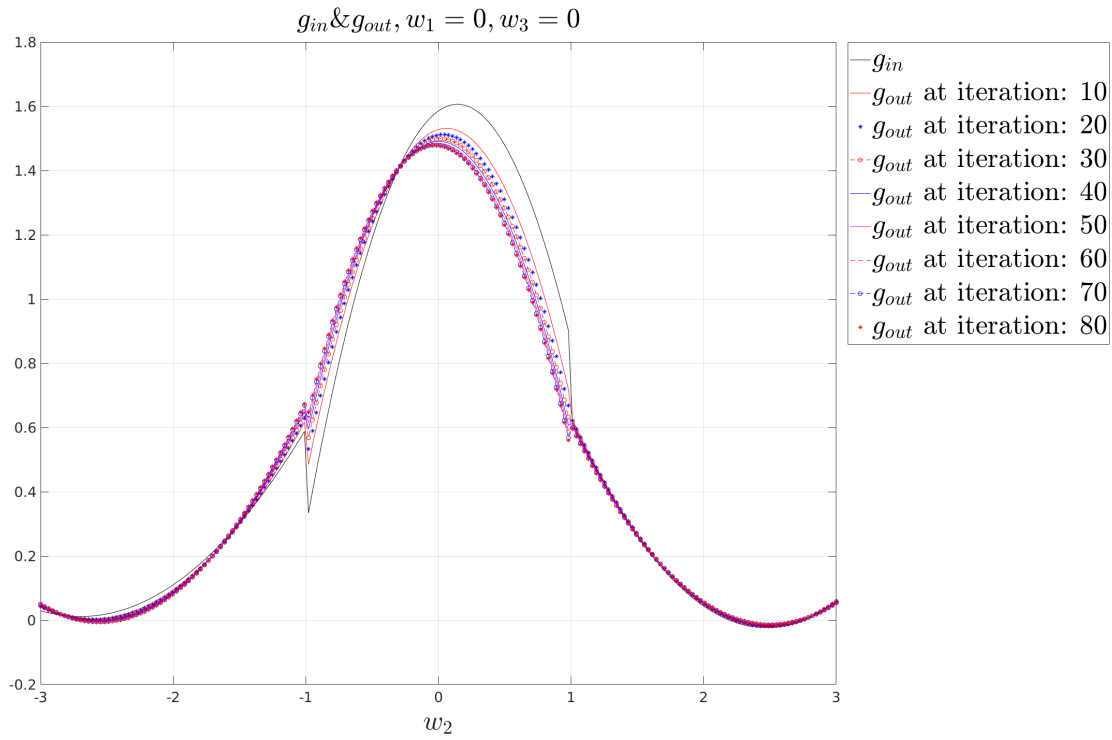


Figure 4.2: Validation Experiment 1 with 27 elements: Evolution of g with $w_1 = w_3 = 0$

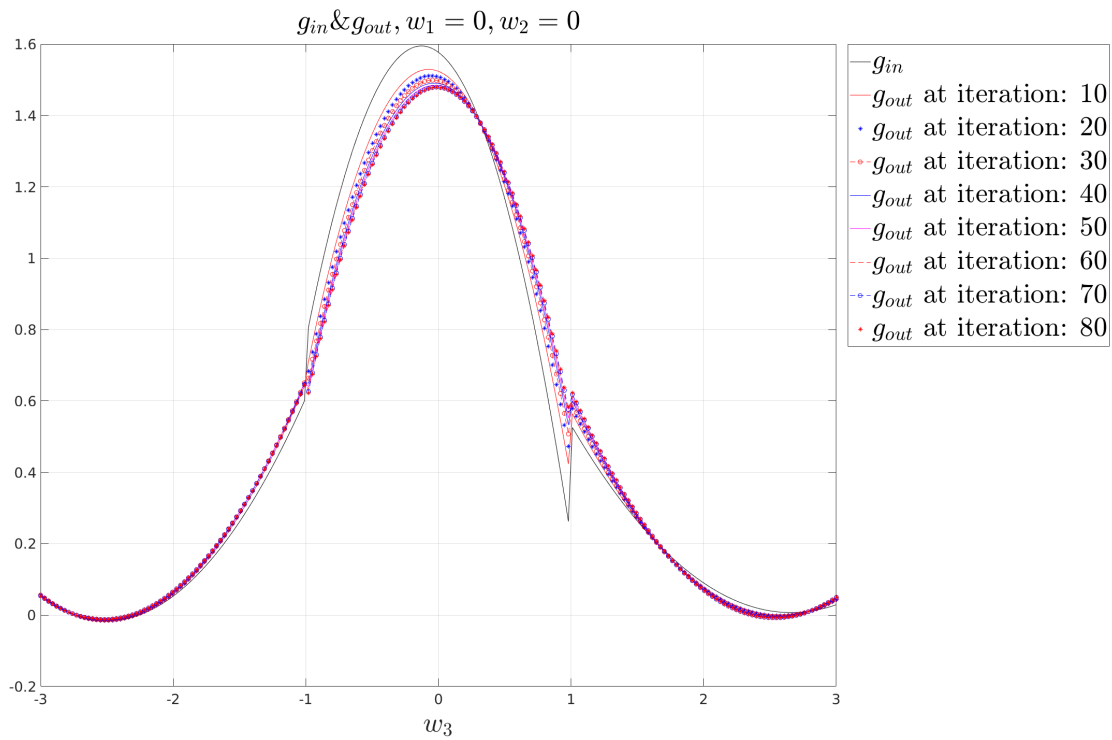


Figure 4.3: Validation Experiment 1 with 27 elements: Evolution of g with $w_1 = w_2 = 0$

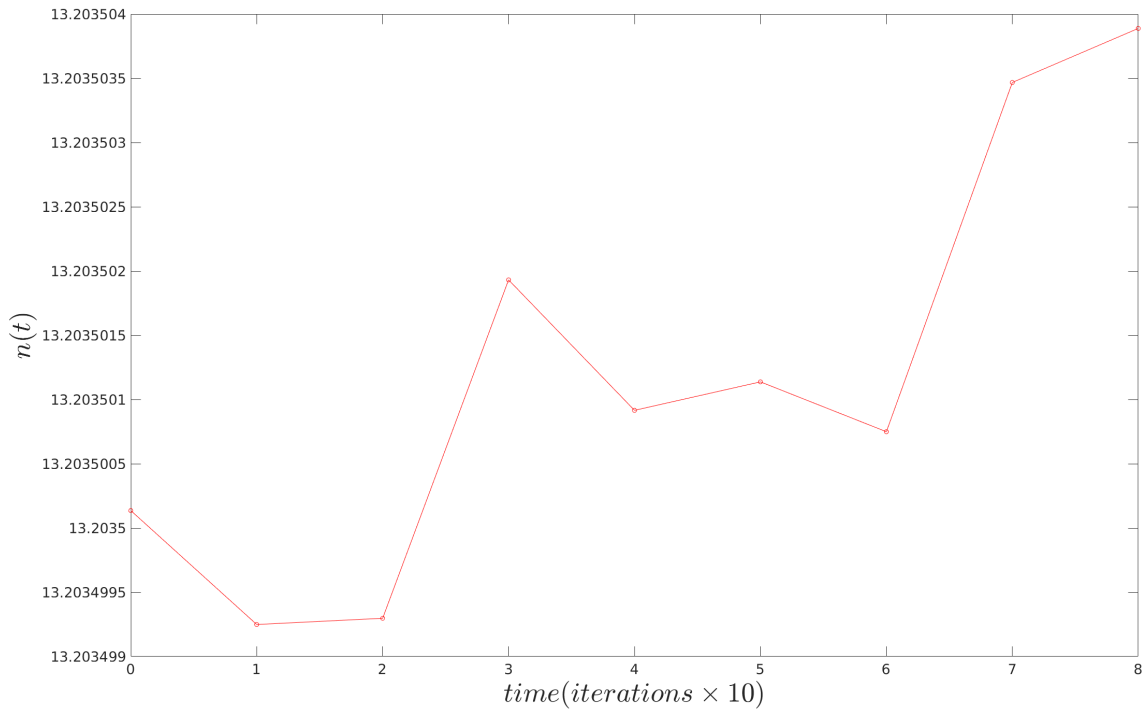


Figure 4.4: Validation Experiment 1 with 27 elements: Number Density

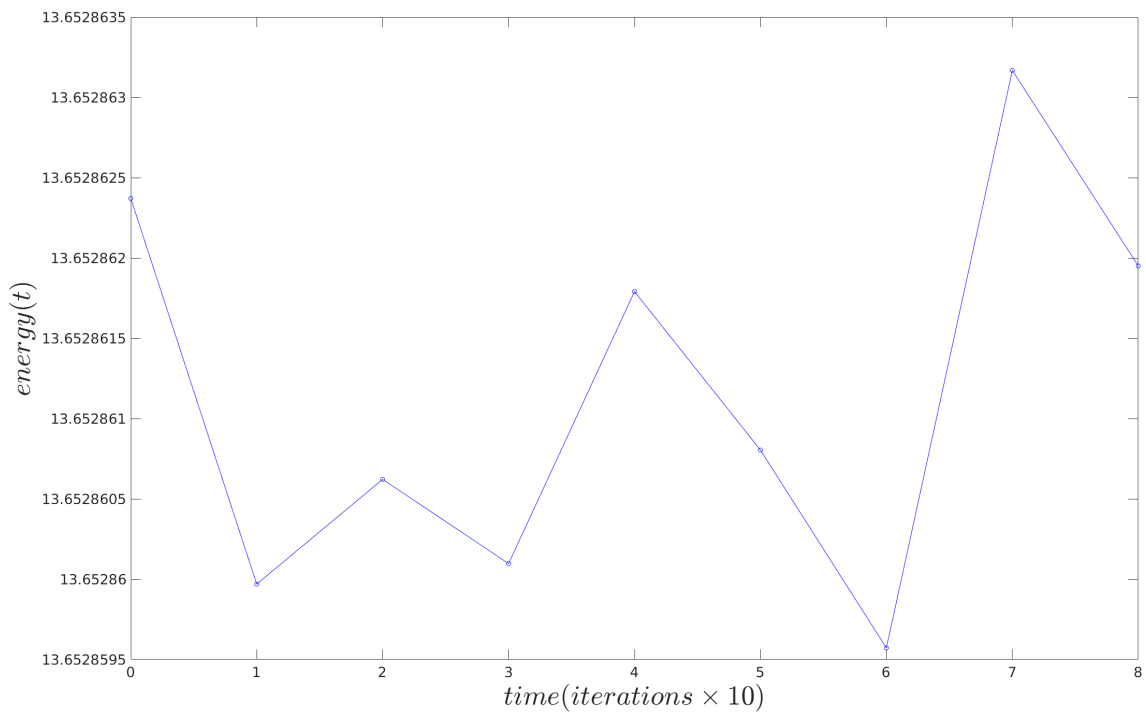
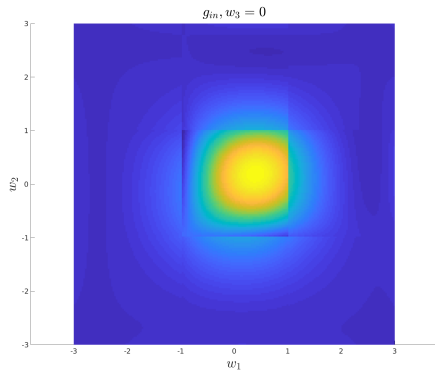
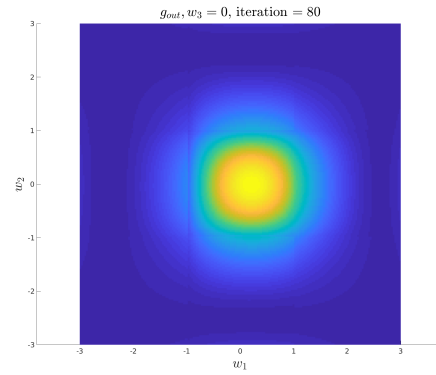


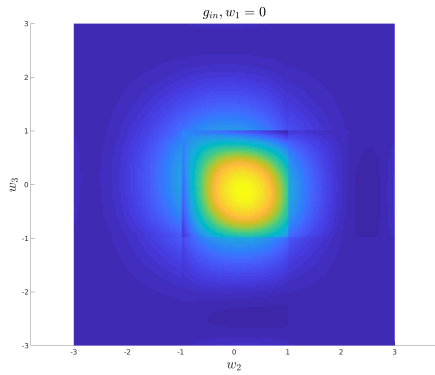
Figure 4.5: Validation Experiment 1 with 27 elements: Energy



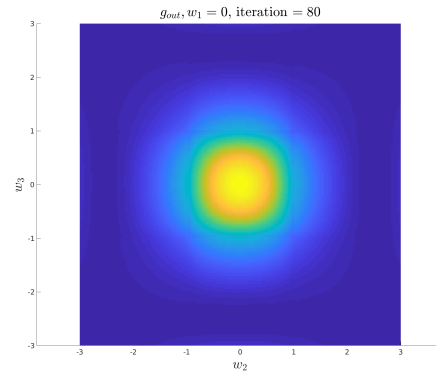
(a) Initial condition on the $w_3 = 0$ surface



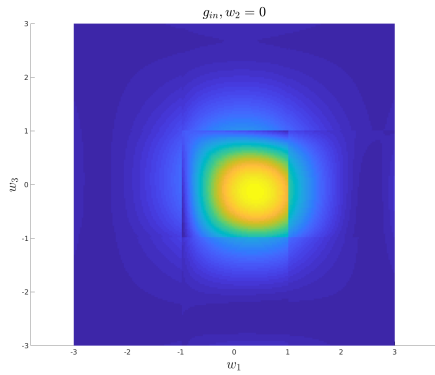
(b) Converged solution on the $w_3 = 0$ surface



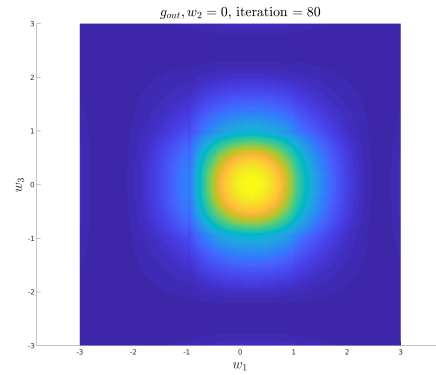
(c) Initial condition on the $w_1 = 0$ surface



(d) Converged solution on the $w_1 = 0$ surface



(e) Initial condition on the $w_2 = 0$ surface



(f) Converged solution on the $w_2 = 0$ surface

Figure 4.6: Validation Experiment 1 with 27 elements: Input and output on different surfaces

The same simulation experiment was run with a 125 element mesh, with a smaller time step, gave us the following solution:

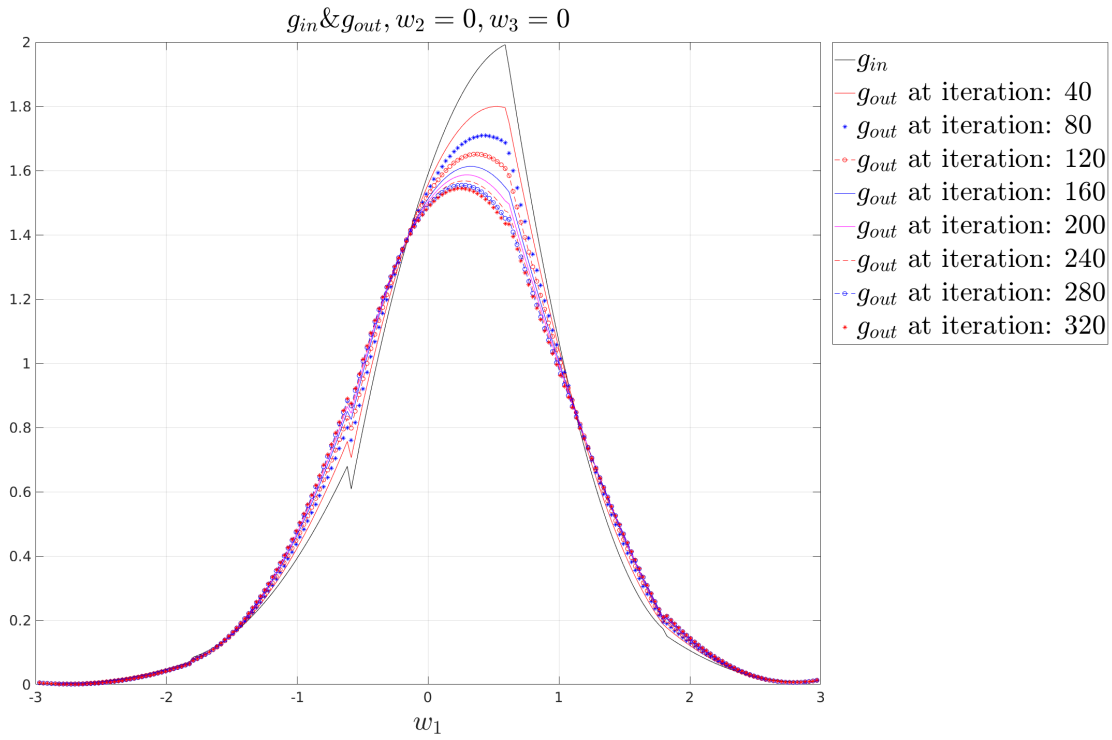


Figure 4.7: Validation Experiment 1 with 125 elements: Evolution of g with $w_2 = w_3 = 0$

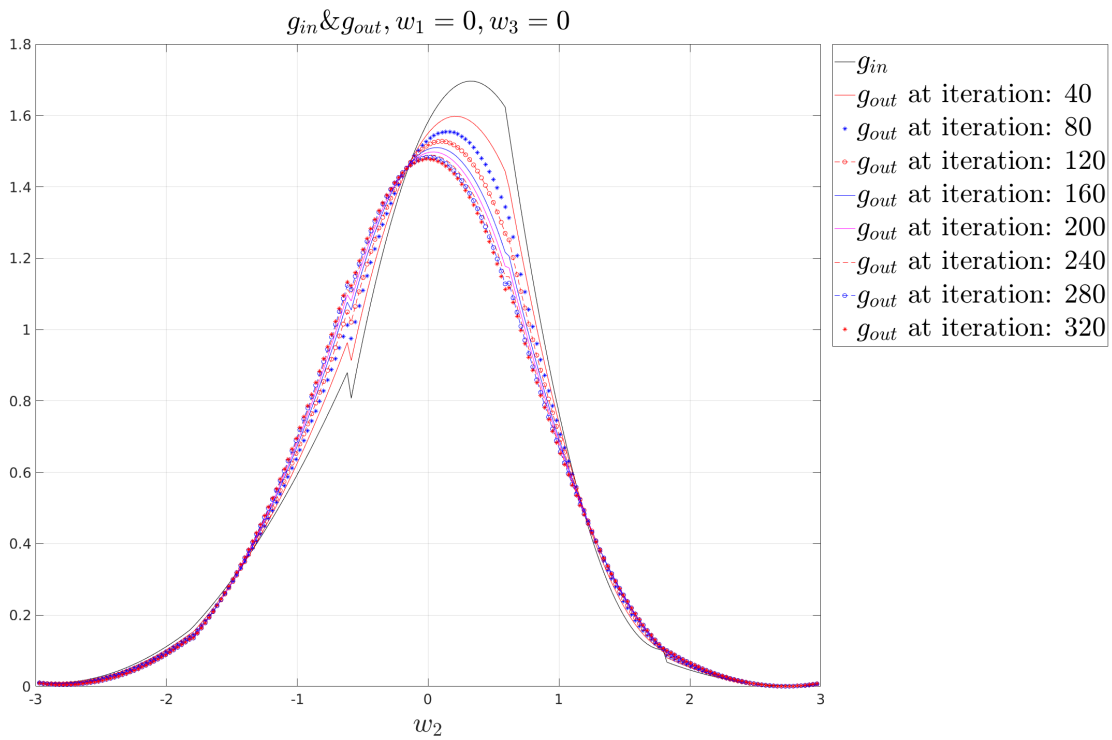


Figure 4.8: Validation Experiment 1 with 125 elements: Evolution of g with $w_1 = w_3 = 0$

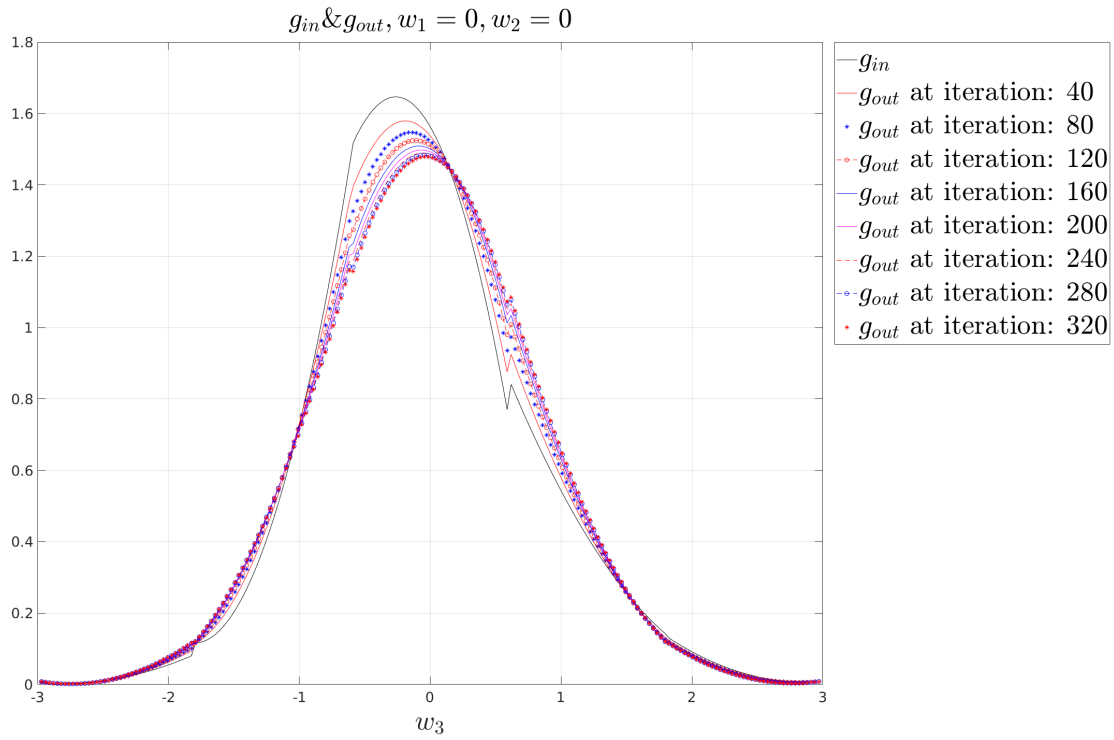


Figure 4.9: Validation Experiment 1 with 125 elements: Evolution of g with $w_1 = w_2 = 0$

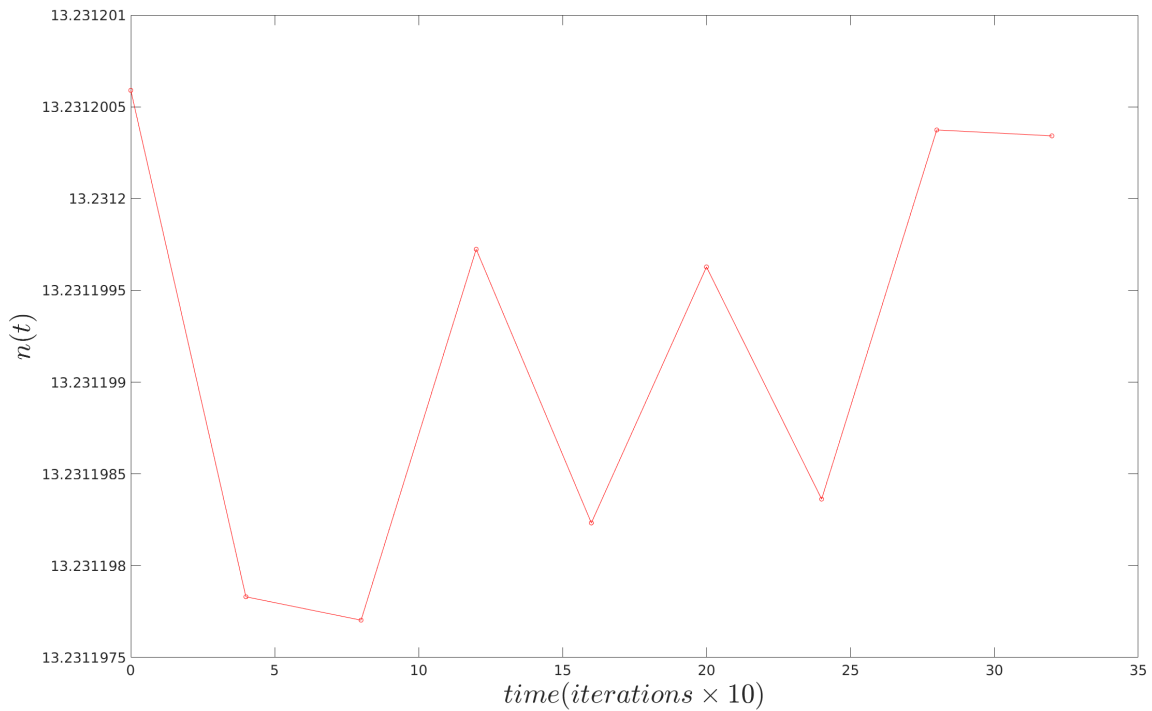


Figure 4.10: Validation Experiment 1 with 125 elements: Number Density

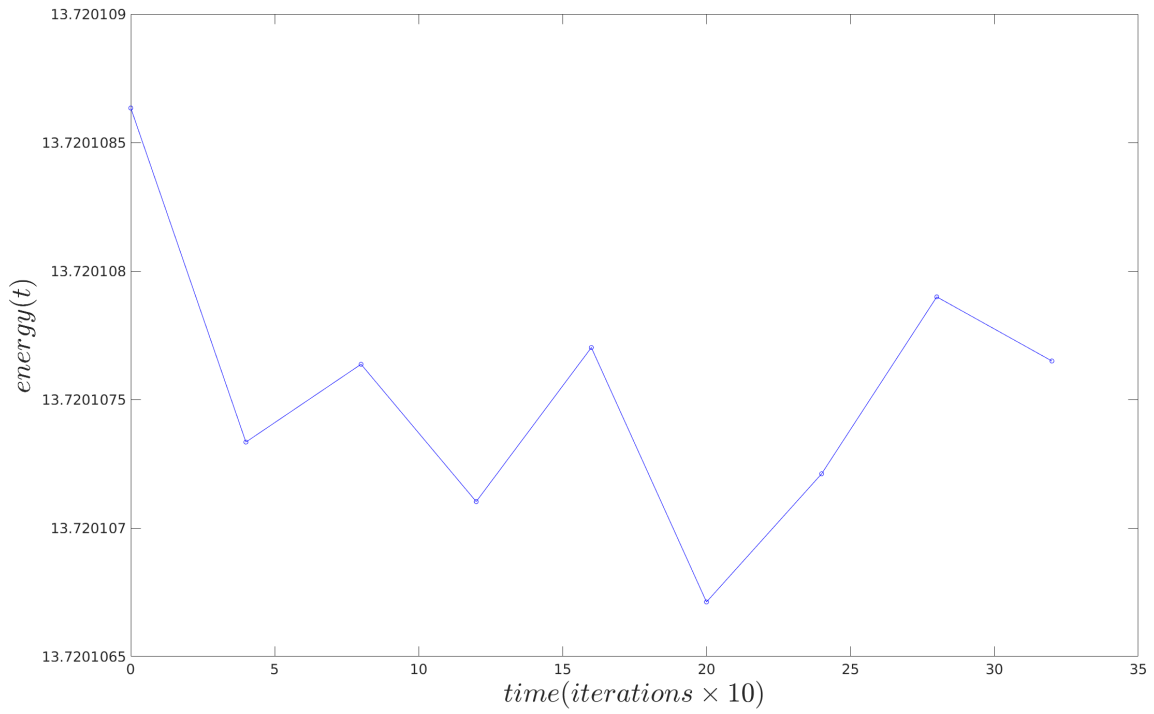
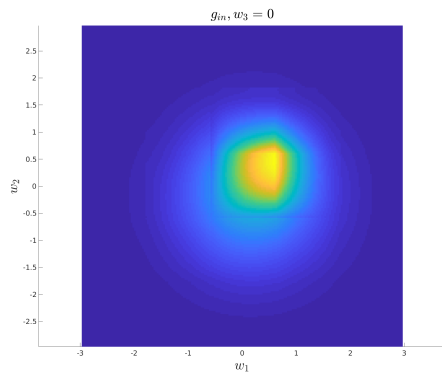
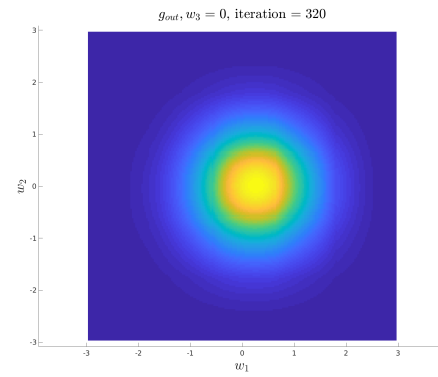


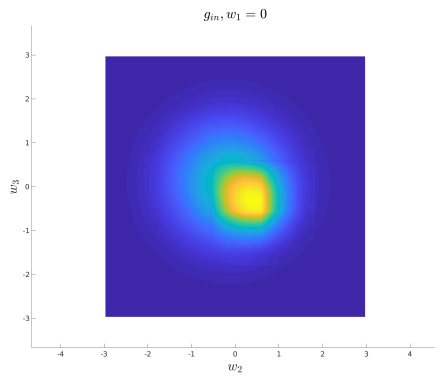
Figure 4.11: Validation Experiment 1 with 125 elements: Energy



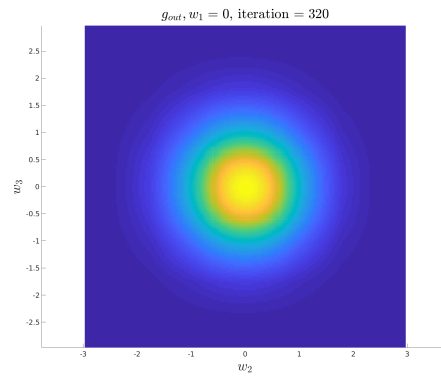
(a) Initial condition on the $w_3 = 0$ surface



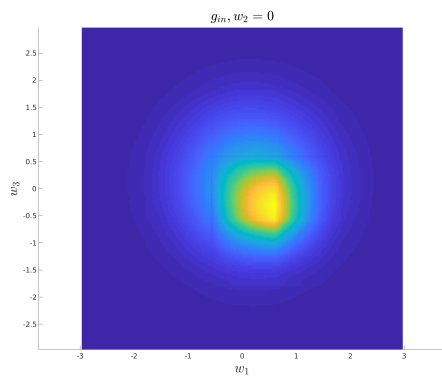
(b) Converged solution on the $w_3 = 0$ surface



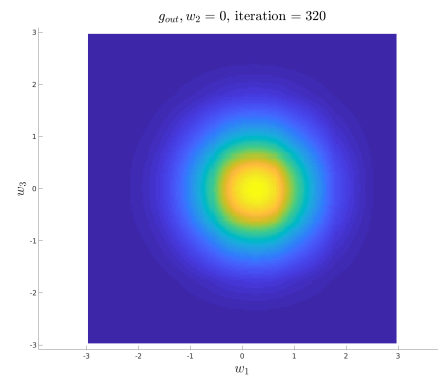
(c) Initial condition on the $w_1 = 0$ surface



(d) Converged solution on the $w_1 = 0$ surface



(e) Initial condition on the $w_2 = 0$ surface



(f) Converged solution on the $w_2 = 0$ surface

Figure 4.12: Validation Experiment 1 with 125 elements: Input and output on different surfaces

4.1.2 Experiment 2

In this experiment we simulate the relaxation of two artificial streams with discontinuous initial data.

The initial data are constructed as a sum of two functions given by:

$$g(t = 0, \mathbf{w}) = \begin{cases} \rho h & |\mathbf{w} - \mathbf{w}_{avg}| \leq r \\ 0 & |\mathbf{w} - \mathbf{w}_{avg}| > r \end{cases} \quad r = 2.0, \quad h = 0.5 \quad (4.1.2.1)$$

The solutions are as follows:

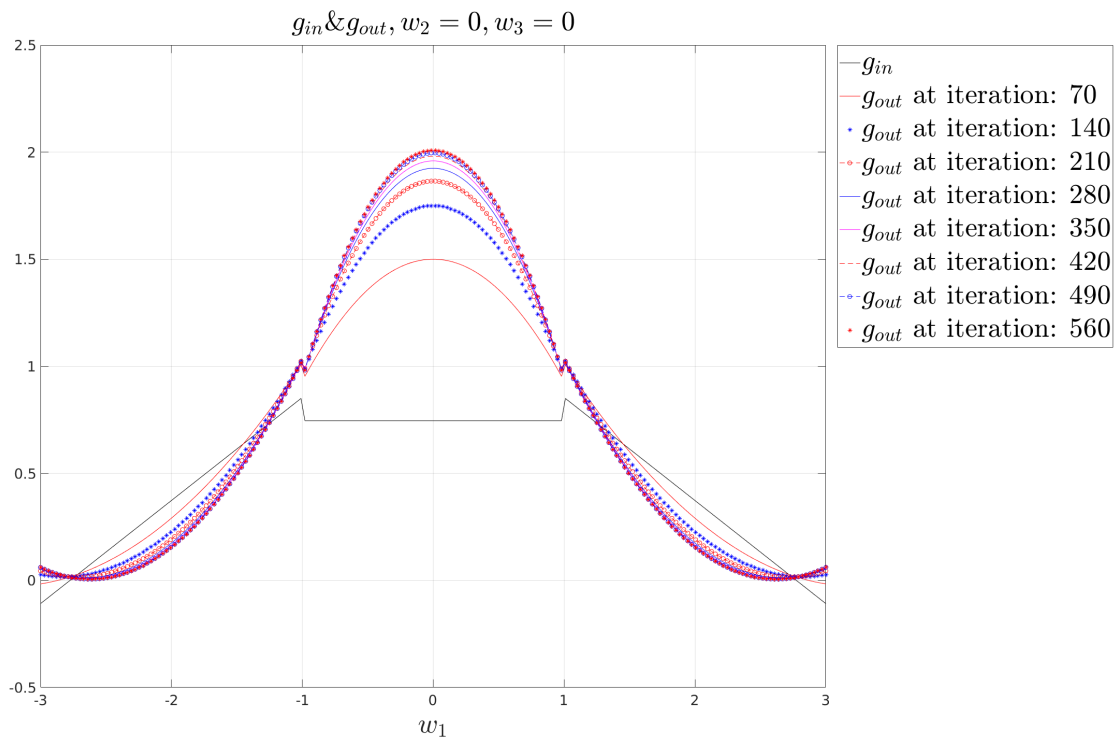


Figure 4.13: Validation Experiment 2 with 27 elements: Evolution of g with $w_2 = w_3 = 0$

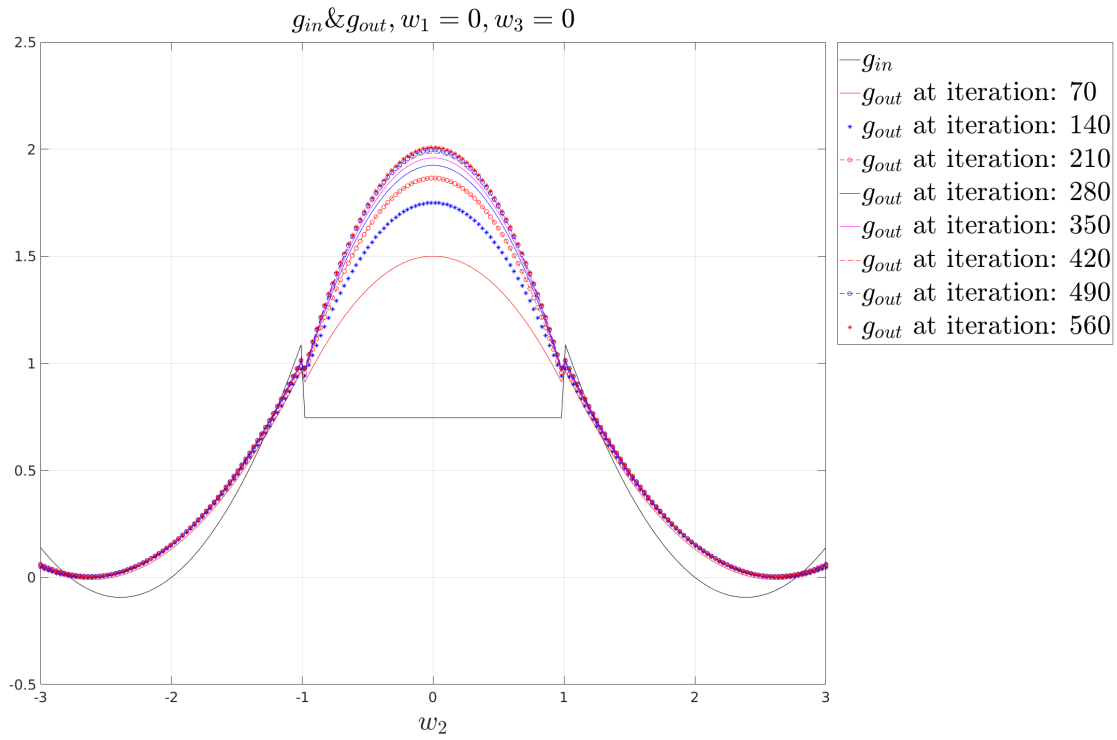


Figure 4.14: Validation Experiment 2 with 27 elements: Evolution of g with $w_1 = w_3 = 0$

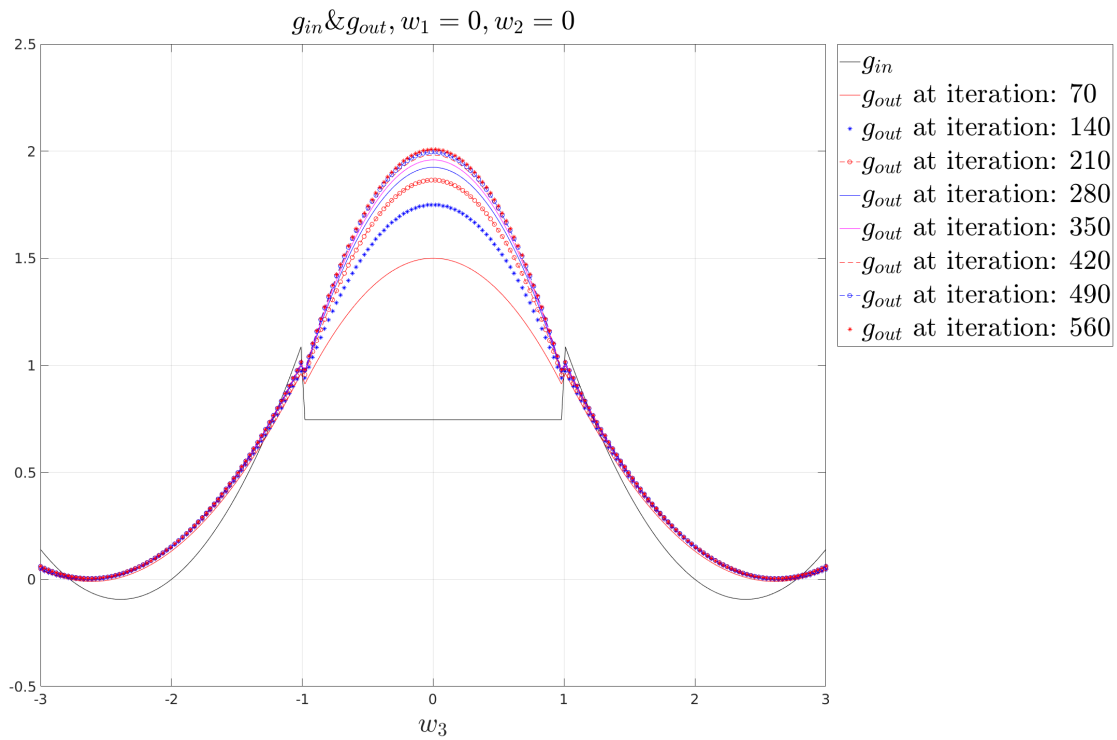


Figure 4.15: Validation Experiment 2 with 27 elements: Evolution of g with $w_1 = w_2 = 0$

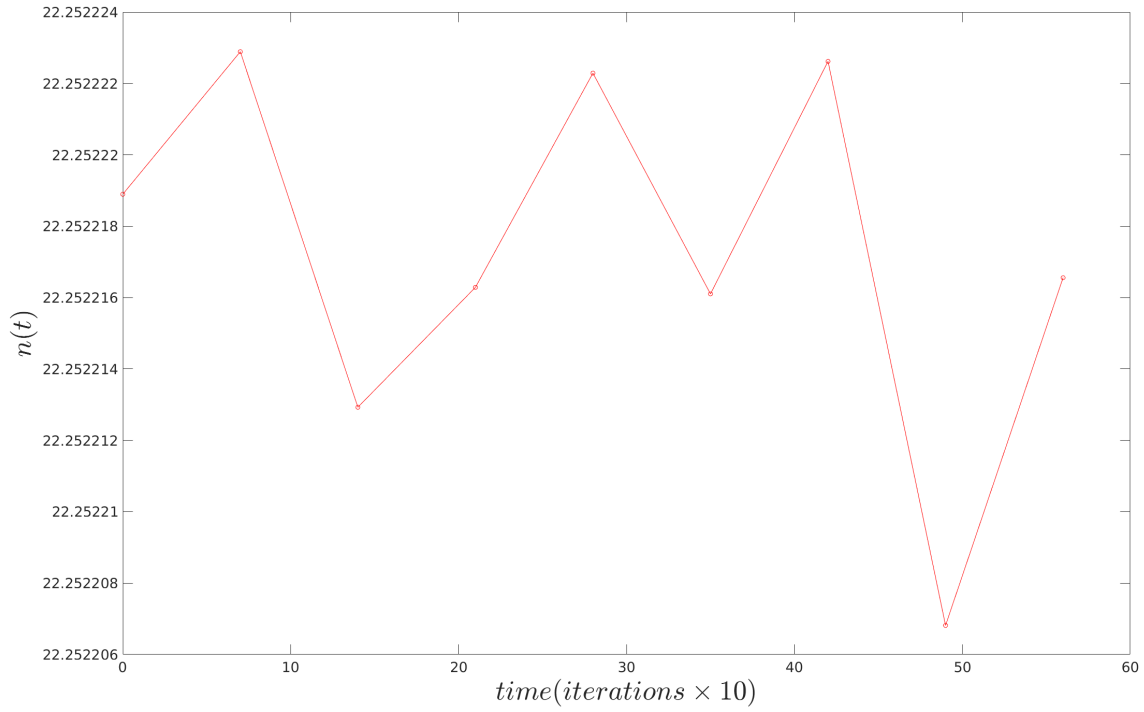


Figure 4.16: Validation Experiment 2 with 27 elements: Number Density

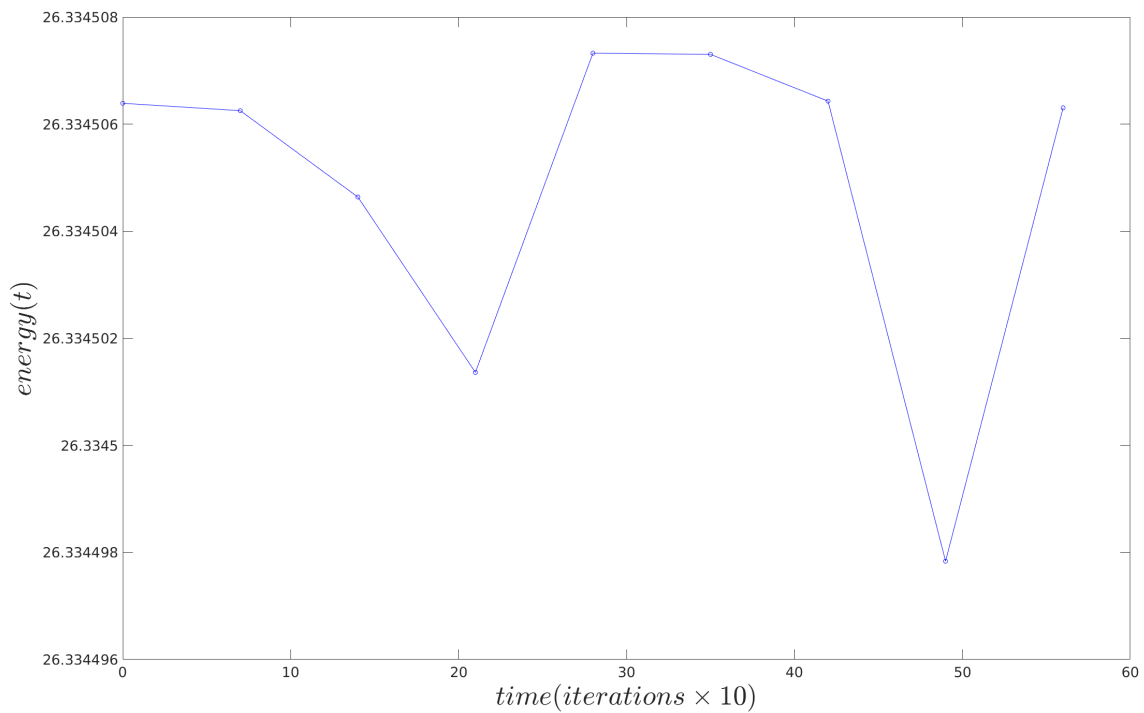


Figure 4.17: Validation Experiment 2 with 27 elements: Energy

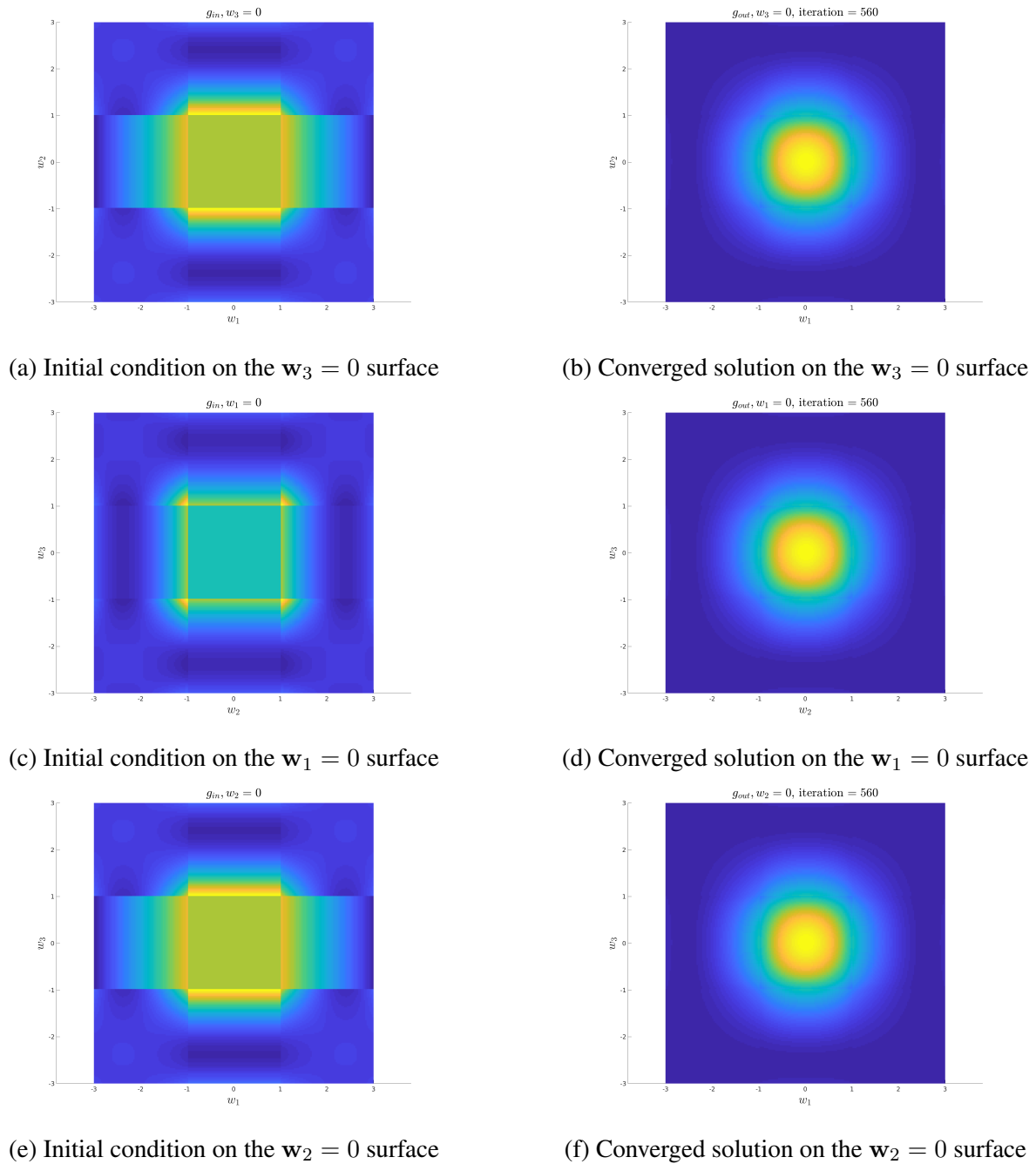


Figure 4.18: Validation Experiment 2 with 27 elements: Input and output on different surfaces

The same experiment run with a 125 element mesh gave us the following solution:

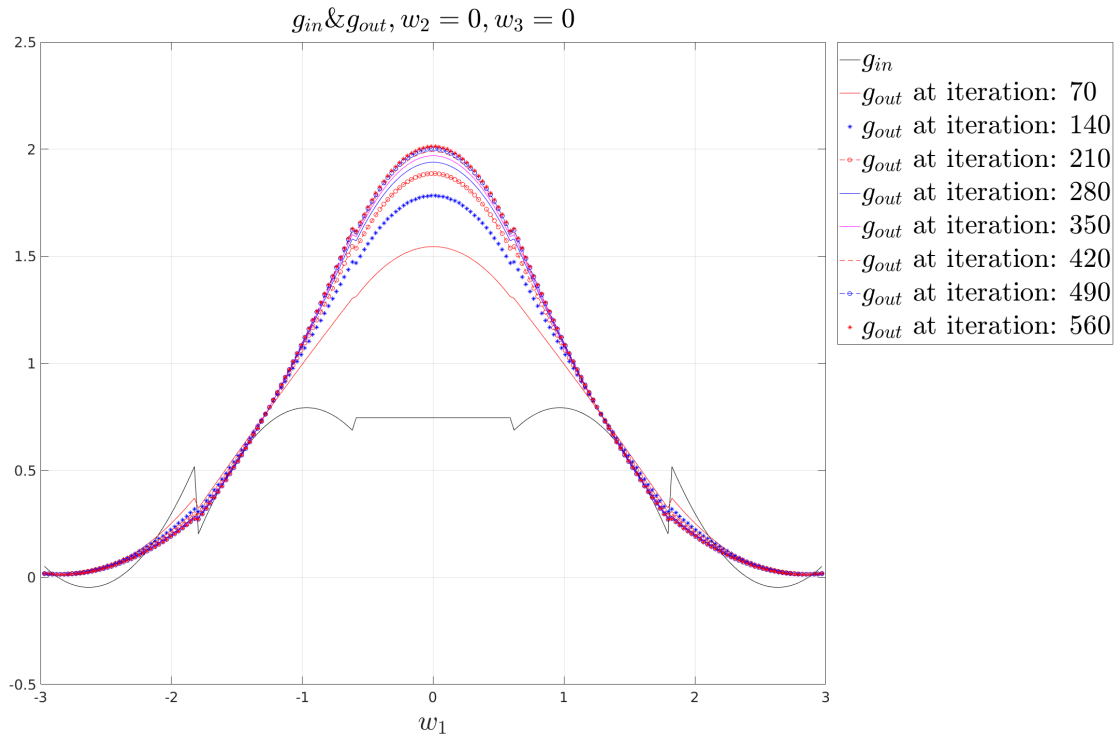


Figure 4.19: Validation Experiment 2 with 125 elements: Evolution of g with $w_2 = w_3 = 0$

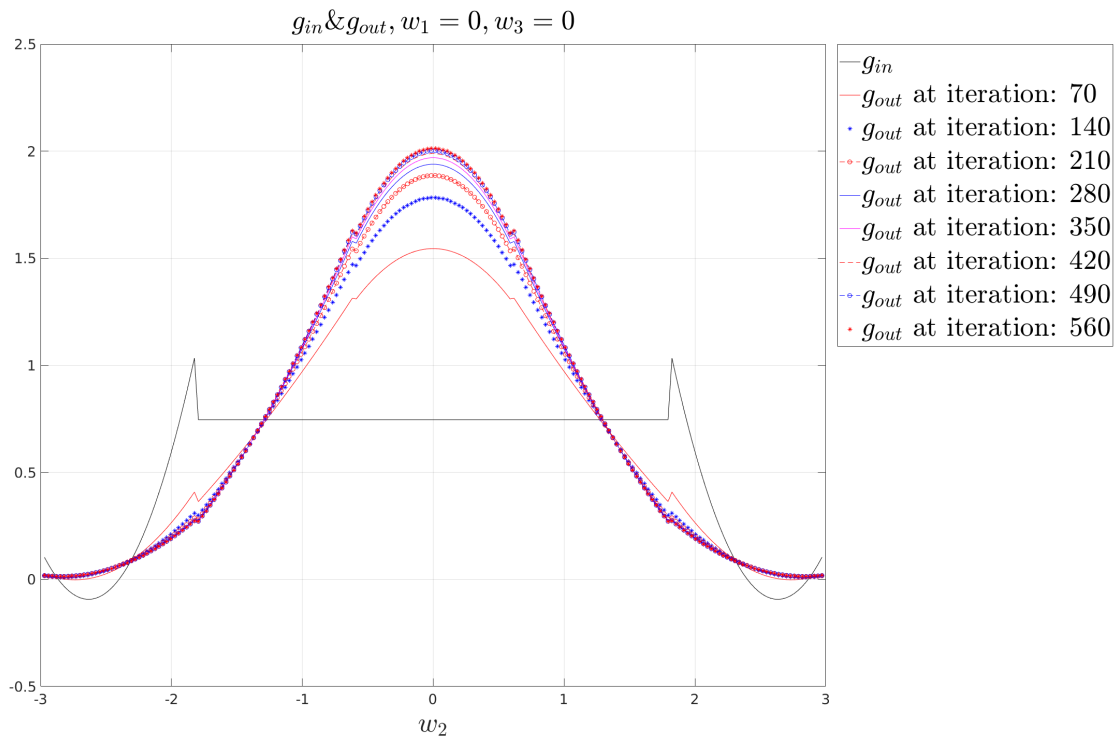


Figure 4.20: Validation Experiment 2 with 125 elements: Evolution of g with $w_1 = w_3 = 0$

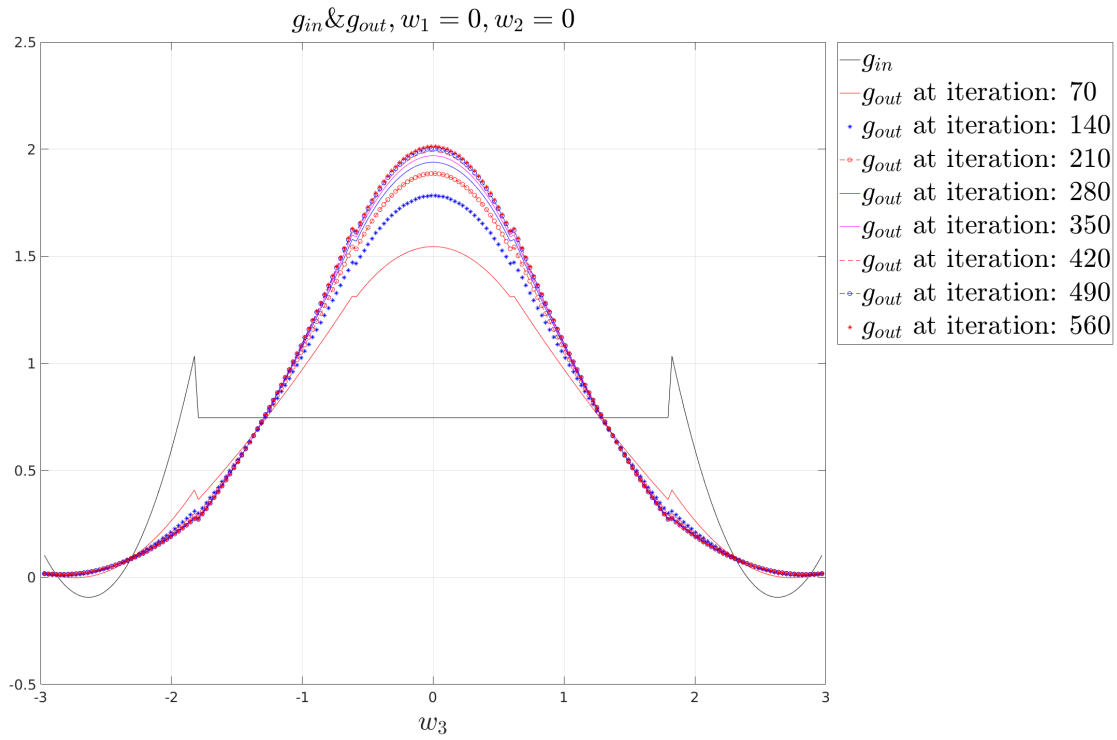


Figure 4.21: Validation Experiment 2 with 125 elements: Evolution of g with $w_1 = w_2 = 0$

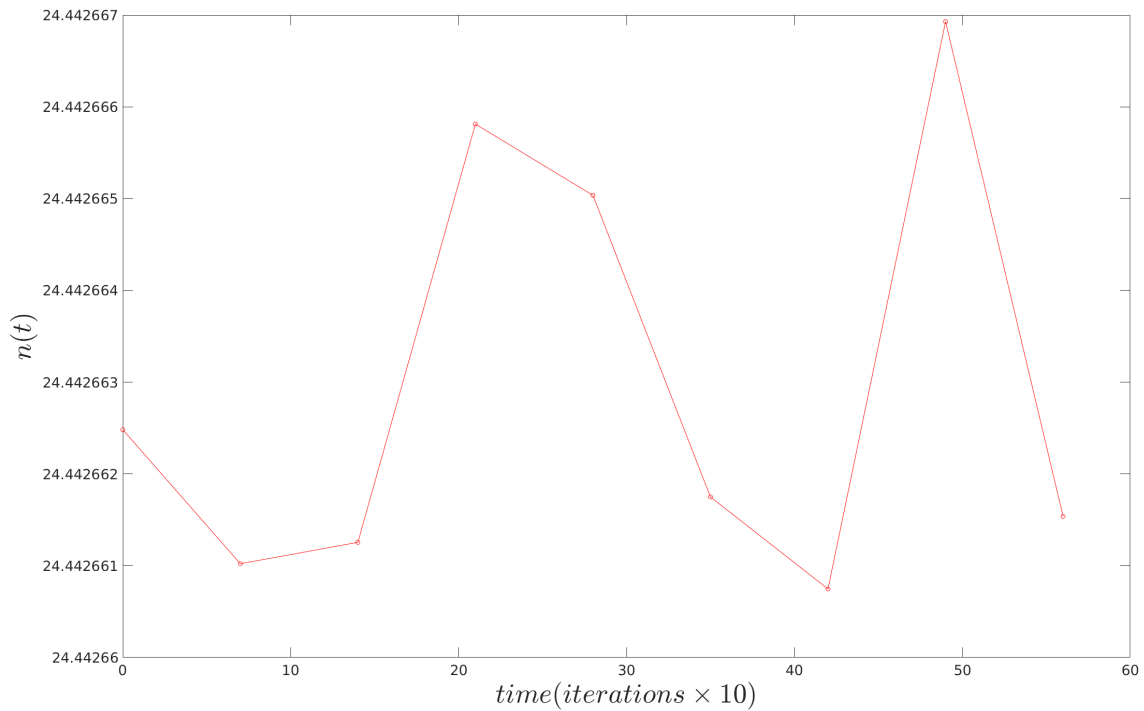


Figure 4.22: Validation Experiment 2 with 125 elements: Number Density

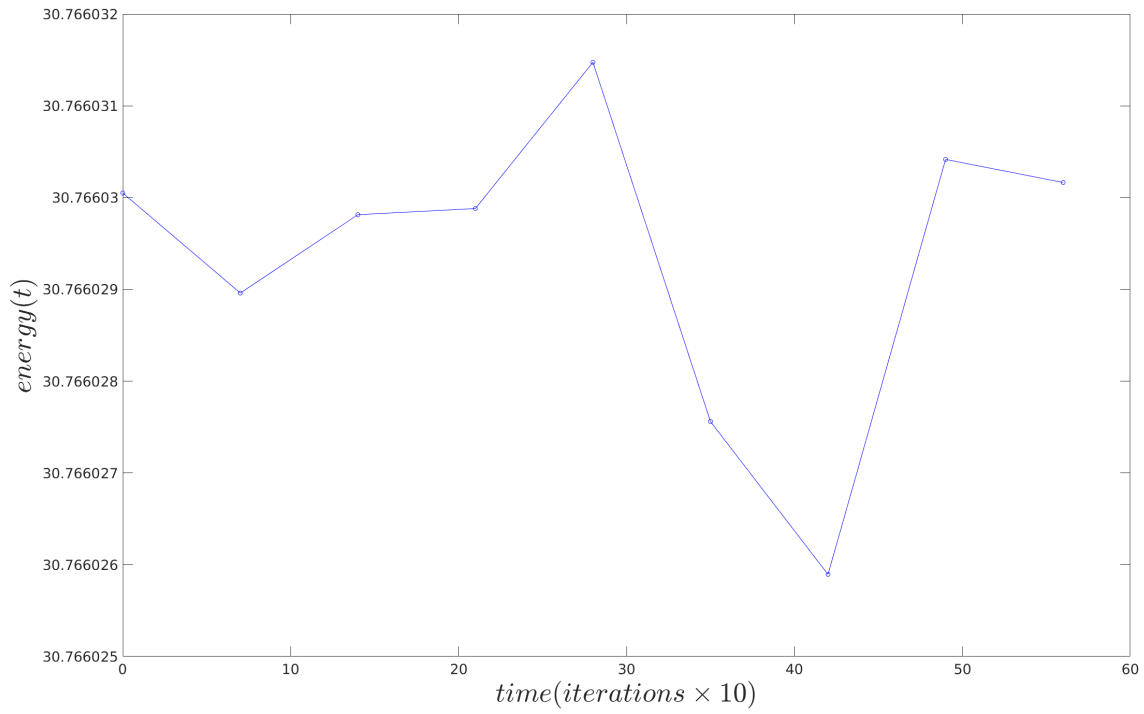


Figure 4.23: Validation Experiment 2 with 125 elements: Energy

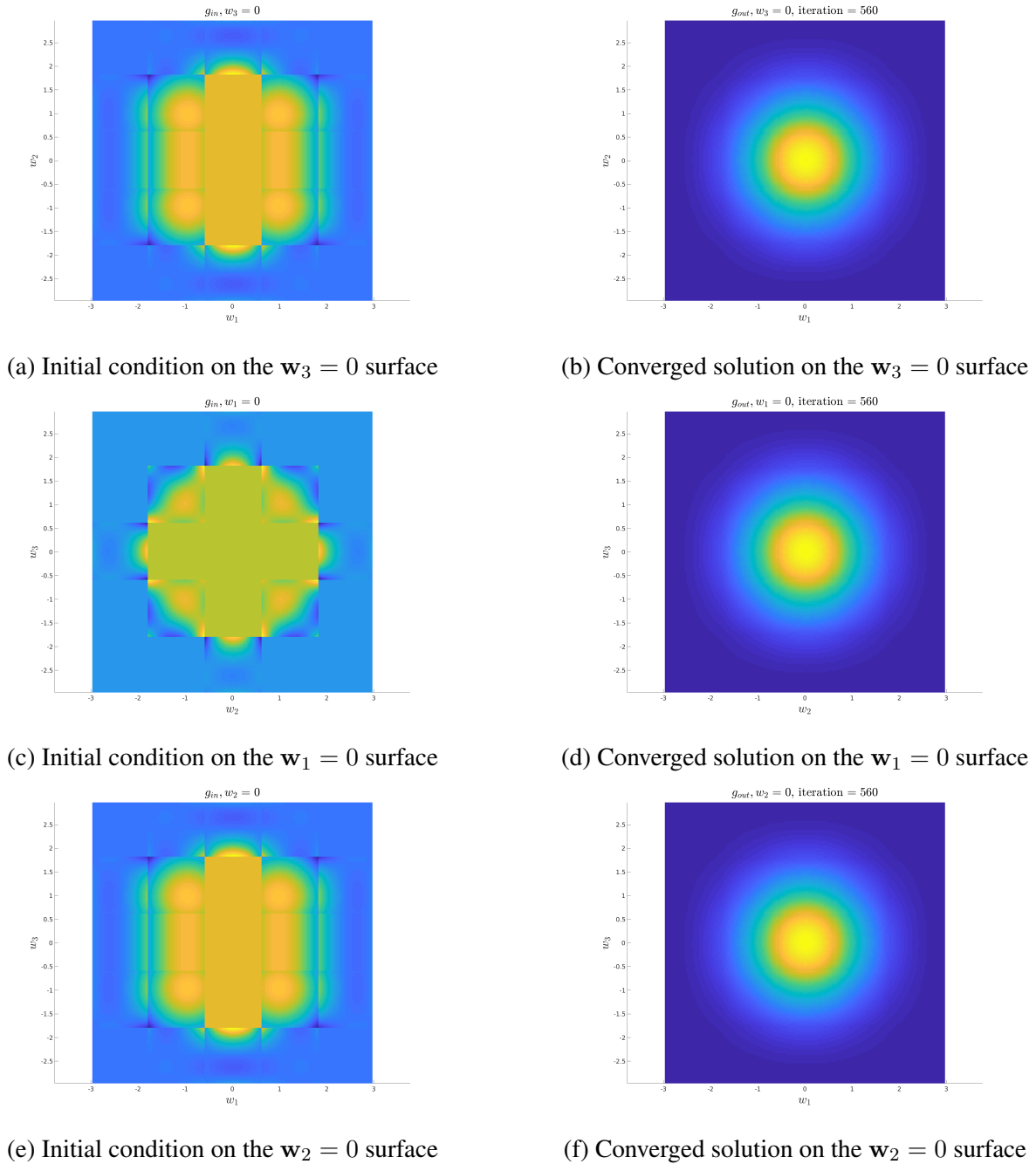


Figure 4.24: Validation Experiment 2 with 125 elements: Input and output on different surfaces

We observe that equilibration of two Gaussians or some discontinuous data as initial conditions, the mixture relaxes and converges to a single Gaussian. The sharp bents/discontinuities in the solution that are visible at the edges of the elements are because of the discontinuous nature of our shape functions over element edges, which reduce with the increase in the number of elements. The solutions produced by a 125 element mesh (5 in each velocity dimension) Figure 4.12 and Figure 4.24 are much smoother

as compared to a 27 element mesh (3 in each velocity dimension) as can be seen in Figure 4.6 and Figure 4.18. It could be observed that the energy and the number density remains almost constant throughout the entire relaxation period and the values of both the 27 element cases and the 125 element ones are in accordance with each other up to a good extent.

These two validation experiments §4.1.1 and §4.1.2 proves the correctness of the computation and code of the Collision operator, *i.e.* the RHS of the reduced Boltzman equation (2.6.0.3) which is pre-computed and stored (because of its time independence) to perform time integration later on.

4.2 Method of Manufactured Solution

The Method of Manufactured Solutions or commonly known as MMS in Computational Science is a technique to verify the correctness of the code developed to solve a governing mathematical equation. Code verification is an early and indispensable step in building certainty within the prescient capability of simulation softwares. MMS is a generalized technique used to build analytical solutions the governing differential equations that form the premise for the simulation code. The analytical solution, which might not make physical sense, could be used to benchmark solutions for verification tests.

The implementation of MMS is theoretically straightforward. The differential equation (or a system of differential equations) for which the code is to be verified is considered,

$$D(\Omega) = 0 \tag{4.2.0.1}$$

where Ω is the unknown scalar variable (could as well be a vector of the unknown variables) in our case and $D(\cdot)$ is the differential operator. Subsequently, a function $\hat{\Omega}$, with sufficient differentiability and satisfying all boundary and initial conditions, is chosen. The chosen function $\hat{\Omega}$, would necessarily, and in general, not satisfy the governing equation(s) (4.2.0.1) exactly and hence a corresponding set of source term(s) S_{Ω} gets “manufactured” in order to balance the system and we get a new system of

equation(s):

$$D\left(\hat{\Omega}\right) = S_{\Omega} \quad (4.2.0.2)$$

Now numerical solvers of (4.2.0.1) could be tested using (4.2.0.2) by adding a minimal code to compute the source term(s)[40].

4.2.1 Manufactured Solution for the reduced Boltzmann equation

The LHS of the reduced boltzman equation (2.6.0.3) code is tested using the method of Manufactured soultions. We consider the equation (4.2.1.1)

$$\frac{\partial g}{\partial t} + \mathbf{p} \cdot \frac{\partial g}{\partial \mathbf{w}} = 0 \quad (4.2.1.1)$$

and substitute the solution with (4.2.1.2) (which satisfies the initial conditions and the bounary condi-tions of our problem at all times),

$$g(t, \mathbf{w}) = \sin(t) \exp(-|\mathbf{w}|^2) \quad (4.2.1.2)$$

and obtain the equation (4.2.1.3)

$$\frac{\partial g}{\partial t} + \mathbf{p} \cdot \frac{\partial g}{\partial \mathbf{w}} = f_* \quad (4.2.1.3)$$

where f_* becomes,

$$f_* = \exp(-|\mathbf{w}|^2) (\cos(t) - 2 \sin(t) (\mathbf{w} \cdot \mathbf{p})) \quad (4.2.1.4)$$

Now, on testing our code for time integration (5th order Adams-Bashforth code) with the above equations we observe that we get back our originally assumed solution as time evolves with very small margins of error.

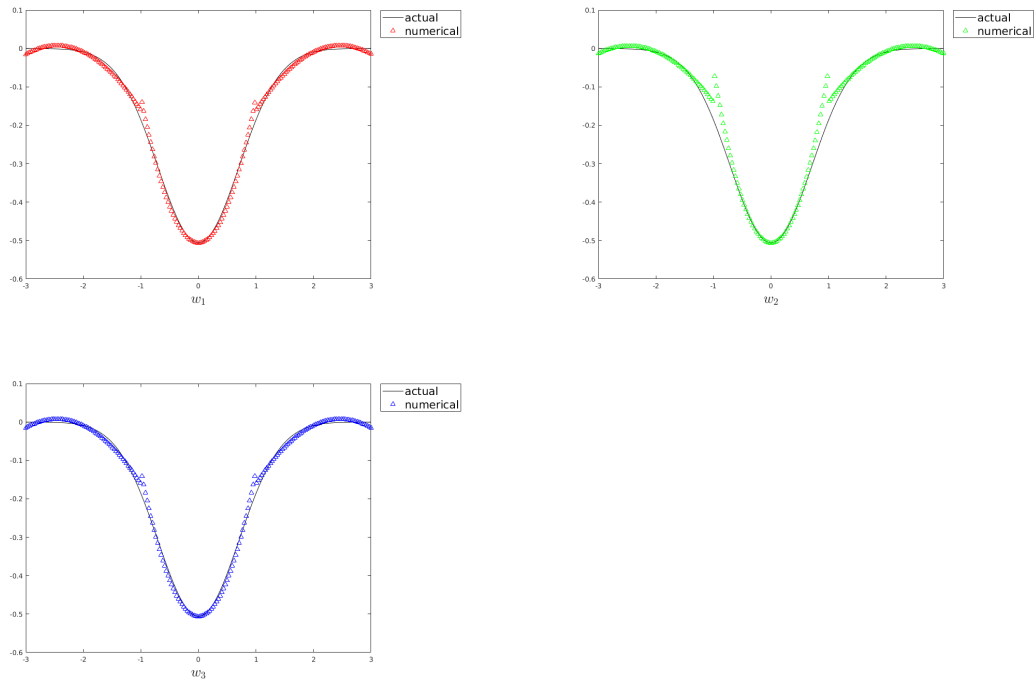


Figure 4.25: Manufactured solution experiment: Solution at 100000 iterations

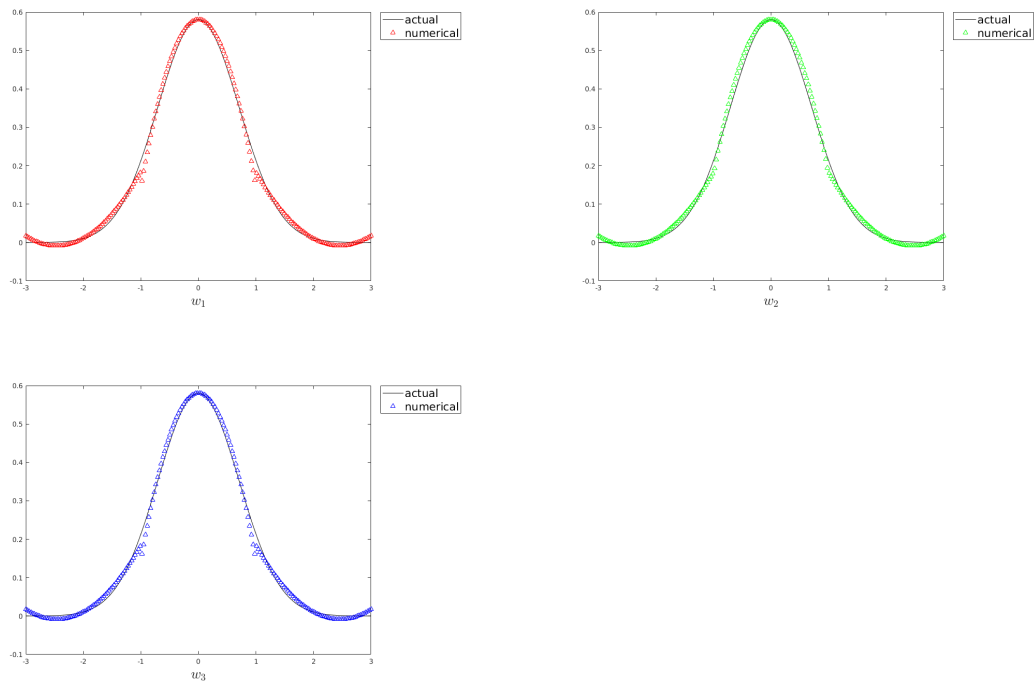


Figure 4.26: Manufactured solution experiment: Solution at 120000 iterations

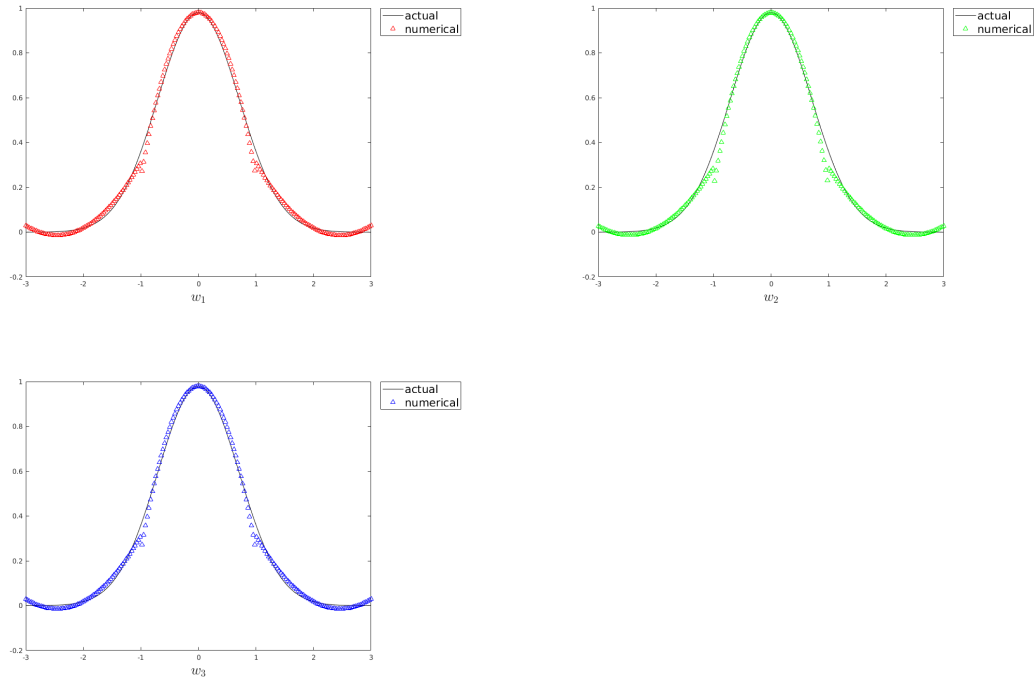


Figure 4.27: Manufactured solution experiment: Solution at 140000 iterations

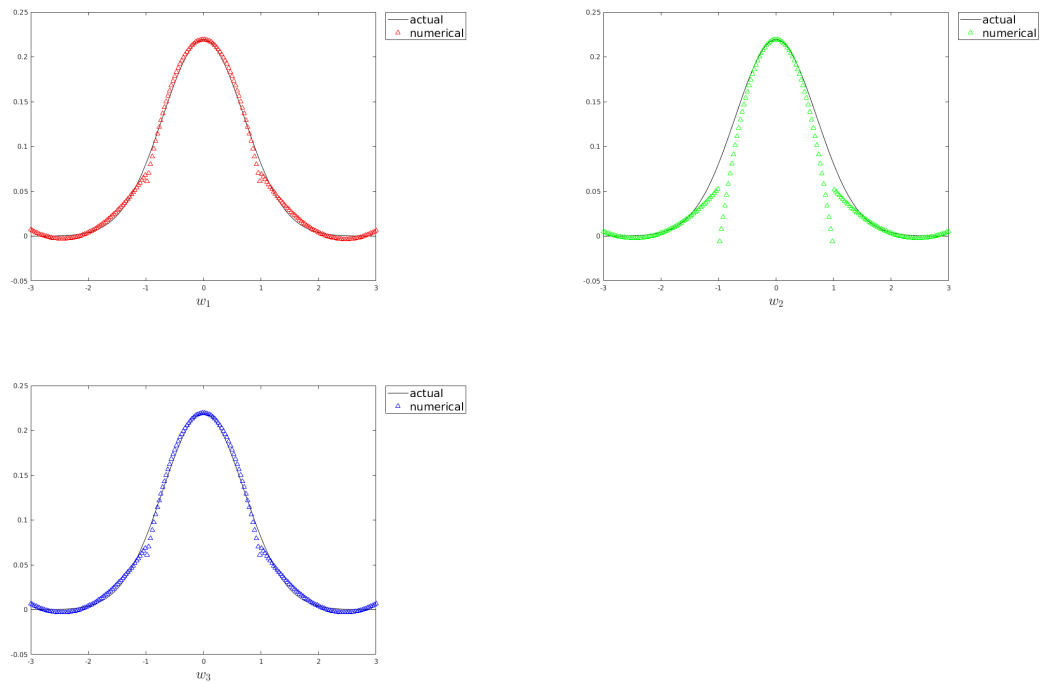


Figure 4.28: Manufactured solution experiment: Solution at 160000 iterations

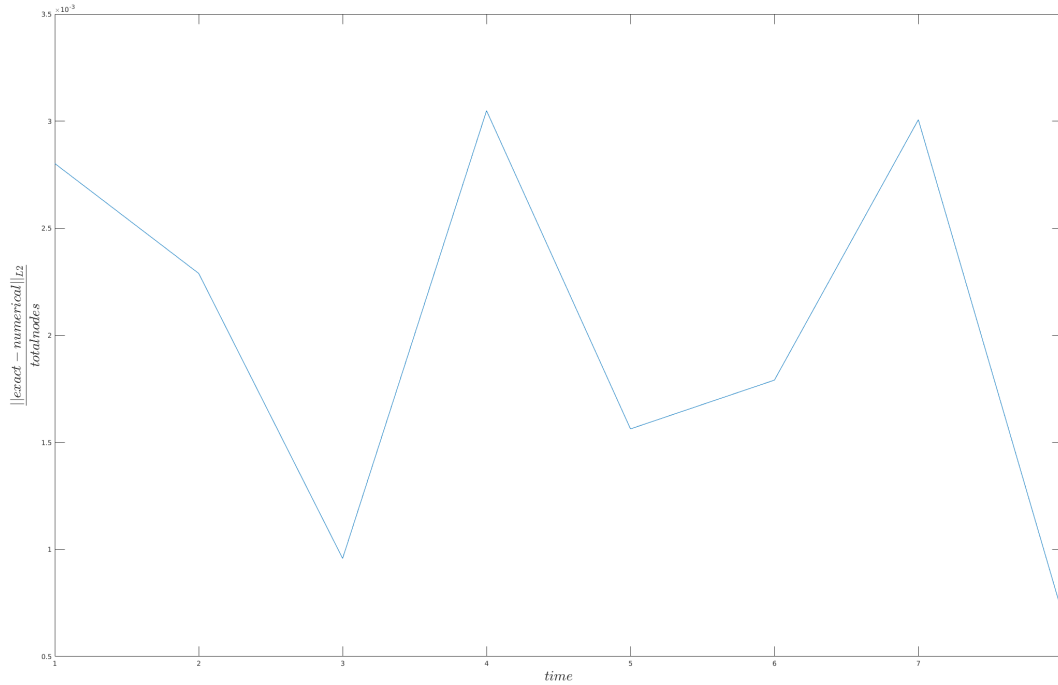


Figure 4.29: Manufactured solution experiment: Error at regular time intervals

We observe that the symmetry among the different sections of the solution breaks because of the shear rate imposed along $\mathbf{l}_1 \otimes \mathbf{l}_2$ direction. We had taken $A = 0.8\mathbf{l}_1 \otimes \mathbf{l}_2$ for the Manufactured solution testing.

At this point, we could argue that the code has been verified to a good extent. The convergence of combined steady-state streams to equilibrium accounts for the correctness of the computation of the Collision operator and so does MMS for the correctness of the LHS of the Boltzmann Equation. The complicated nature of the Collision operator did not allow us to verify the entire Boltzmann equation with MMS. The code is verified even further in the following way. As we know that the Boltzmann Equation is an approximation of the Molecular Dynamics method, we run simulations with different values of \mathbf{A} for different kinds of flows, with proper boundary conditions, and compare our results using LAMMPS.

Chapter 5

Results and Discussion

So far we have looked at steady states with $\mathbf{A} = 0$ in the equation (2.6.0.3). Now we would be looking for solutions in the non-equilibrium regime of flows.

5.1 Non-equilibrium flows

These example flows could be visualized as shown in Figure 5.30 and Figure 5.31. The statistics (the velocity distribution function to be precise) of gas flows characterized by different forms of the 3×3 matrix \mathbf{A} have been observed with the reduced form of the Boltzmann Equation (2.6.0.3). Figure 5.30 is an example of how the periodic boundary condition would be deforming in case of incompressible flows. The motions of all other particles in the system (could be infinitely many) would have a mapping from that of the simulated ones using the action, (2.3.0.1). For example, we would be simulating the particles, $\mathbf{x}_{0,k}$, and for all other particles, $\nu = \mathbb{Z} \setminus 0$, the mapping of their motion could be obtained using (2.3.0.1). It implies that if the velocity of the particle at the origin of physical space is \mathbf{v} then the velocity of the particle at some other position \mathbf{x} is given by $\mathbf{v} + \mathbf{A}(\mathbf{I} + t\mathbf{A})^{-1}\mathbf{x}$.

5.2 Simple Shear

In [14], section §5.3.1 show that Plane Couette flow could exactly be represented by OMD, for $\mathbf{A} = \dot{\gamma} \mathbf{l}_1 \otimes \mathbf{l}_2$. They explain that the method of OMD specialized to the case of plane Couette flow is a significant generalization of the famous work by Lees and Edwards[30]. If $\mathbf{A} = \mathbf{a} \otimes \mathbf{n}$ with $\mathbf{a} \cdot \mathbf{n} = 0$, considering orthonormal vectors $\mathbf{e}_1, \mathbf{e}_3$, \mathbf{a} and \mathbf{n} could be written as $\mathbf{a} = |\mathbf{a}| \mathbf{e}_1, \mathbf{n} = |\mathbf{n}| \mathbf{e}_3$. Substituting $\dot{\gamma} = |\mathbf{a}| |\mathbf{n}|$, the Eulerian velocity field translates to:

$$\mathbf{v} = \mathbf{A} (\mathbf{I} + t\mathbf{A})^{-1} \mathbf{x} = (\dot{\gamma} \mathbf{e}_1 \otimes \mathbf{e}_3) (\mathbf{I} - \dot{\gamma} \mathbf{e}_1 \otimes \mathbf{e}_3) \mathbf{x} = \dot{\gamma} x_3 \mathbf{e}_1 \quad (5.2.0.1)$$

In this experiment, we simulate a gas at equilibrium with an imposition of a shear strain to observe the development of a Couette Flow. We run this experiment for a steady Gaussian as the initial condition and a dimensionless shear rate of $\dot{\gamma} = 0.8$.

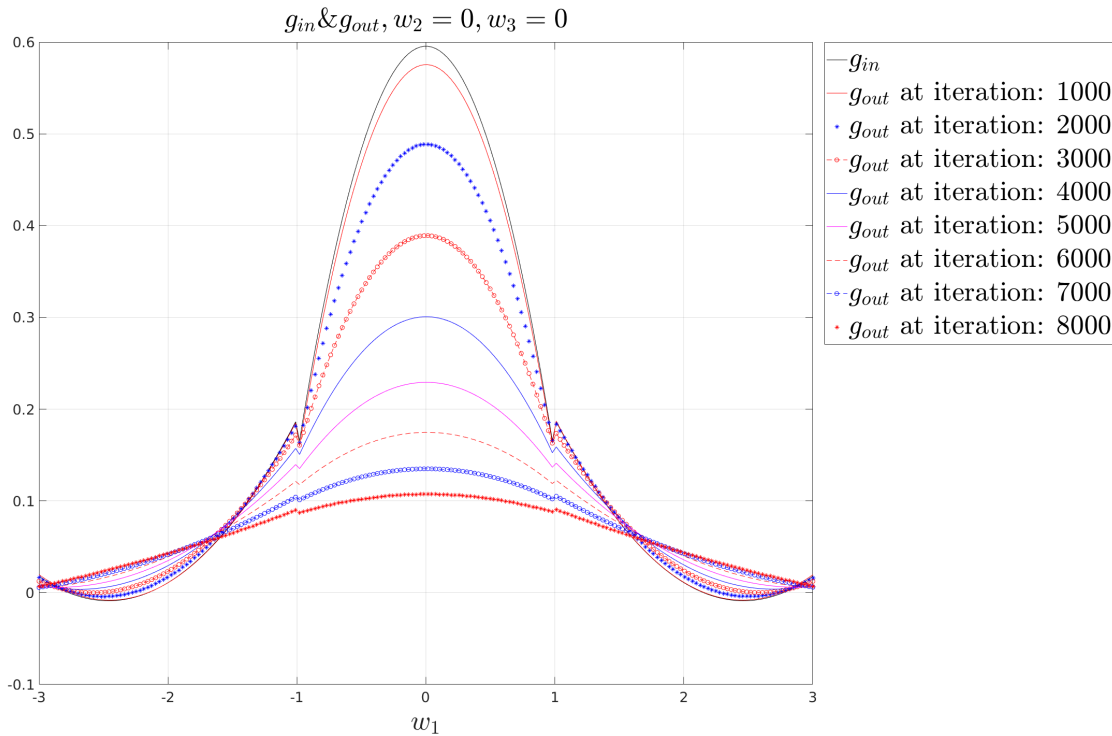


Figure 5.1: Experiment 1 with 27 Elements: Evolution of g with $w_2 = w_3 = 0$

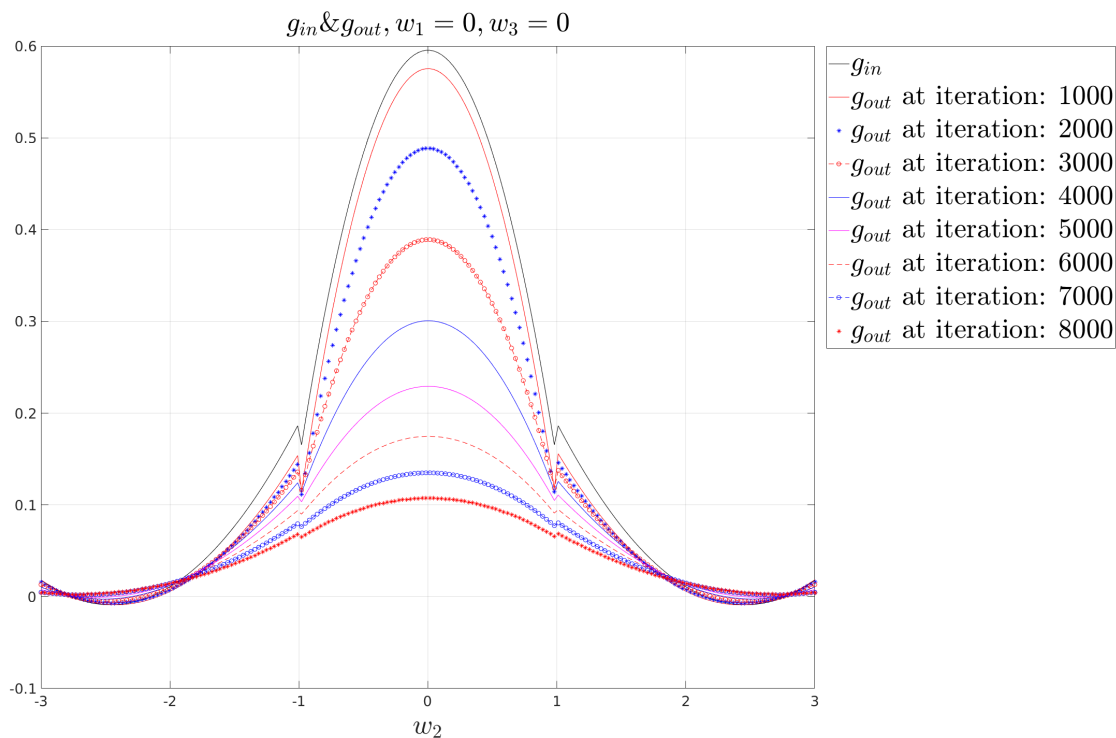


Figure 5.2: Experiment 1 with 27 Elements: Evolution of g with $w_1 = w_3 = 0$

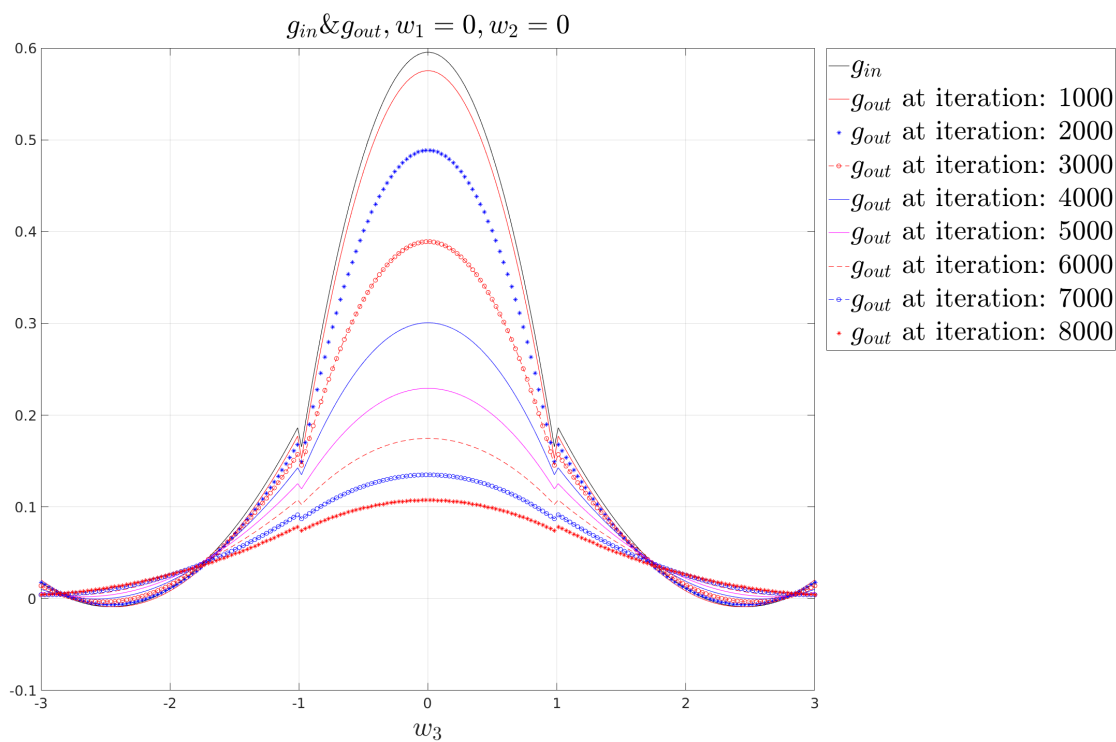


Figure 5.3: Experiment 1 with 27 Elements: Evolution of g with $w_1 = w_2 = 0$

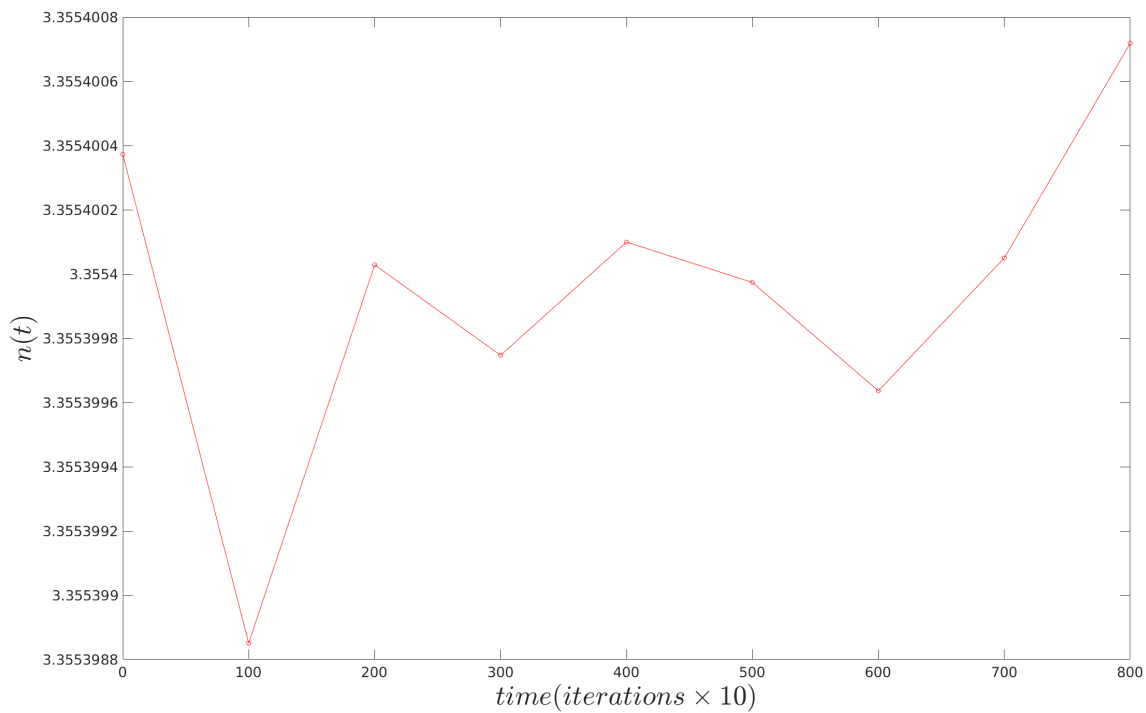


Figure 5.4: Experiment 1 with 27 Elements: Number Density

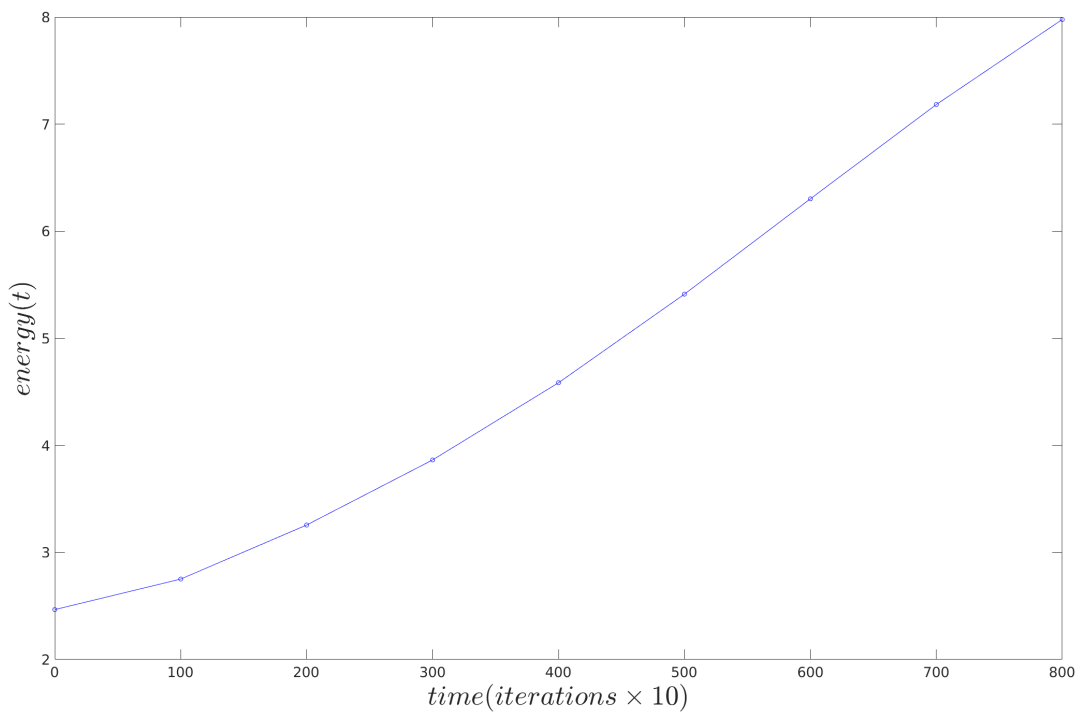
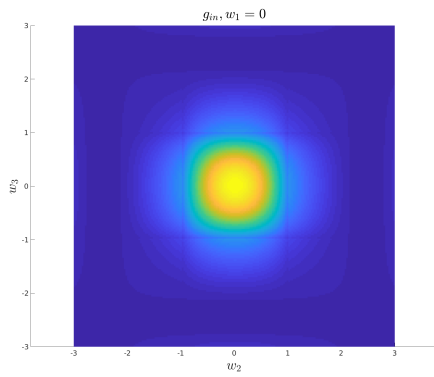
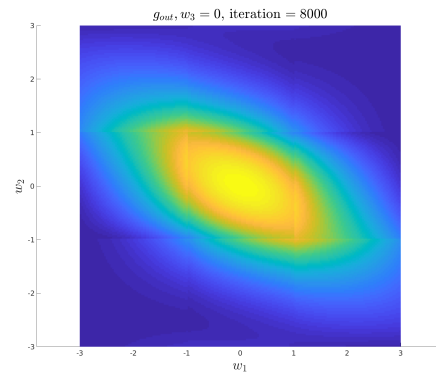


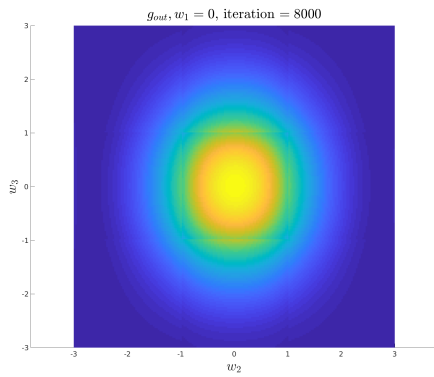
Figure 5.5: Experiment 1 with 27 Elements: Energy



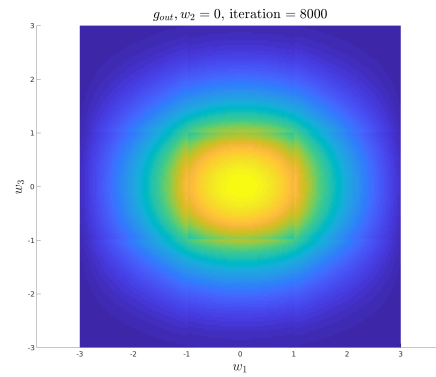
(a) Initial condition on the $w_1 = 0$ surface



(b) Converged solution on the $w_3 = 0$ surface



(c) Converged solution on the $w_1 = 0$ surface



(d) Converged solution on the $w_2 = 0$ surface

Figure 5.6: Experiment 1 with 27 Elements: Input and output on different surfaces

This simulation was run with 125 elements as well.

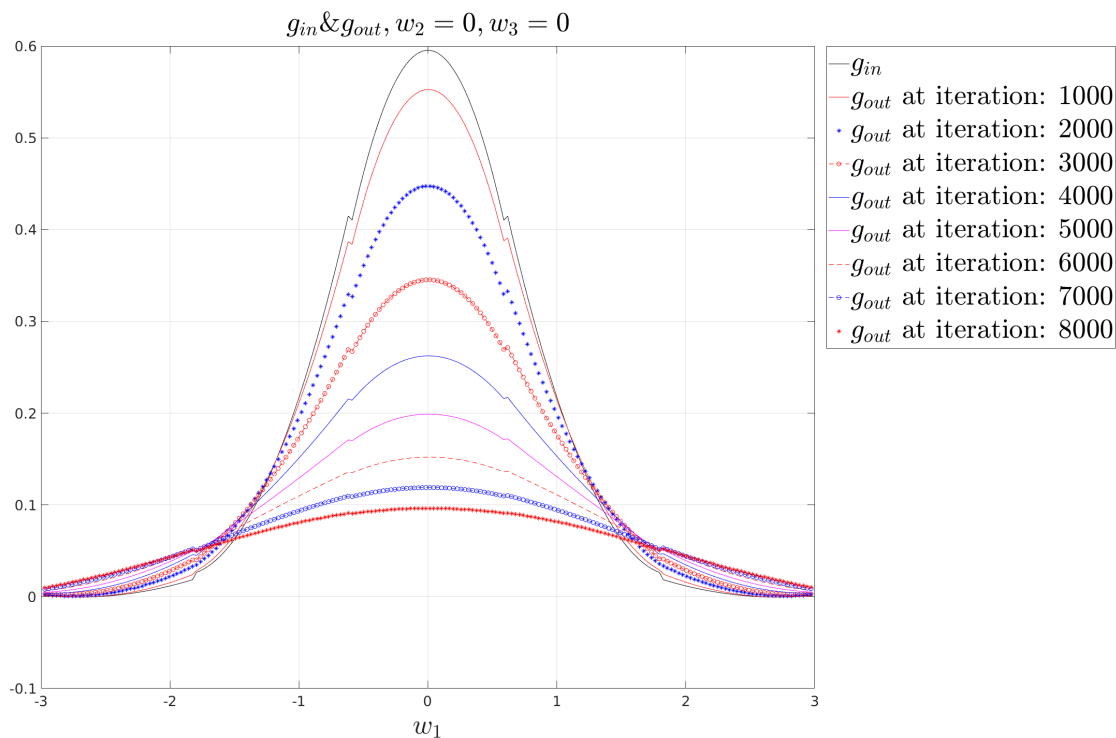


Figure 5.7: Experiment 1 with 125 Elements: Evolution of g with $w_2 = w_3 = 0$

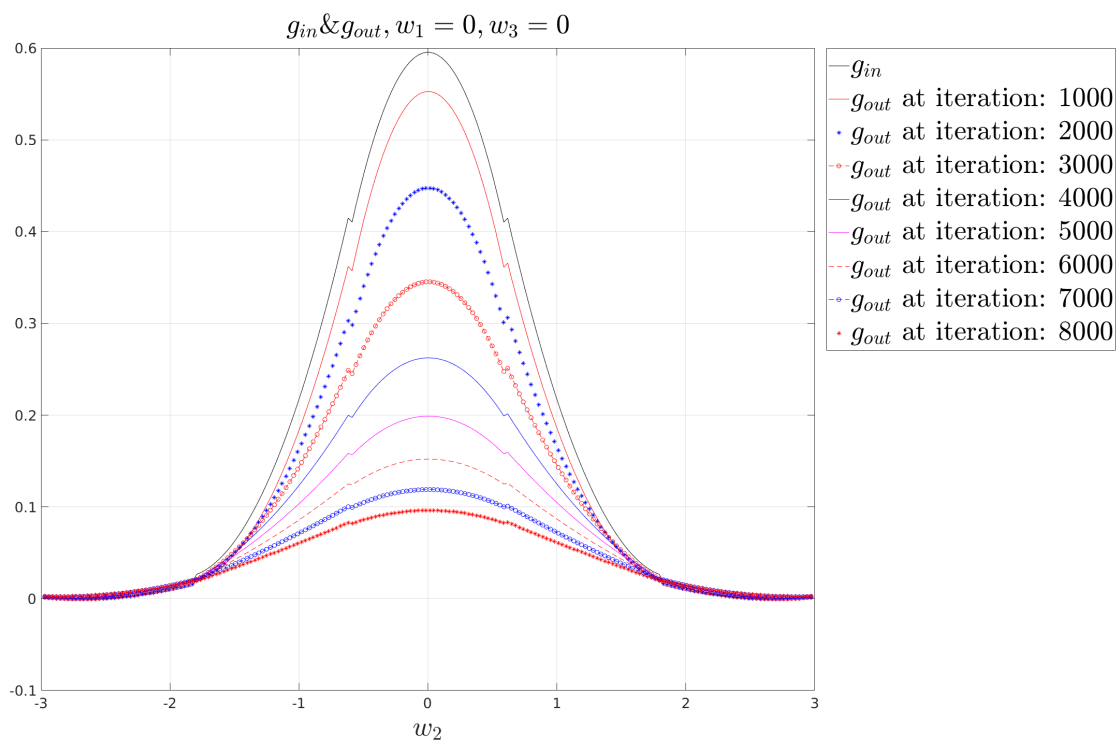


Figure 5.8: Experiment 1 with 125 Elements: Evolution of g with $w_1 = w_3 = 0$

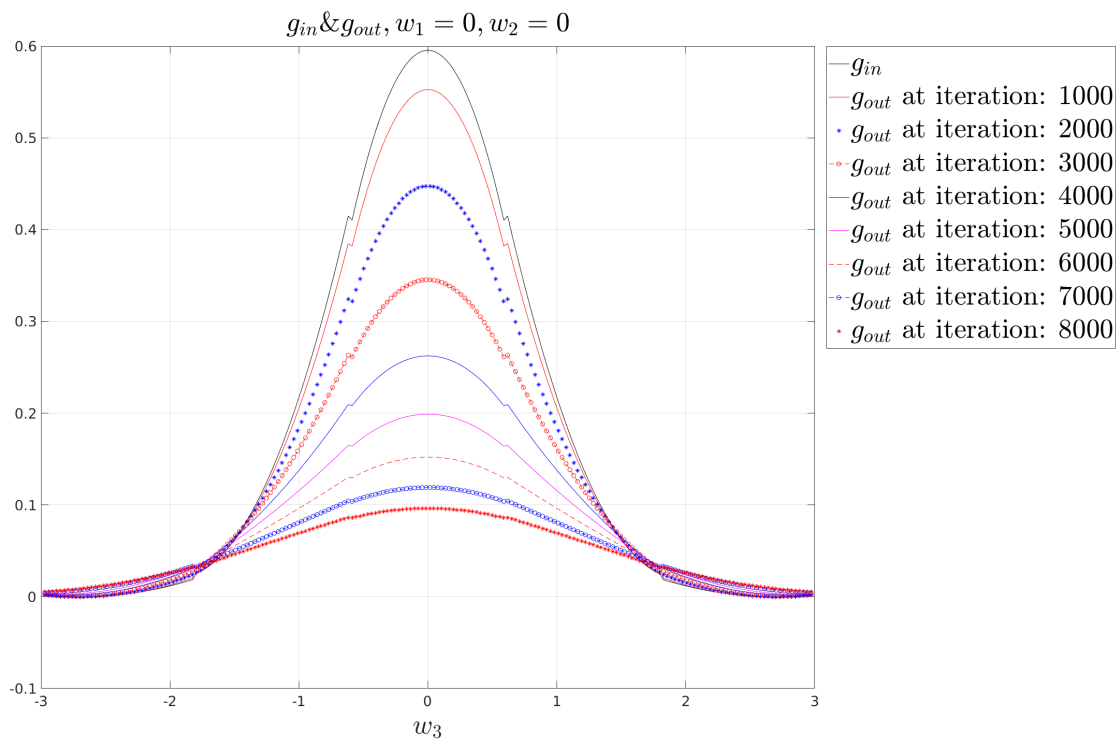


Figure 5.9: Experiment 1 with 125 Elements: Evolution of g with $w_1 = w_2 = 0$

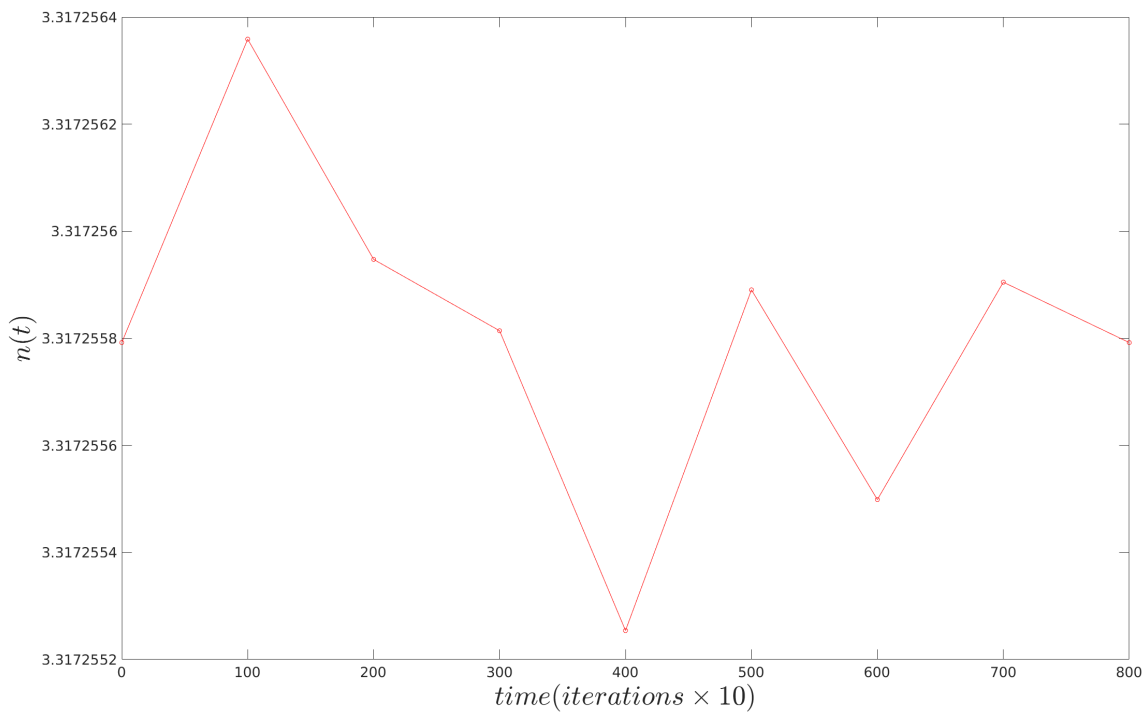


Figure 5.10: Experiment 1 with 125 Elements: Number Density

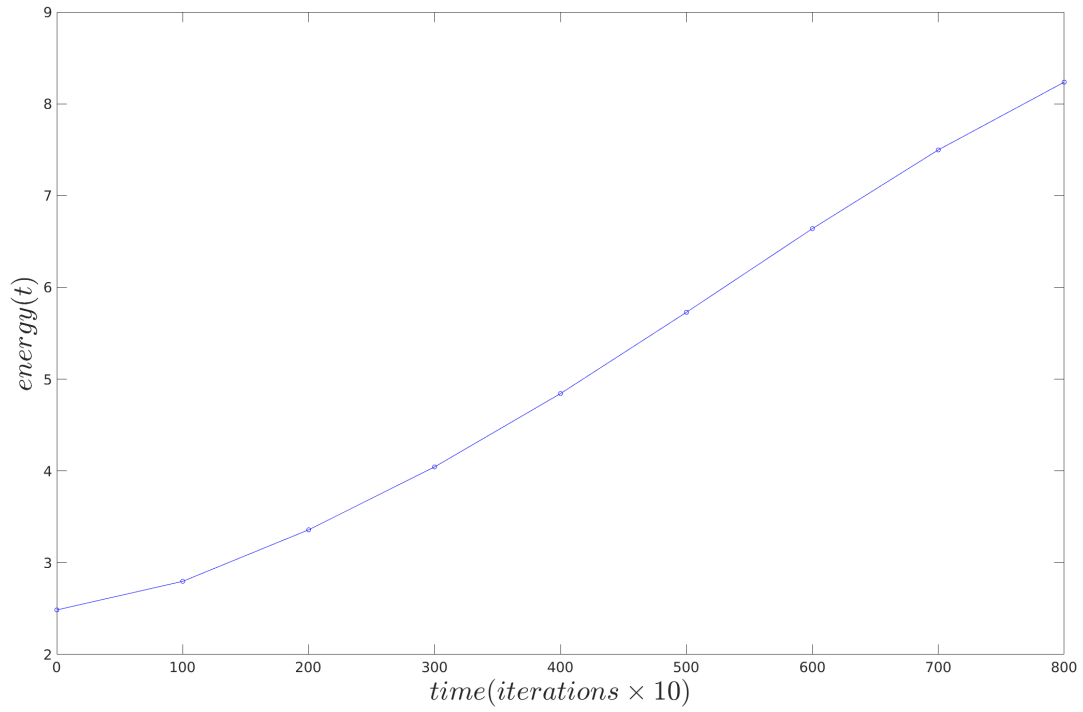


Figure 5.11: Experiment 1 with 125 Elements: Energy

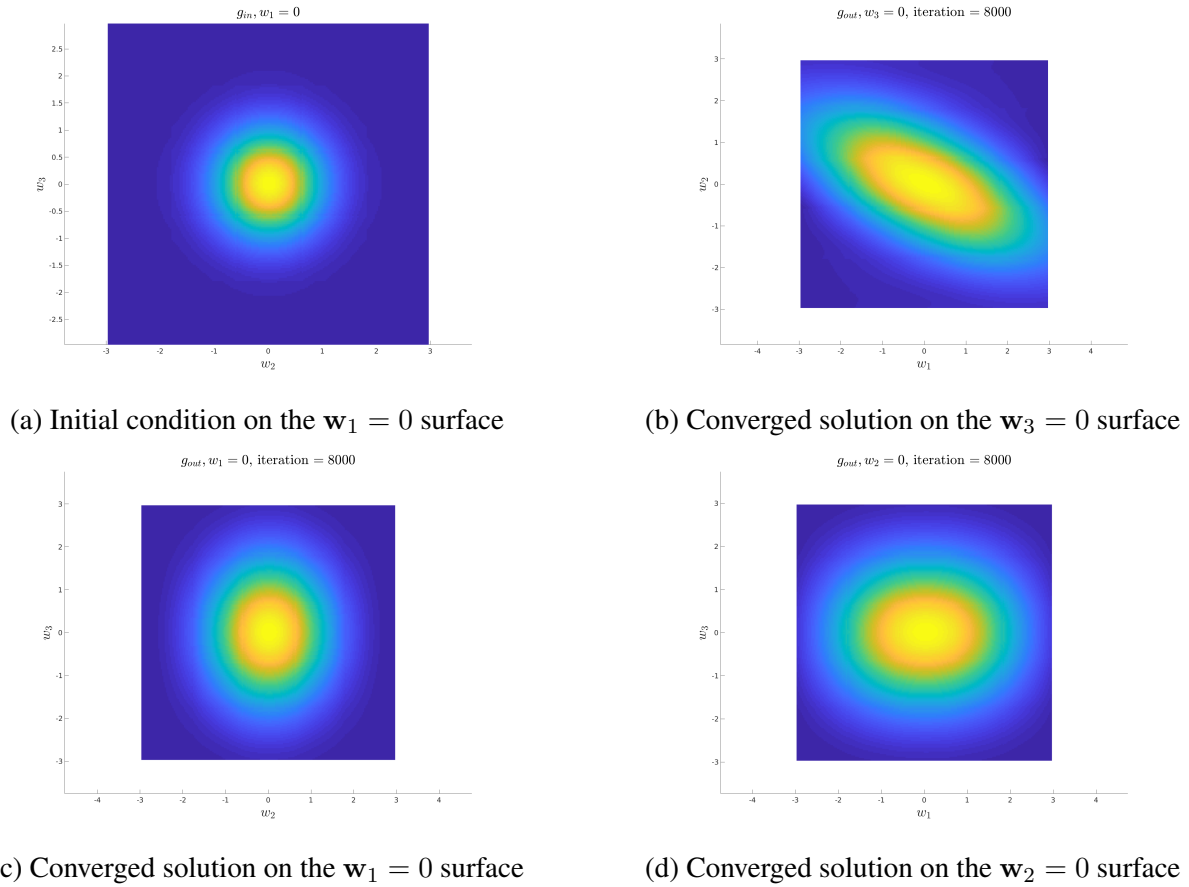
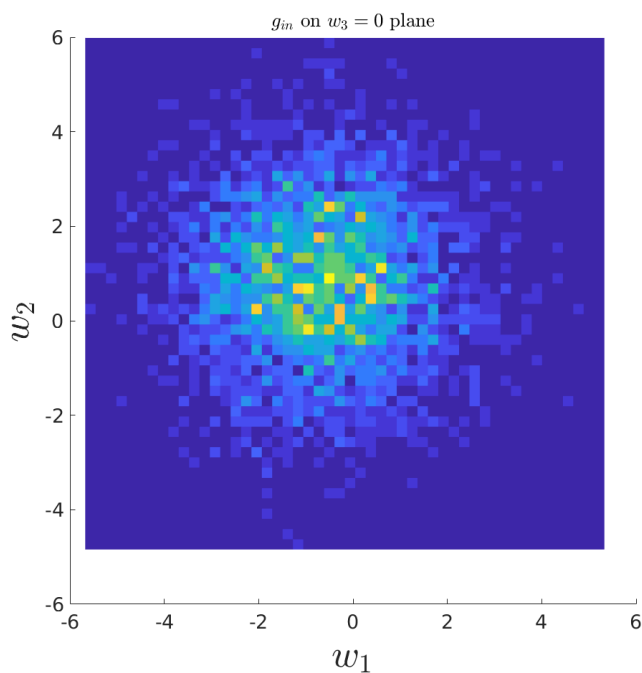
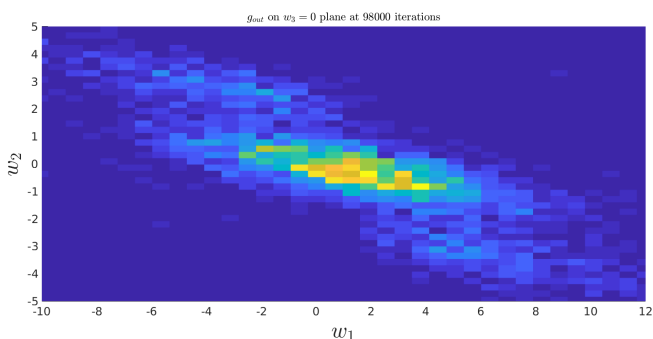


Figure 5.12: Experiment 1 with 125 Elements: Input and output on different surfaces

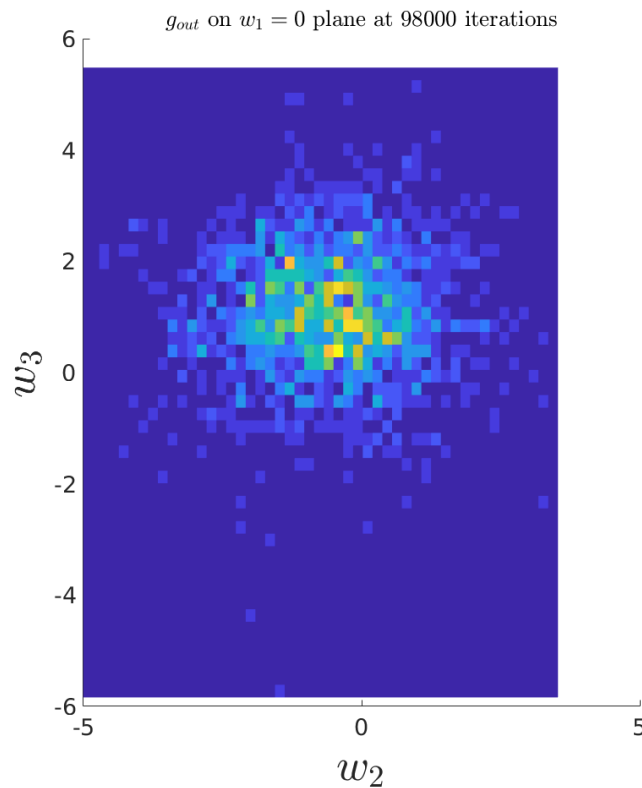
Here we observe that the energy of the system increases due to the energy added in the form of shear strain as expected. We see that the number of particles with low velocities decrease and that with high velocities increase, resulting in increasing the total energy of the gas as shown in Figure 5.1 and Figure 5.7. The number density and energy of the gas computed using the expressions given in section §2.5 with (2.5.0.4) and (2.5.0.7). It could also be observed that because of the shear in $\mathbf{I}_1 \otimes \mathbf{I}_2$ direction we observe a diagonal spreading of the distribution function g implying the particles gain velocity in the $w_1 - w_2$ and $w_2 - w_1$ directions. This behavior is in agreement with the molecular dynamics simulation run with LAMMPS as shown in Figure 5.13. This LAMMPS simulation is done with 10,000 particles with the same unitless shear rate as the simulation with Boltzmann equation *i.e.* $\dot{\gamma} = 0.8$ for 98,000 iterations. In Figure 5.6, Figure 5.12, and Figure 5.13 the initial conditions are symmetric with respect to all axes (w_1, w_2, w_3) and hence it has been illustrated on the $w_1 = 0$ plane only.



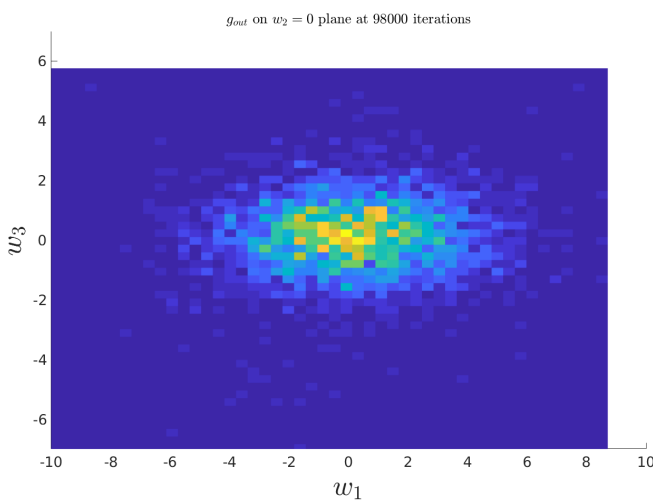
(a) Initial condition on the $w_3 = 0$ surface



(b) Converged solution on the $w_3 = 0$ surface



(c) Converged solution on the $w_1 = 0$ surface



(d) Converged solution on the $w_2 = 0$ surface

Figure 5.13: Experiment 1 in LAMMPS: Input and output on different surfaces

Since LAMMPS do not have any hard sphere potential in-built in their software, we have used the

closest approximation by using a Lennard-Jones potential with a cut-off ranging only up to a distance of no repulsion and hence no attractive forces were taken into consideration for the simulations.

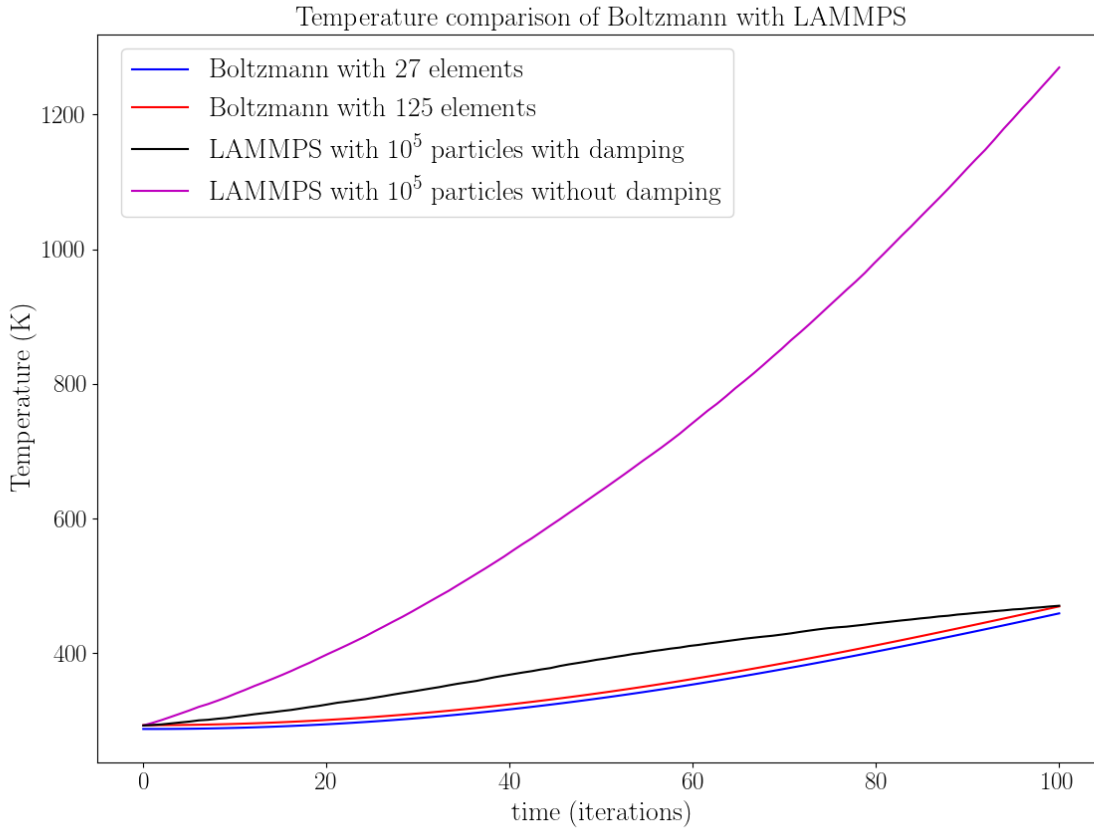


Figure 5.14: Temperature comparison of Boltzmann with molecular dynamics

The LAMMPS simulation was done with 10,000 and 100,000 particles with a viscosity damping of 0.0011 dimensionless LAMMPS Lennard-Jones units. The energies of the two methods of simulation matches only under the condition of imposition of a viscous damping, which is possibly because of the leaking of energy due to domain-truncation. The energy, momentum and number density in the verification experiments were constrained with the use of Lagrange polynomial which wasn't possible in the non-equilibrium simulation where we supply energy into the system in the form of shear force. It could be observed that the 125 element solution is in a much better agreement with the molecular dynamics results than the 27 element solution.

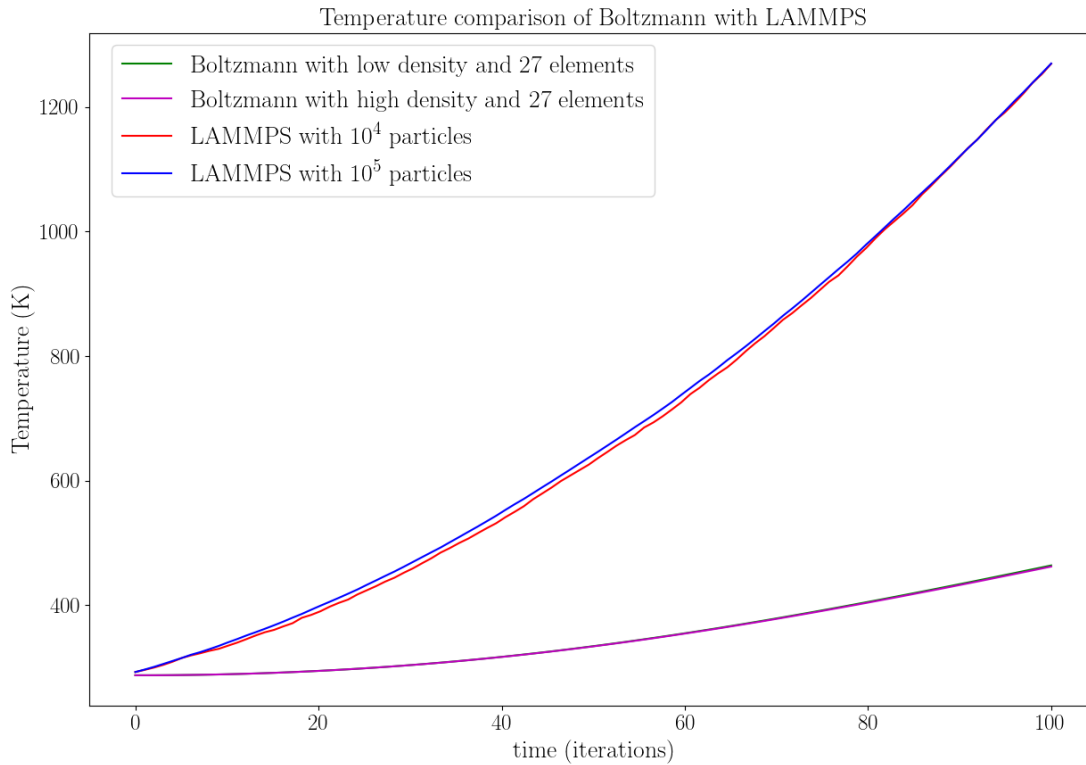


Figure 5.15: Temperature comparison of Boltzmann with molecular dynamics with 2 different densities

It could also be observed that the energy curves are independent of the number density of the simulated gas as shown in Figure 5.15.

The *mean free path* of gases is computed by the expression in (2.6.0.1)

$$\lambda = \frac{1}{\sqrt{2}\pi\rho_0 d_0^2}$$

which has been used to decide on the parameters in both the simulation of Boltzmann equation and LAMMPS. The parameters used to compare the results were for a low-density Argon gas with 10,000 and 100,000 particles in a box of size $2000\sigma \times 2000\sigma \times 2000\sigma$ where σ is the Lennard-Jones parameter for Ar.

We have also run the simulation for different box sizes in LAMMPS keeping the density same and we observe that the solution is closer to the solution with Boltzmann equation with a smaller box size for the same shear strain rate Figure 5.16.

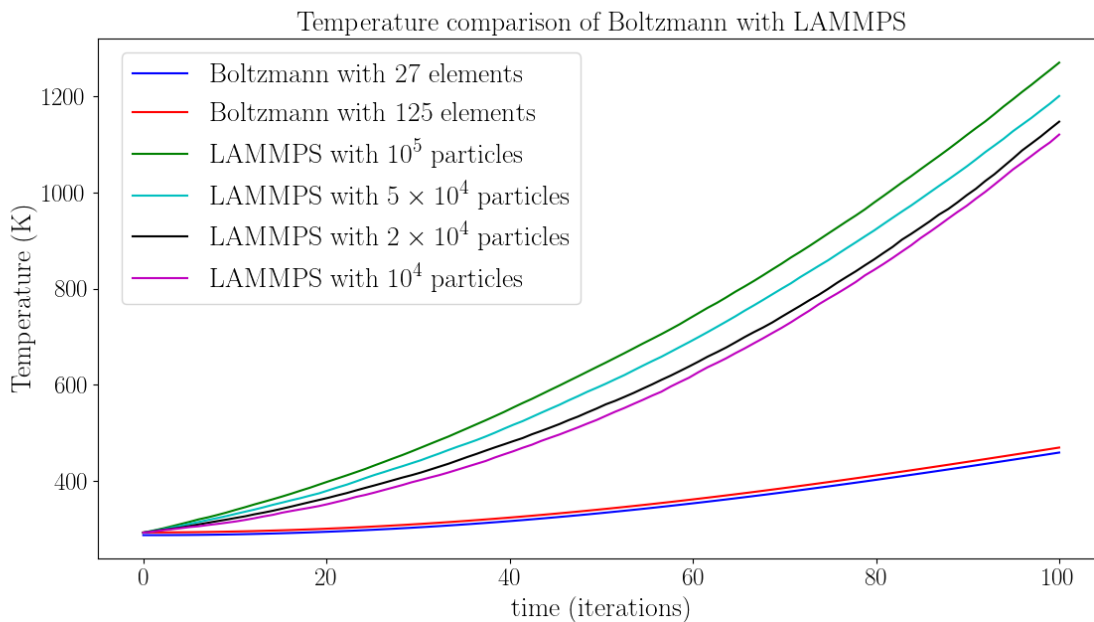


Figure 5.16: Temperature comparison of Boltzmann with molecular dynamics with different box sizes

5.3 Pressure Shear

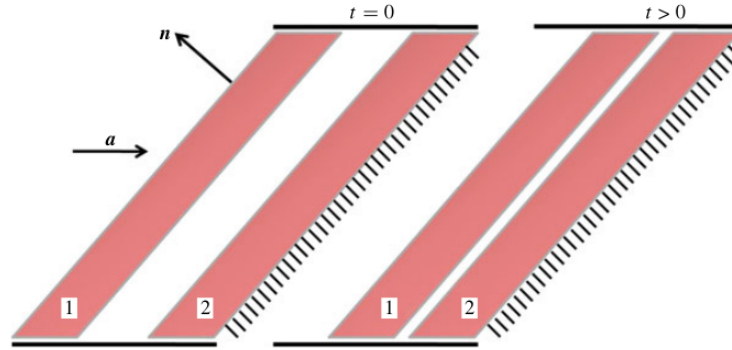


Figure 5.17: Schematic pressure-shear viscometer: vectors \mathbf{a} and \mathbf{n} as in the text. The leading edge of plate 1 moves at constant velocity in the direction \mathbf{a} towards plate 2, which is stationary. Both plates are in general oblique to the velocity as shown. (from Dayal & James [15])

This experiment could be thought of an unsteady, compressible flow represented by universal flow with $\mathbf{A} = \mathbf{a} \otimes \mathbf{n}$ with $\mathbf{a} \cdot \mathbf{n} \neq 0$. Hence $(\mathbf{I} + t\mathbf{A})^{-1} = \mathbf{I} - \frac{t(\mathbf{a} \cdot \mathbf{n})}{1+t(\mathbf{a} \cdot \mathbf{n})} \mathbf{a} \otimes \mathbf{n}$ and the velocity field as:

$$\mathbf{v}(\mathbf{x}, t) = \frac{1}{1 + t(\mathbf{a} \cdot \mathbf{n})} (\mathbf{n} \cdot \mathbf{x}) \mathbf{a}, \quad t > 0 \quad (5.3.0.1)$$

This simulation physically represents homogeneous flow between two plates with normals \mathbf{n} moving towards each other ($\mathbf{a} \cdot \mathbf{n} < 0$) with the fluid moving in the direction of the motion of plates with a velocity \mathbf{a} . The simulation could run up to a time somewhat lesser than when \mathbf{v} becomes singular, *i.e.* $t = -\frac{1}{\mathbf{a} \cdot \mathbf{n}}$ which physically represents the striking the plates with each other. The parameters of \mathbf{A} that we have used to simulate this flow is:

$$\mathbf{A} = \begin{pmatrix} -0.25 & 0 & 1.4 \\ 0 & 0 & 0 \\ 0 & 0 & 0 \end{pmatrix} \quad (5.3.0.2)$$

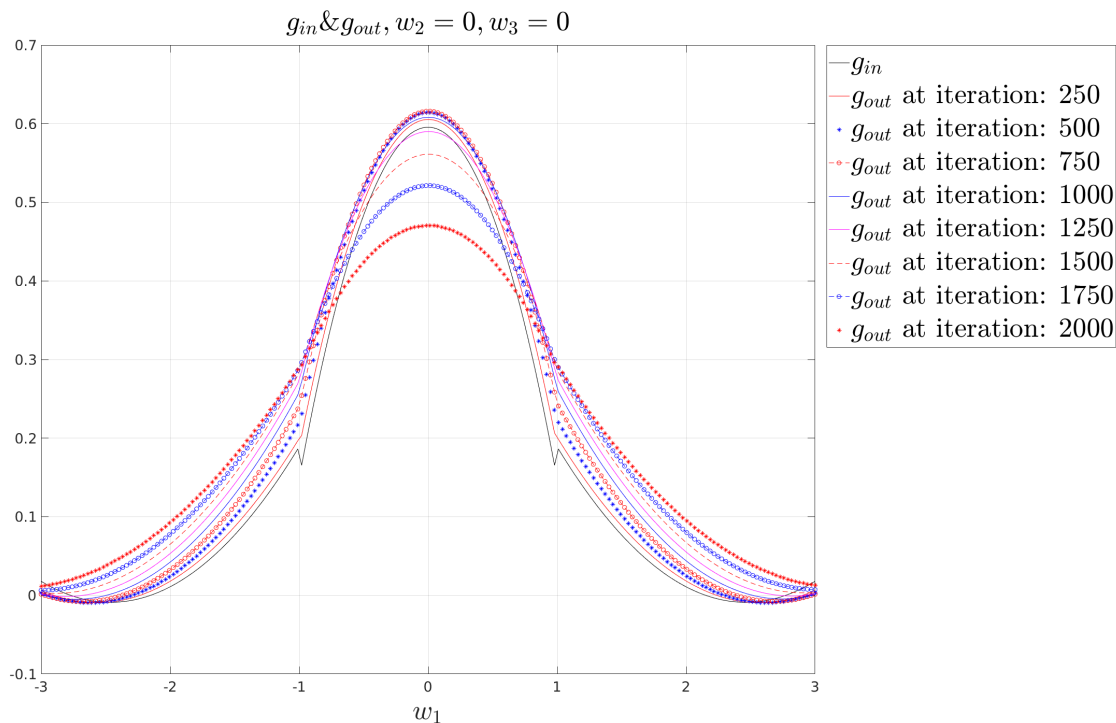


Figure 5.18: Experiment 4 with 27 Elements: Evolution of g with $w_2 = w_3 = 0$

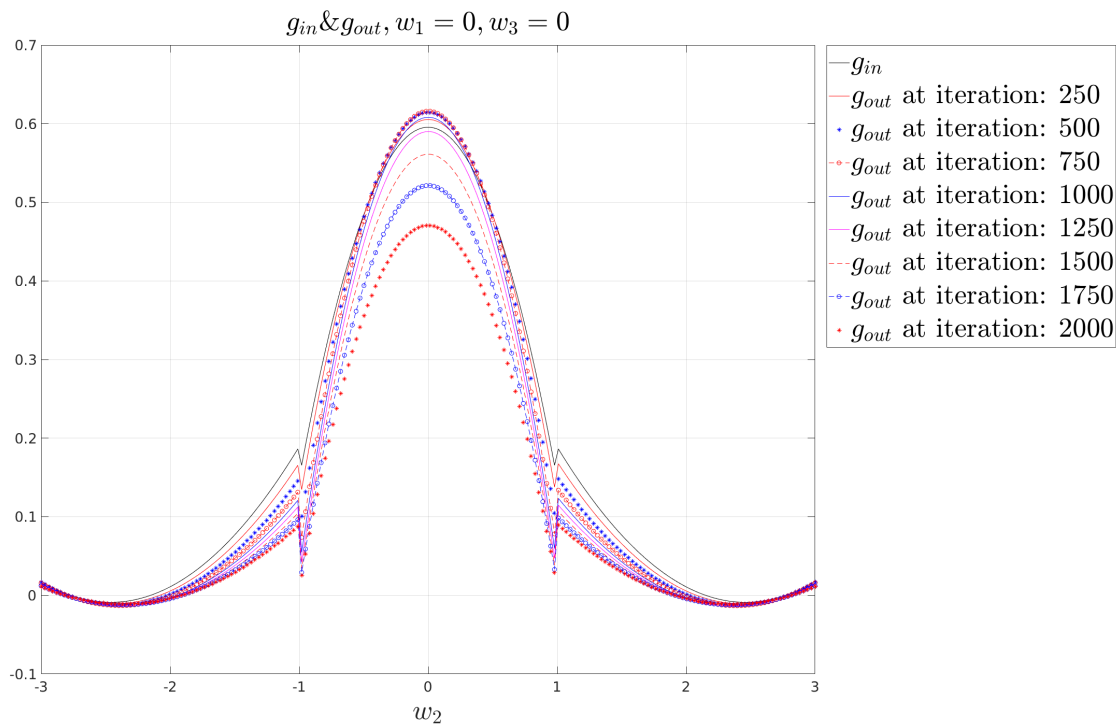


Figure 5.19: Experiment 4 with 27 Elements: Evolution of g with $w_1 = w_3 = 0$

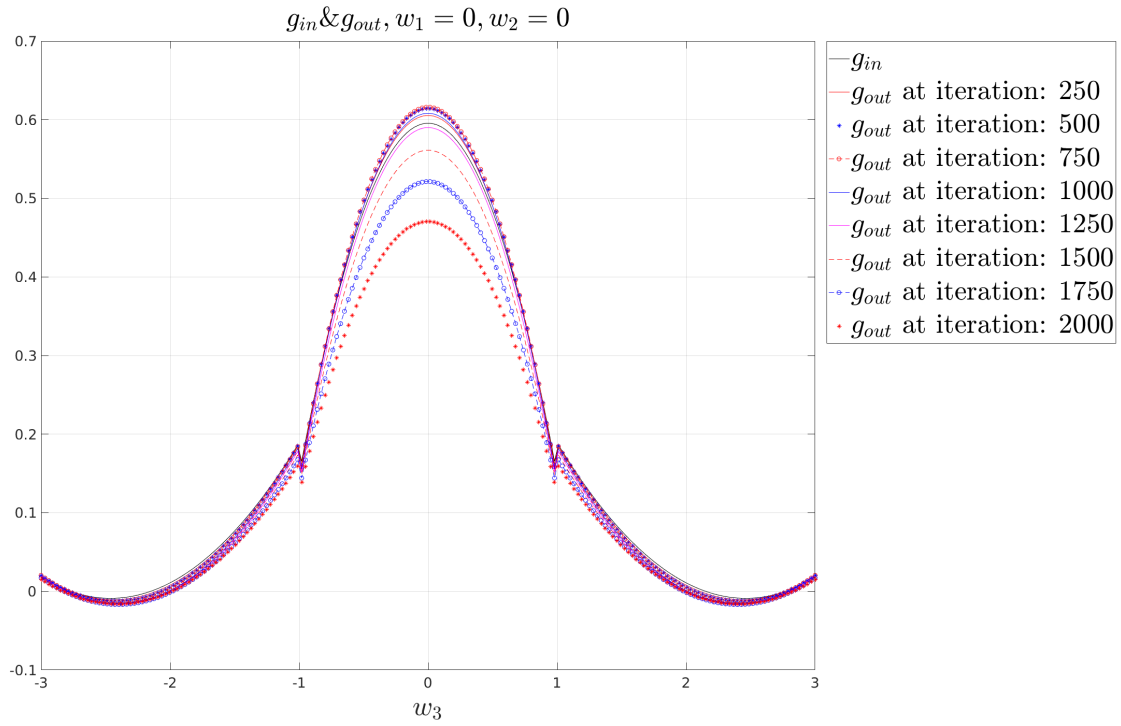


Figure 5.20: Experiment 4 with 27 Elements: Evolution of g with $w_1 = w_2 = 0$

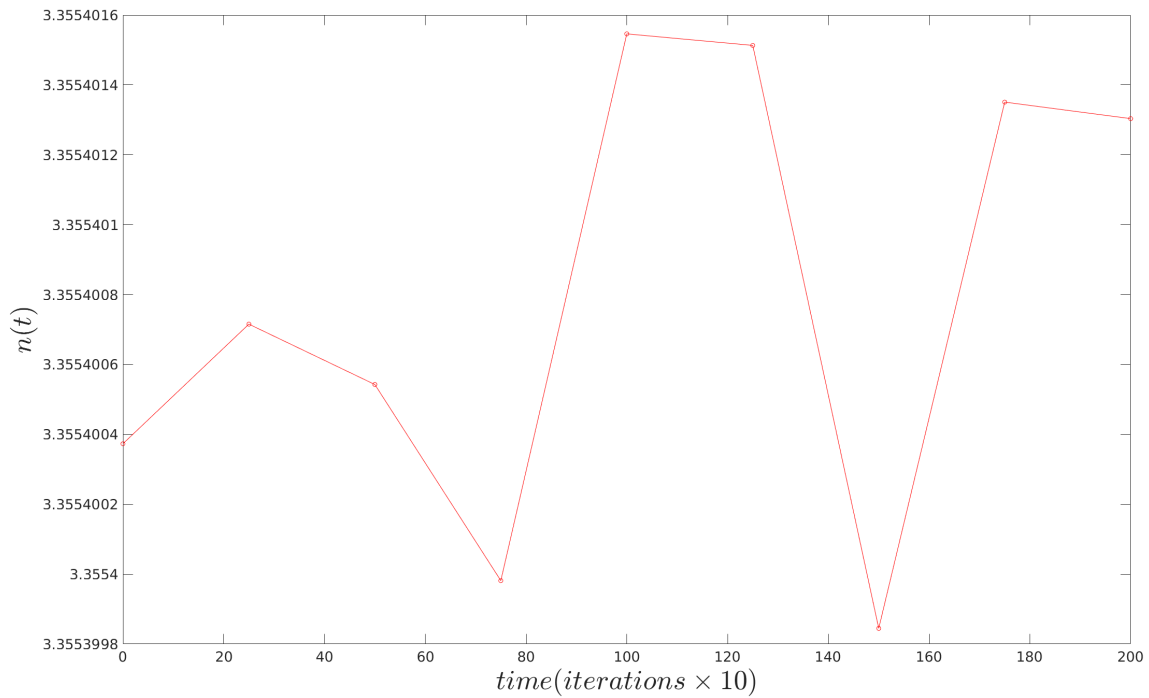


Figure 5.21: Experiment 4 with 27 Elements: Number Density

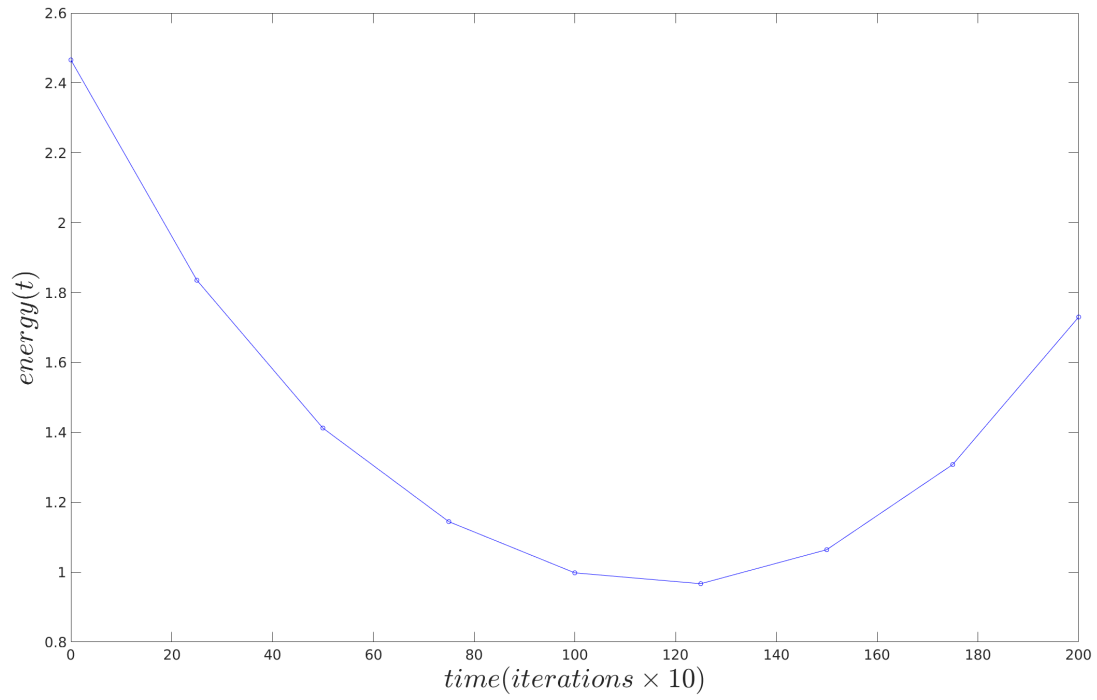
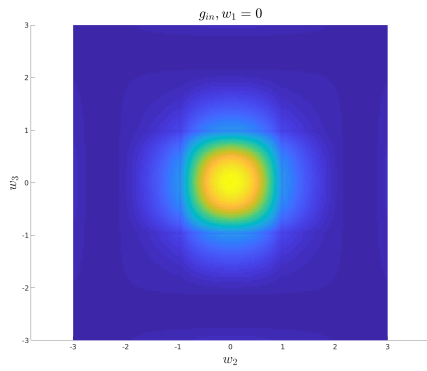
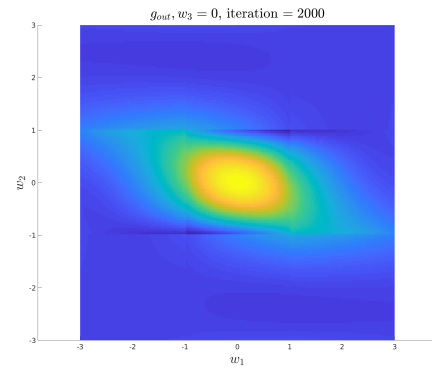


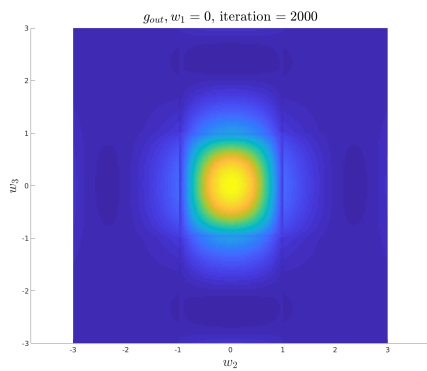
Figure 5.22: Experiment 4 with 27 Elements: Energy



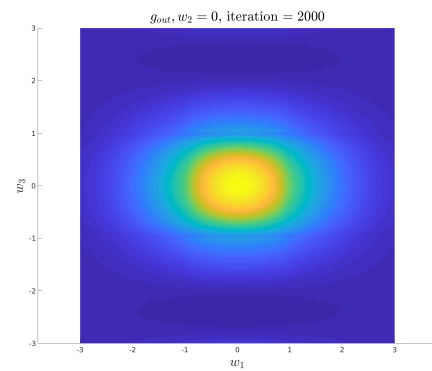
(a) Initial condition on the $w_1 = 0$ surface



(b) Converged solution on the $w_3 = 0$ surface



(c) Converged solution on the $w_1 = 0$ surface



(d) Converged solution on the $w_2 = 0$ surface

Figure 5.23: Experiment 4 with 27 Elements: Input and output on different surfaces

This experiment with 5 elements:

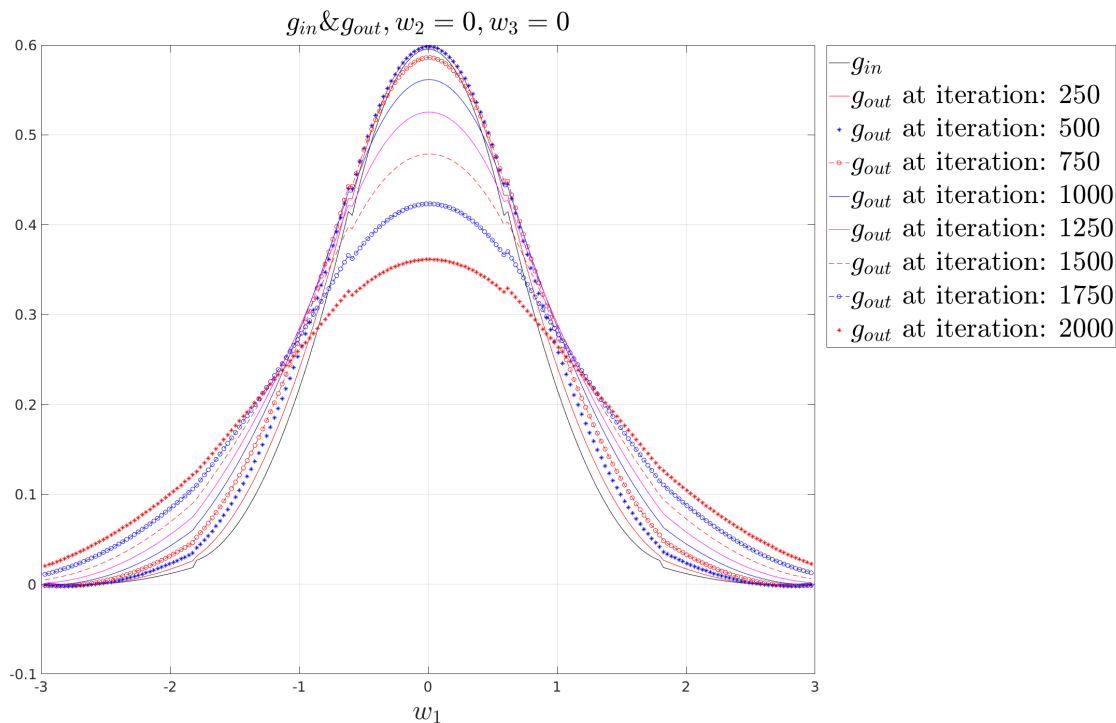


Figure 5.24: Experiment 4 with 125 Elements: Evolution of g with $w_2 = w_3 = 0$

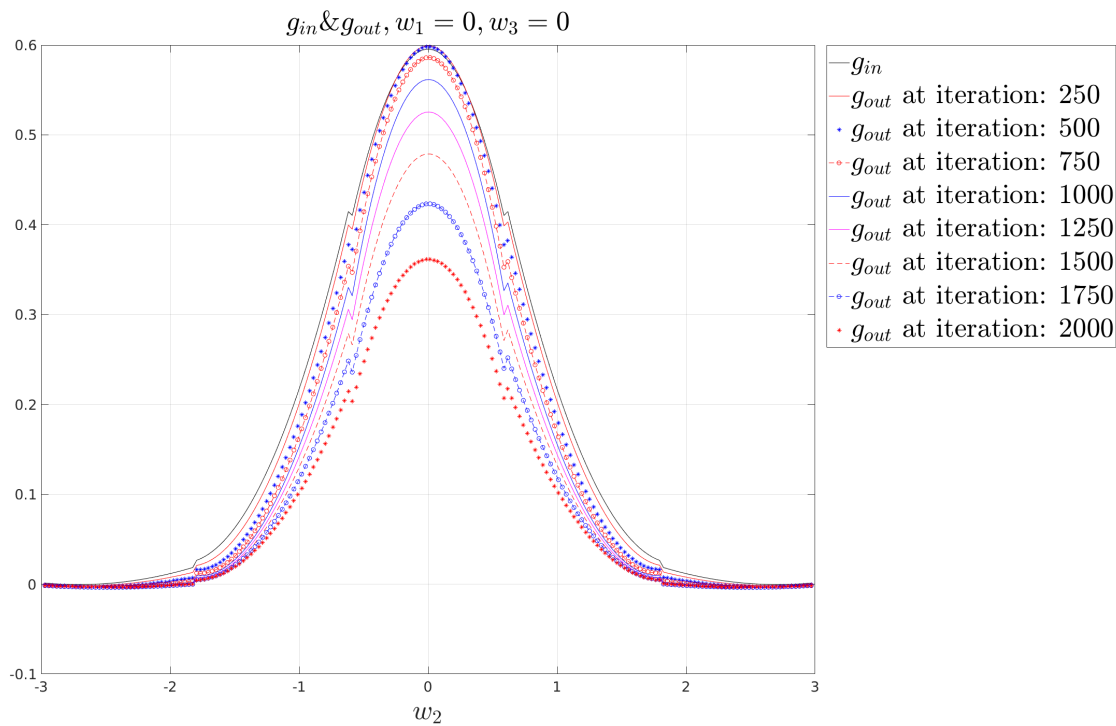


Figure 5.25: Experiment 4 with 125 Elements: Evolution of g with $w_1 = w_3 = 0$

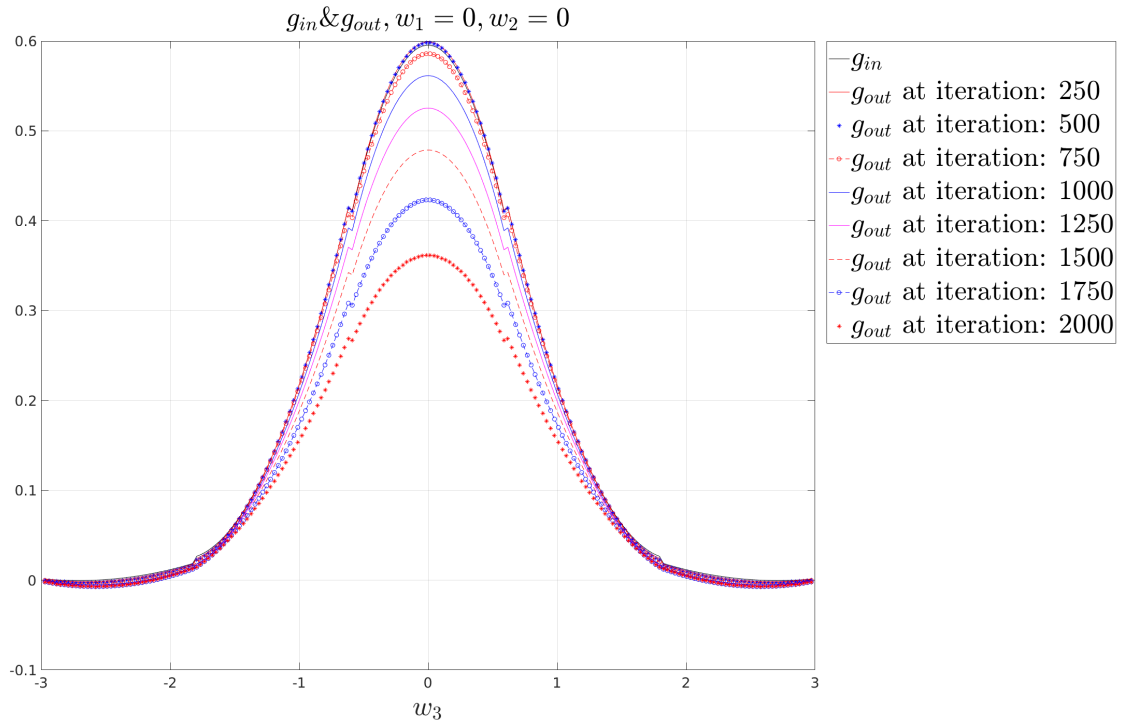


Figure 5.26: Experiment 4 with 125 Elements: Evolution of g with $w_1 = w_2 = 0$

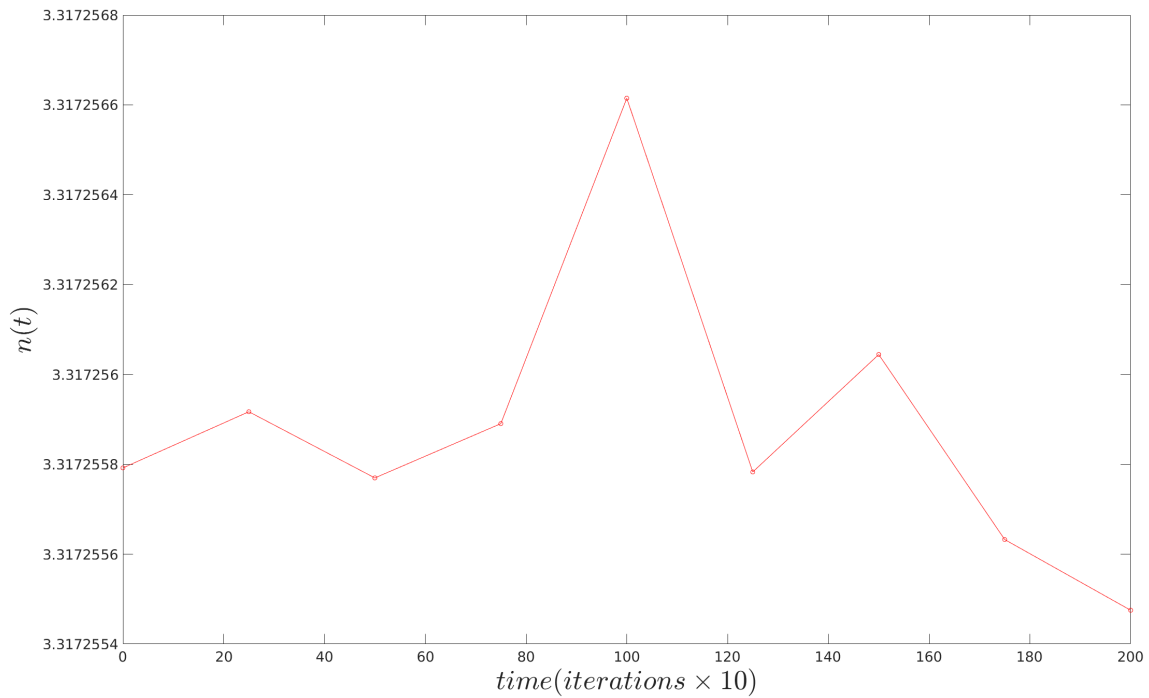


Figure 5.27: Experiment 4 with 125 Elements: Number Density

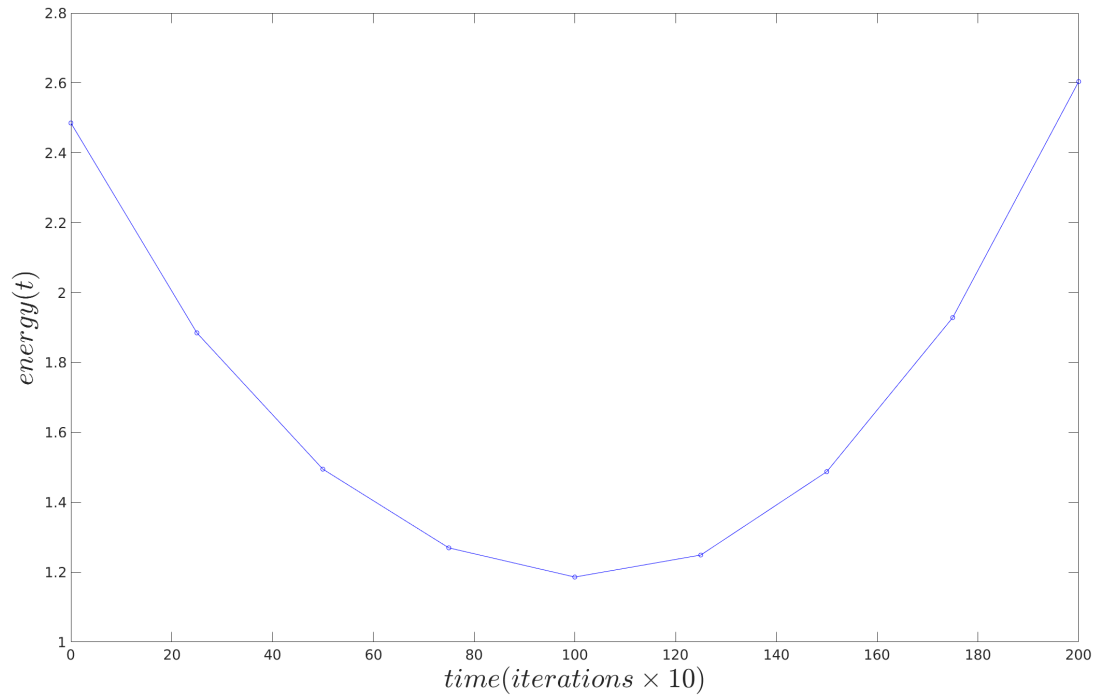
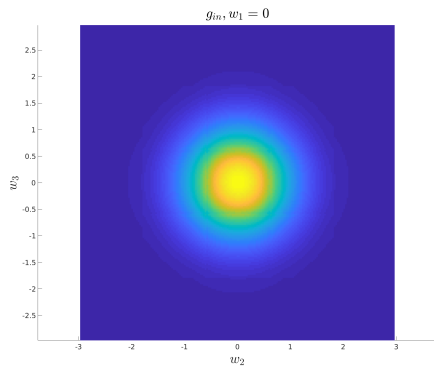
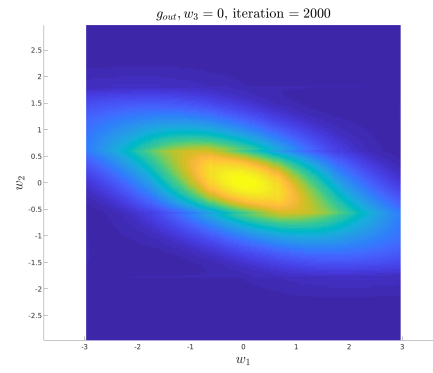


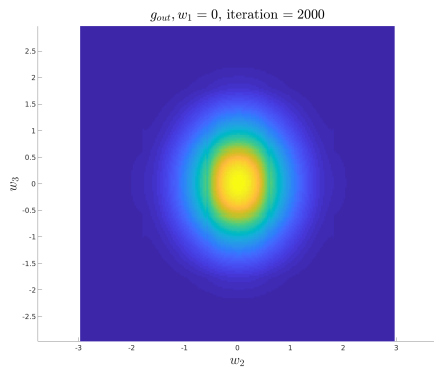
Figure 5.28: Experiment 4 with 125 Elements: Energy



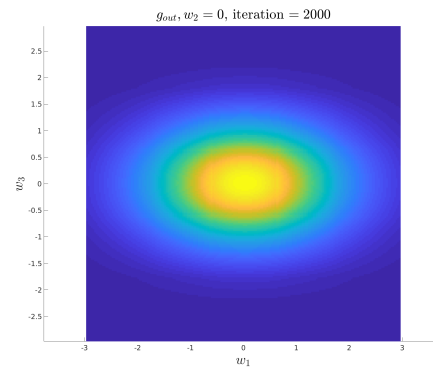
(a) Initial condition on the $w_1 = 0$ surface



(b) Converged solution on the $w_3 = 0$ surface



(c) Converged solution on the $w_1 = 0$ surface



(d) Converged solution on the $w_2 = 0$ surface

Figure 5.29: Experiment 4 with 125 Elements: Input and output on different surfaces

5.4 Simple bi-directional Shear

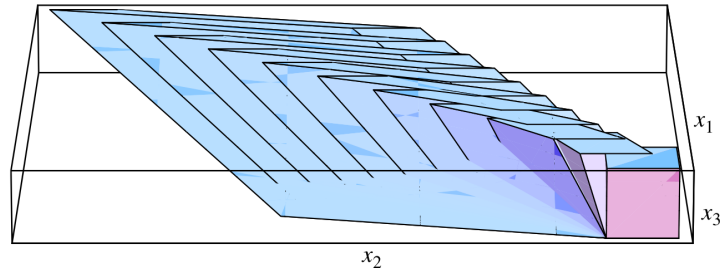


Figure 5.30: Universal flow of the unit cube having outer normals $\mathbf{l}_1, \mathbf{l}_2, \mathbf{l}_3$. The values of the parameters are $\alpha = 1.4, v_1 = 0.9, v_3 = 0.7$. The figure shows the same set of material particles at successive instants of time. Time between pictures is 0.5 in consistent units. (from Dayal & James[15])

Dayal & James in [15] refers to (2.4.0.4) as the description for *universal flows*. They show that these flows are the exact solutions of the equations of motion of every fluid with no external body force. In addition to the explanation in section §2.4, they show that universal flows could be found in all flows. For example, incompressible flows could be described in the following way. Incompressibility immediately imposes the condition, $\det(\mathbf{I} + t\mathbf{A}) = 1, \forall t > 0$. The characteristic equation in t reveals the condition,

$$\det \mathbf{A} = \text{tr } \mathbf{A} = \text{tr } \mathbf{A}^2 = 0 \quad (5.4.0.1)$$

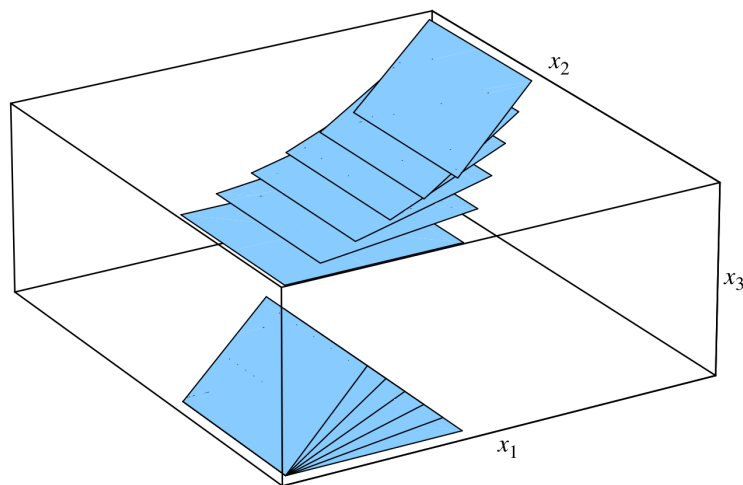


Figure 5.31: Motion of the two planes with normal \mathbf{l}_3 with parameters chosen as in Figure 5.30. Time between pictures is 0.2 in consistent units. (from Dayal & James[15])

The necessary and sufficient conditions for (5.4.0.1) in a suitable orthonormal basis are,

$$\mathbf{A} = \begin{pmatrix} 0 & 0 & \alpha \\ v_1 & 0 & v_2 \\ 0 & 0 & 0 \end{pmatrix} \quad (5.4.0.2)$$

Considering $\mathbf{A} = \alpha \mathbf{l}_1 \otimes \mathbf{l}_3 + v_1 \mathbf{l}_2 \otimes \mathbf{l}_1 + v_3 \mathbf{l}_2 \otimes \mathbf{l}_3$, where $\mathbf{l}_1, \mathbf{l}_2$ and \mathbf{l}_3 form an orthonormal basis it directly implies that the Eulerian description of this motion is,

$$\mathbf{v}(\mathbf{x}, t) = \mathbf{A}\mathbf{x} - \alpha t v_1 v_3 \mathbf{l}_2 \quad (5.4.0.3)$$

In this experiment we run the simulation on an incompressible gas with shear in three directions as shown in Figure 5.30 with the same dimensionless values of shear rates *i.e.* $\alpha = 1.4, v_1 = 0.9, v_3 = 0.7$ and observe the evolution of the velocity distribution g . To describe the motion macroscopically, all material particles in planes with \mathbf{l}_3 remain in their planes. The initial square faces with normals $\pm \mathbf{l}_3$ of the cube considered become parallelograms with preserving areas.

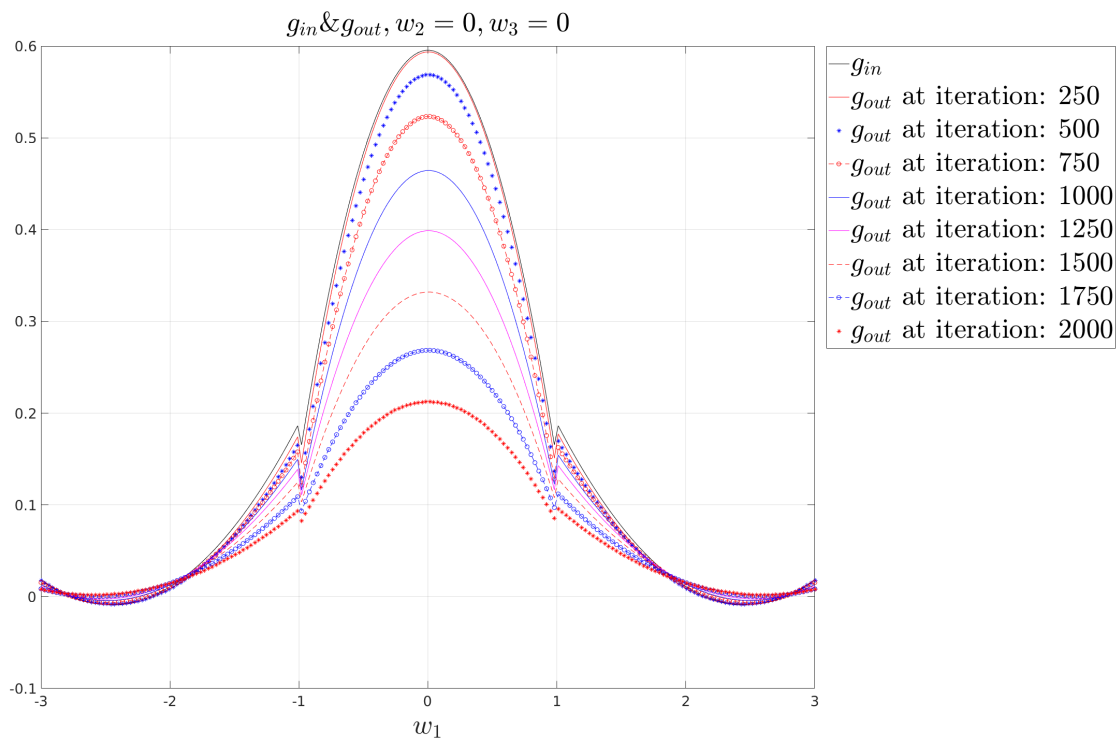


Figure 5.32: Experiment 2 with 27 Elements: Evolution of g with $w_2 = w_3 = 0$

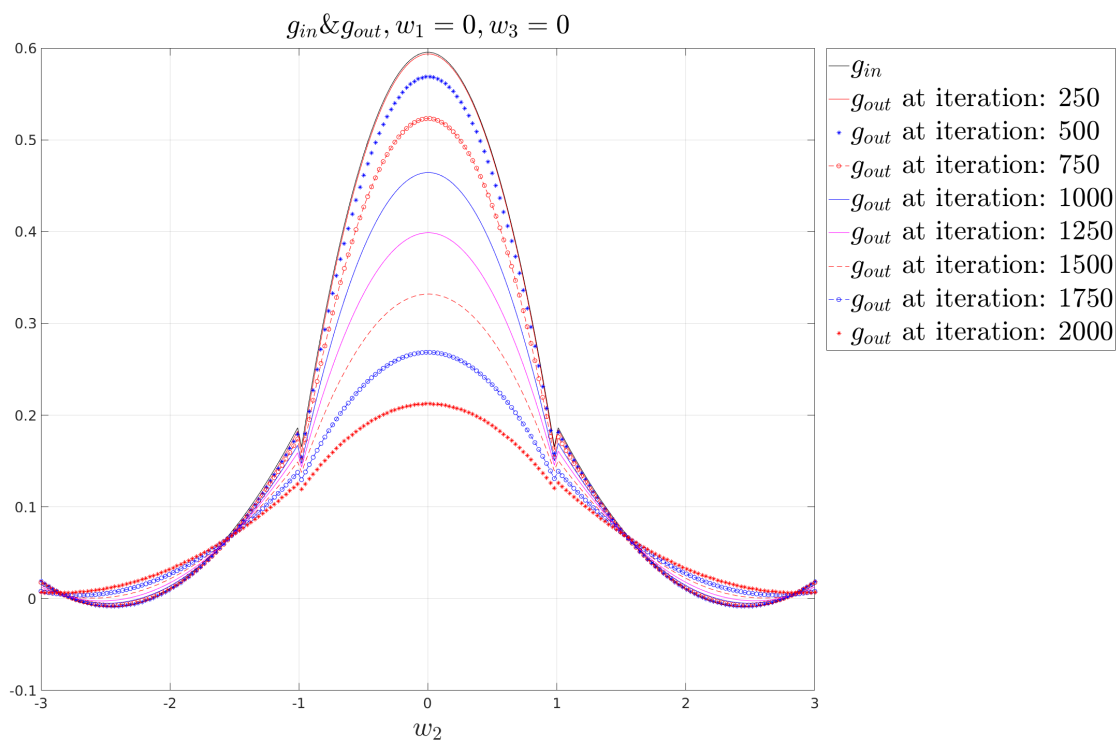


Figure 5.33: Experiment 2 with 27 Elements: Evolution of g with $w_1 = w_3 = 0$

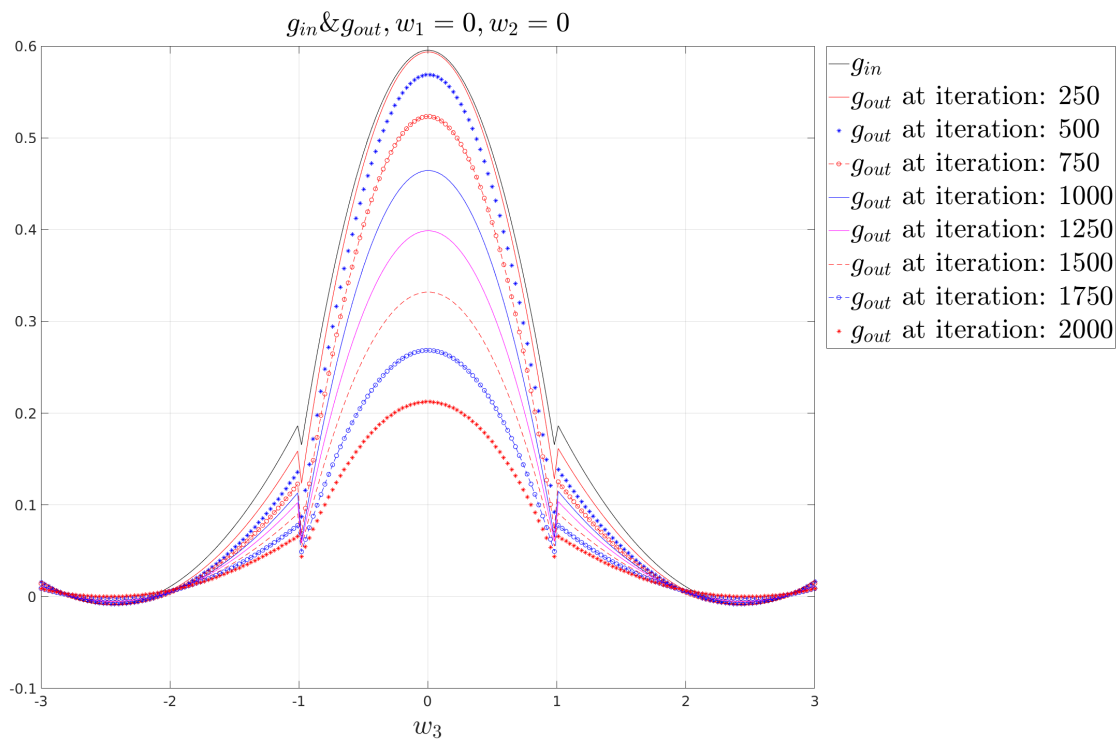


Figure 5.34: Experiment 2 with 27 Elements: Evolution of g with $w_1 = w_2 = 0$

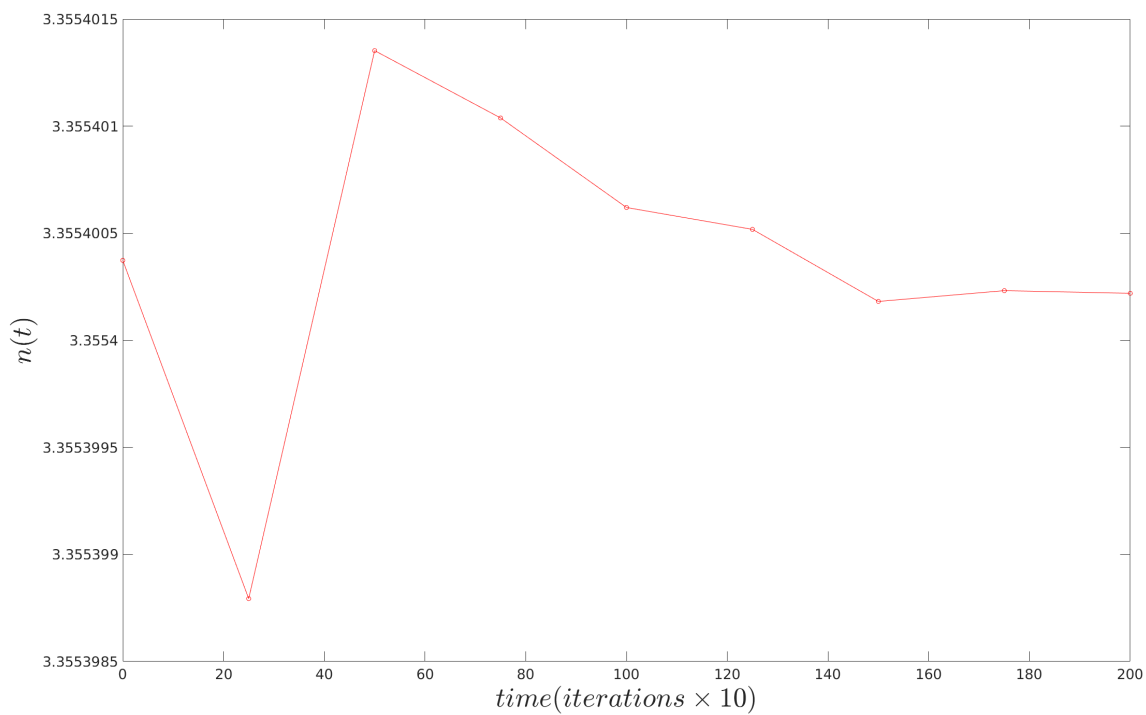


Figure 5.35: Experiment 2 with 27 Elements: Number Density

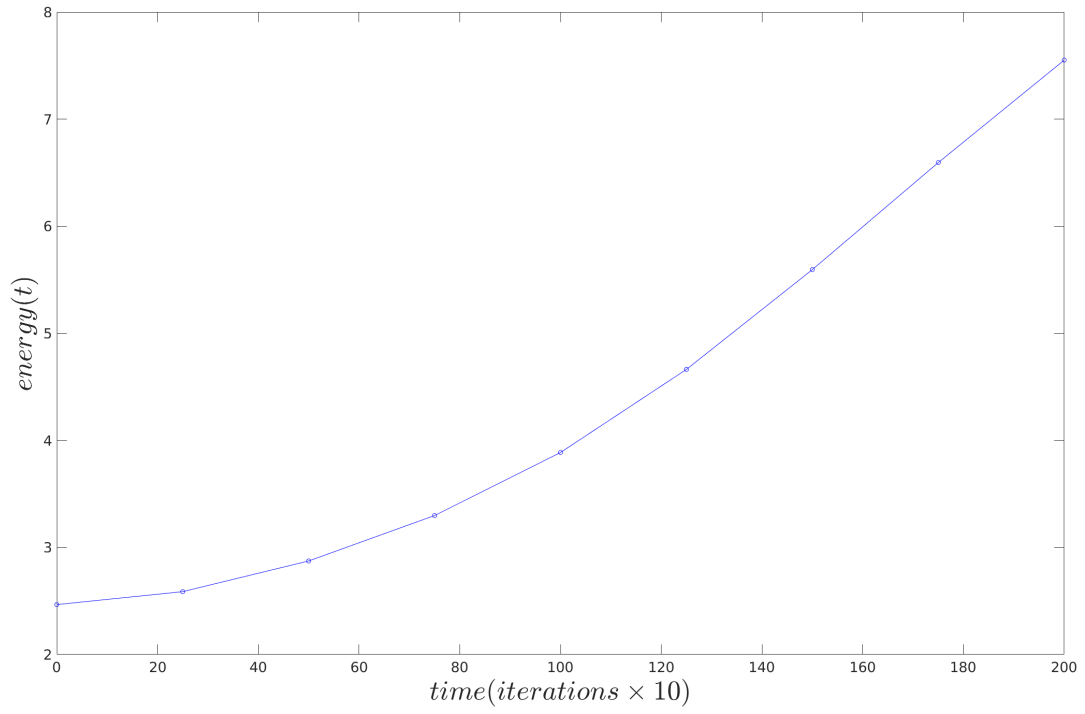
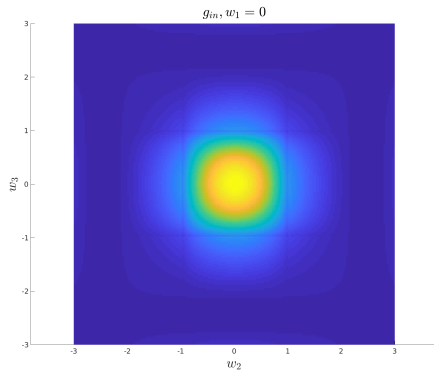
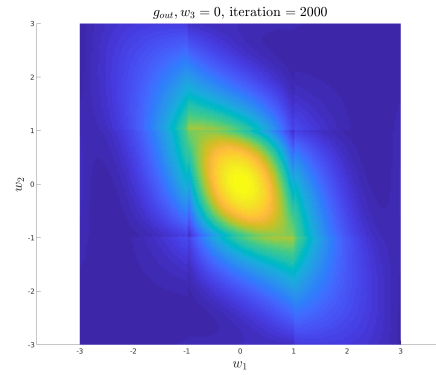


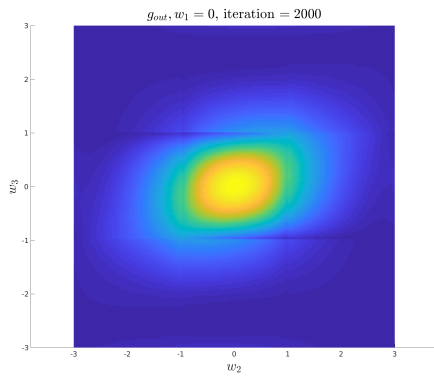
Figure 5.36: Experiment 2 with 27 Elements: Energy



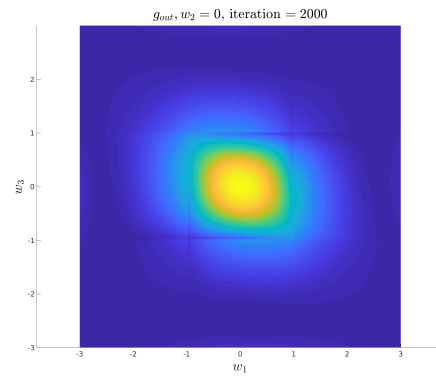
(a) Initial condition on the $w_1 = 0$ surface



(b) Converged solution on the $w_3 = 0$ surface



(c) Converged solution on the $w_1 = 0$ surface



(d) Converged solution on the $w_2 = 0$ surface

Figure 5.37: Experiment 2 with 27 Elements: Input and output on different surfaces

This experiment with 5 elements:

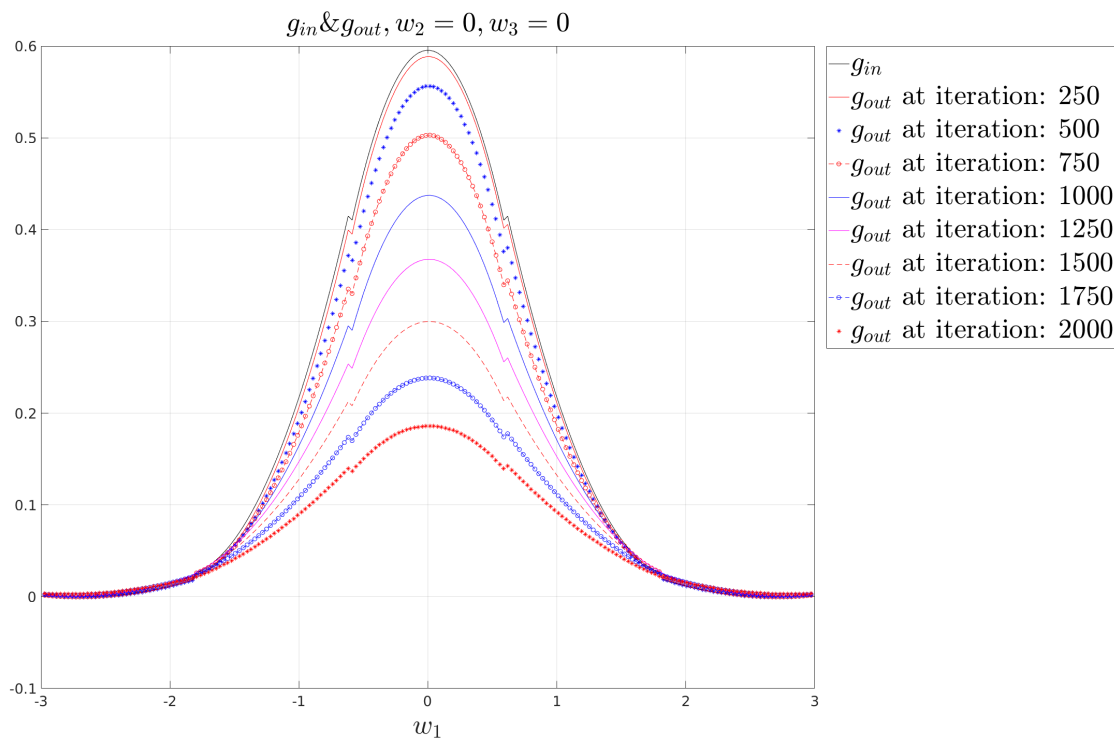


Figure 5.38: Experiment 2 with 125 Elements: Evolution of g with $w_2 = w_3 = 0$

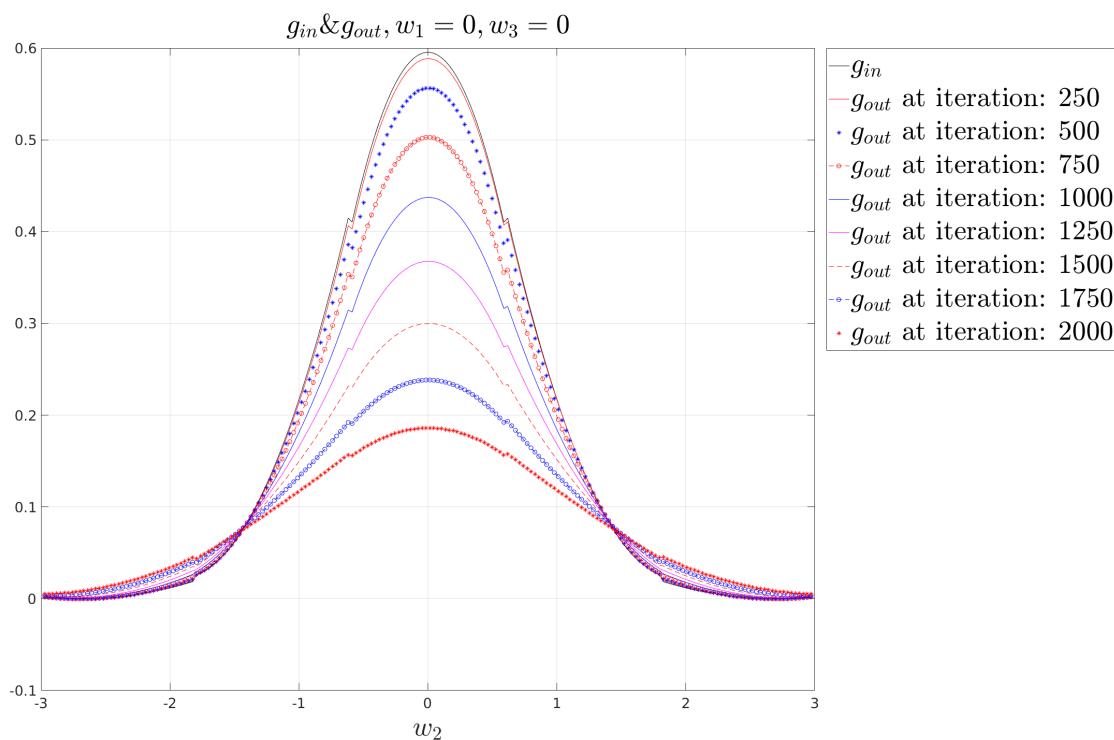


Figure 5.39: Experiment 2 with 125 Elements: Evolution of g with $w_1 = w_3 = 0$

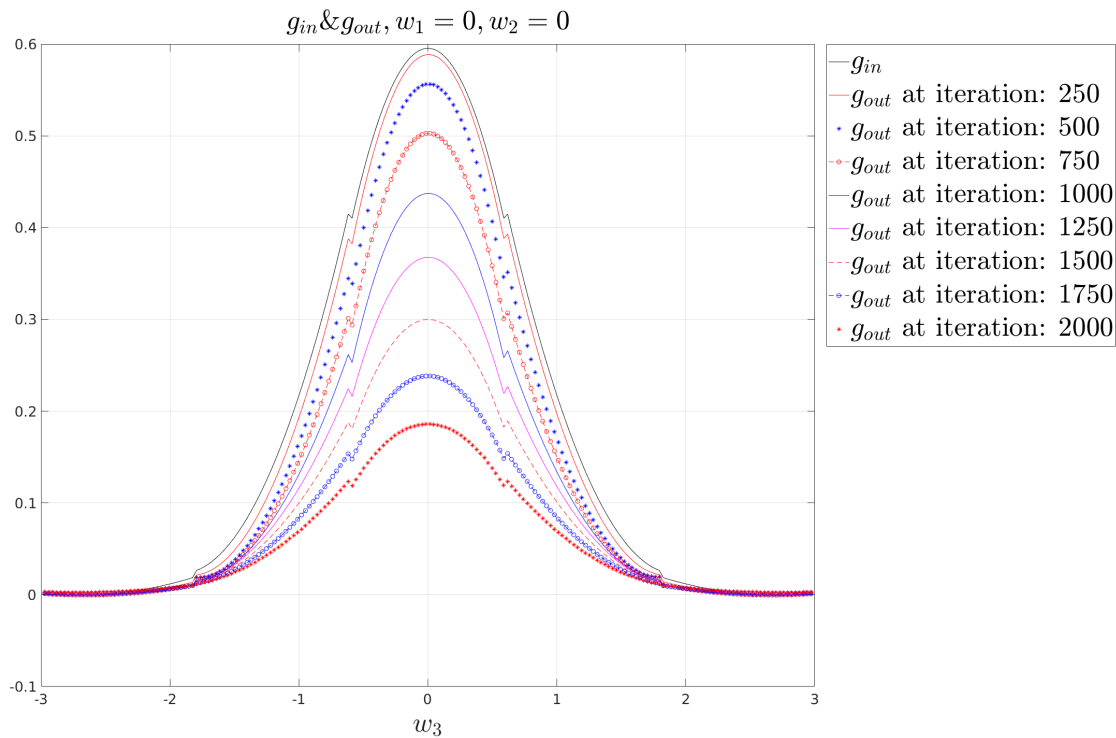


Figure 5.40: Experiment 2 with 125 Elements: Evolution of g with $w_1 = w_2 = 0$

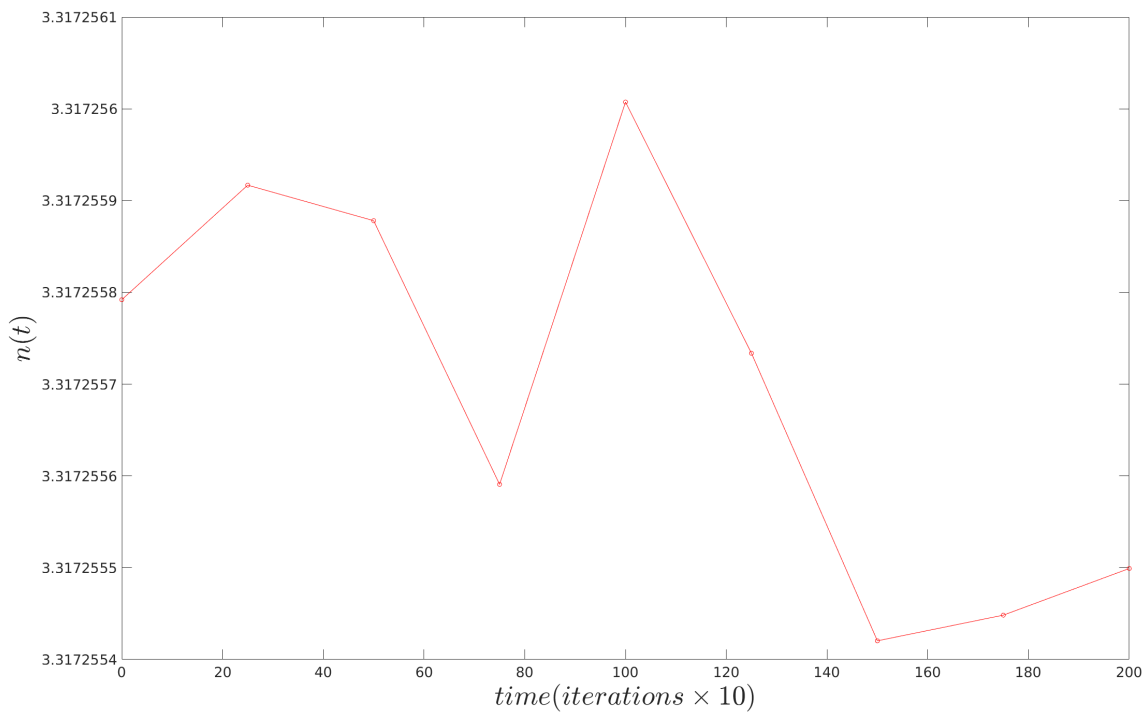


Figure 5.41: Experiment 2 with 125 Elements: Number Density

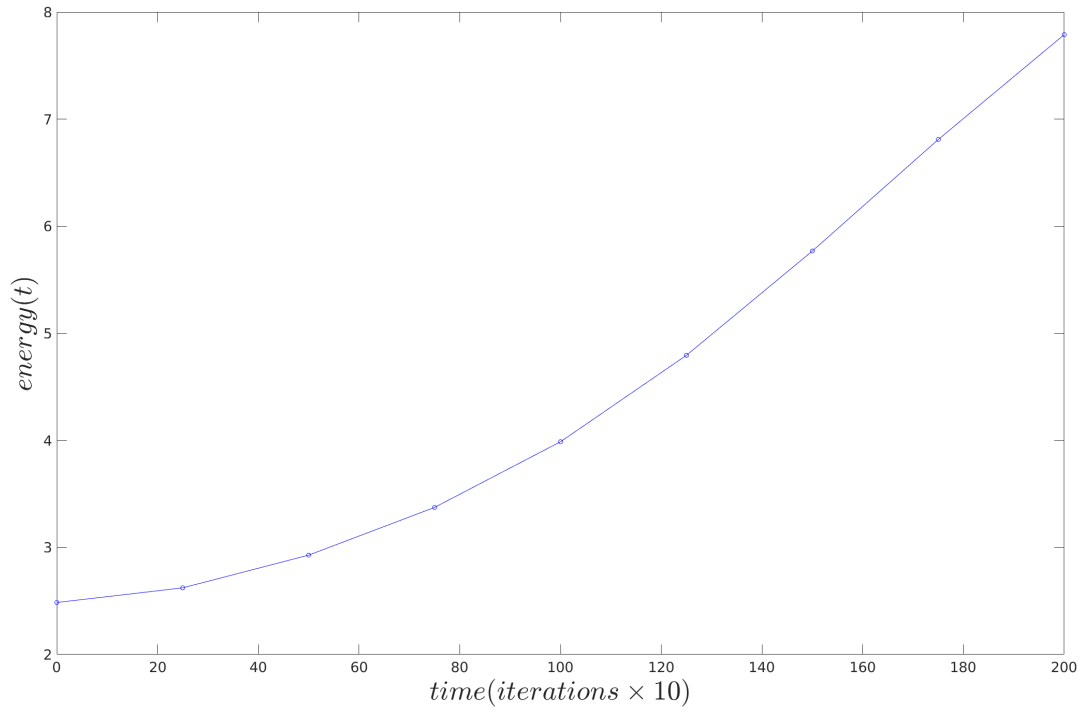
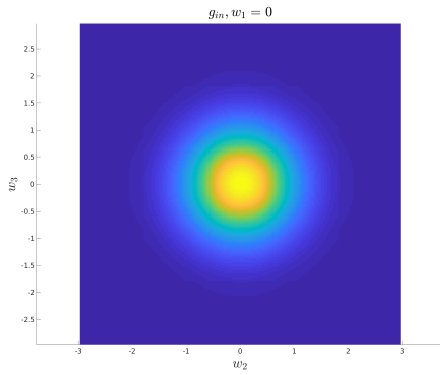
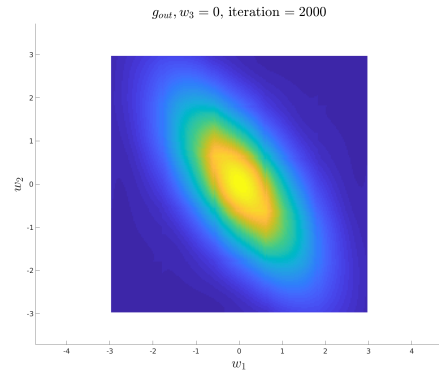


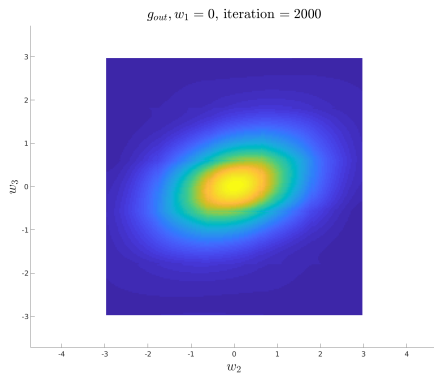
Figure 5.42: Experiment 2 with 125 Elements: Energy



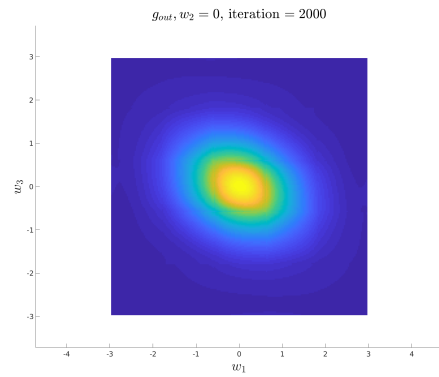
(a) Initial condition on the $w_1 = 0$ surface



(b) Converged solution on the $w_3 = 0$ surface



(c) Converged solution on the $w_1 = 0$ surface



(d) Converged solution on the $w_2 = 0$ surface

Figure 5.43: Experiment 2 with 125 Elements: Input and output on different surfaces

Since we apply shear in three directions in this simulation, we observe directional growth of the velocity distribution function on all three planes $w_1 = 0$, $w_2 = 0$, and $w_3 = 0$.

5.5 Vortex-like Structure

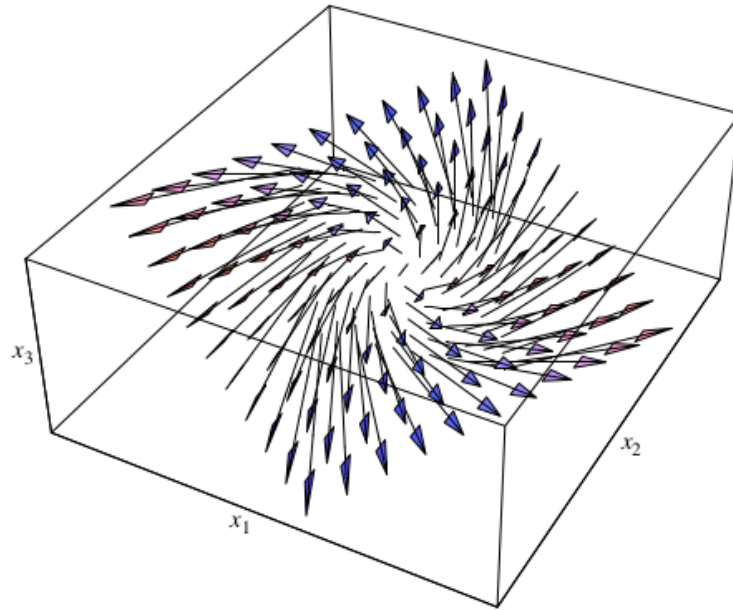


Figure 5.44: Vortex like structures. The values of the parameters are $\alpha = -1.3, v_1 = 1.3, v_3 = 0.7$. The velocity field on the plane $x_2 = \text{const}$ is shown, and this velocity field is independent of x_2 . The line perpendicular to this plane passing through the centre of this structure is a line of zero velocity. (from Dayal & James[15])

Another kind of flow that could be described using universal flows for incompressible fluids with (5.4.0.2), is vortex §4.3.2 [15]. Figure 5.44 is a view observed from a direction $(1.3, -2.4, 2)$. As it has been described by all standard definitions, this flow is disqualified to be called a vortex, although it is a limiting case of a vortex, excepting the M_z criterion [23]. In this experiment we simulate a vortex-like structure as shown in Figure 5.44 with the same dimensionless shear strain rates. The expression for $\nabla \mathbf{v}$ could be with simple computation,

$$\nabla \mathbf{v} = \begin{pmatrix} 0 & 0 & \alpha \\ v_1 & 0 & v_2 - \alpha v_1 t \\ 0 & 0 & 0 \end{pmatrix} \quad (5.5.0.1)$$

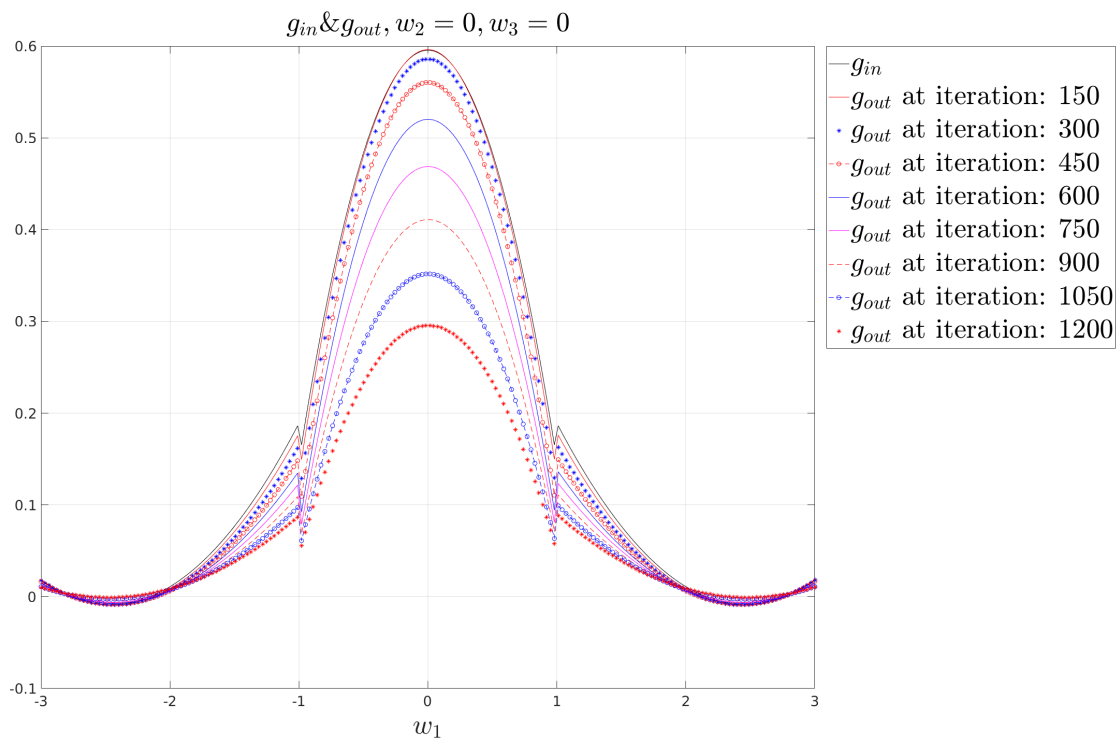


Figure 5.45: Experiment 3 with 27 Elements: Evolution of g with $w_2 = w_3 = 0$

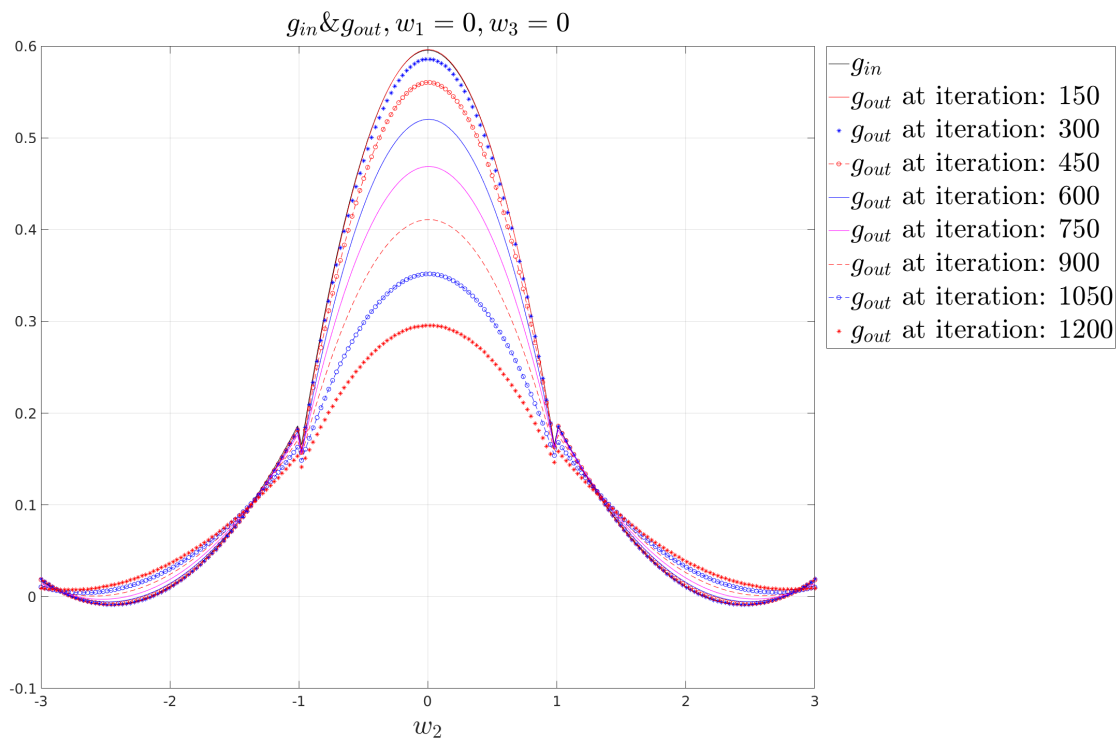


Figure 5.46: Experiment 3 with 27 Elements: Evolution of g with $w_1 = w_3 = 0$

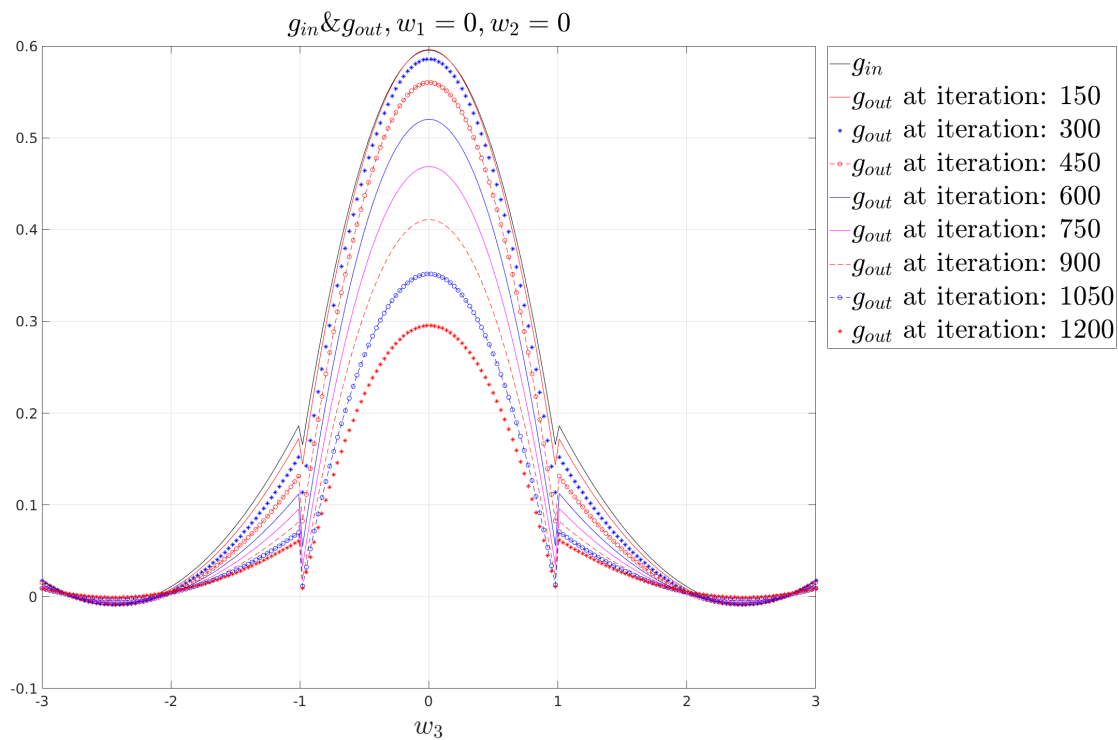


Figure 5.47: Experiment 3 with 27 Elements: Evolution of g with $w_1 = w_2 = 0$

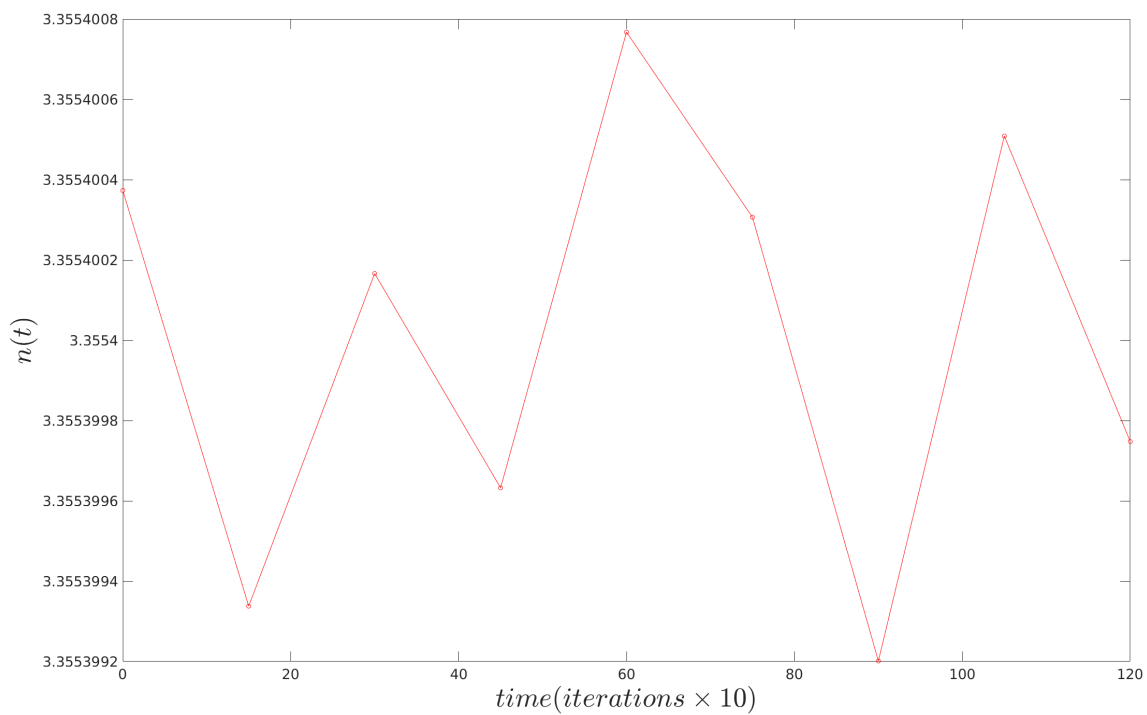


Figure 5.48: Experiment 3 with 27 Elements: Number Density

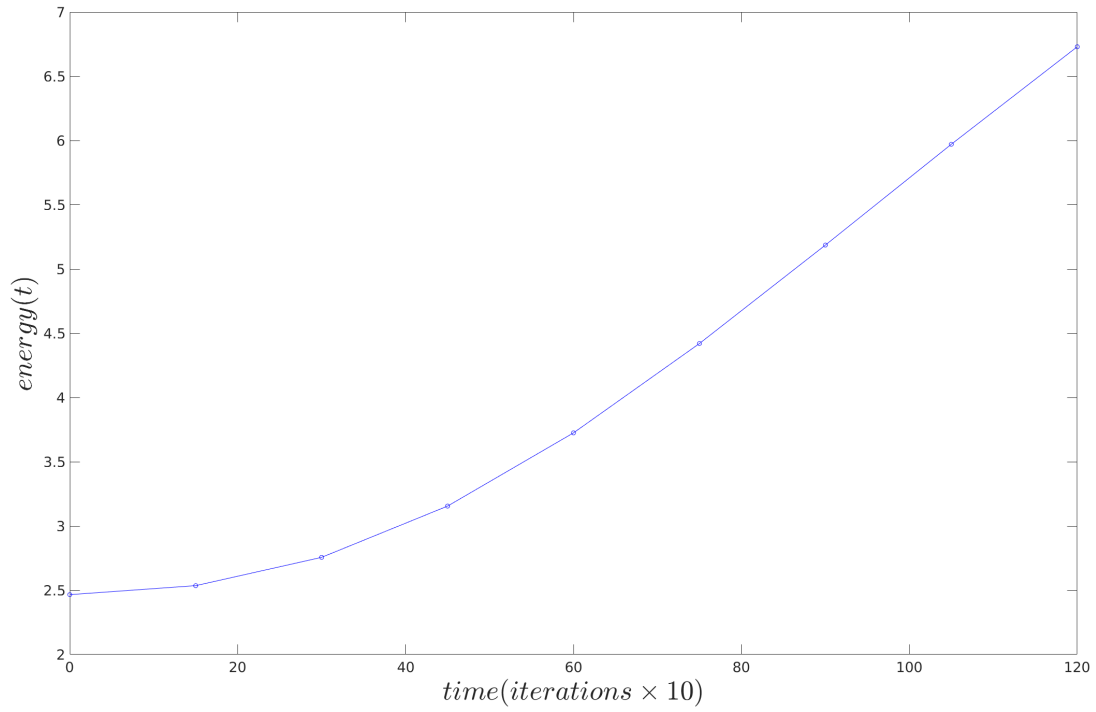
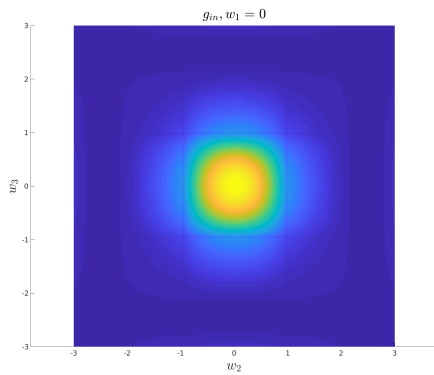
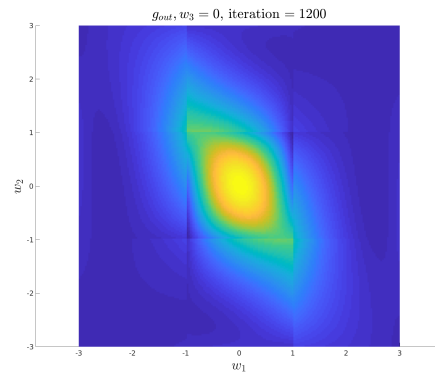


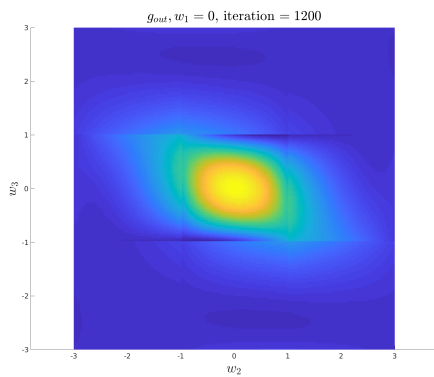
Figure 5.49: Experiment 3 with 27 Elements: Energy



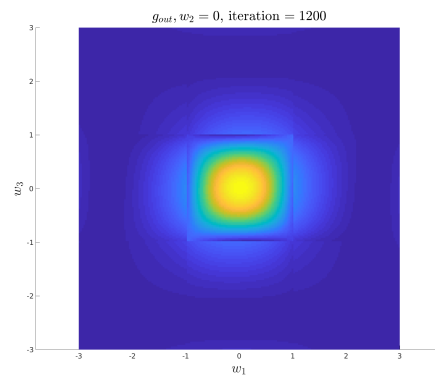
(a) Initial condition on the $w_1 = 0$ surface



(b) Converged solution on the $w_3 = 0$ surface



(c) Converged solution on the $w_1 = 0$ surface



(d) Converged solution on the $w_2 = 0$ surface

Figure 5.50: Experiment 3 with 27 Elements: Input and output on different surfaces

This experiment with 5 elements:

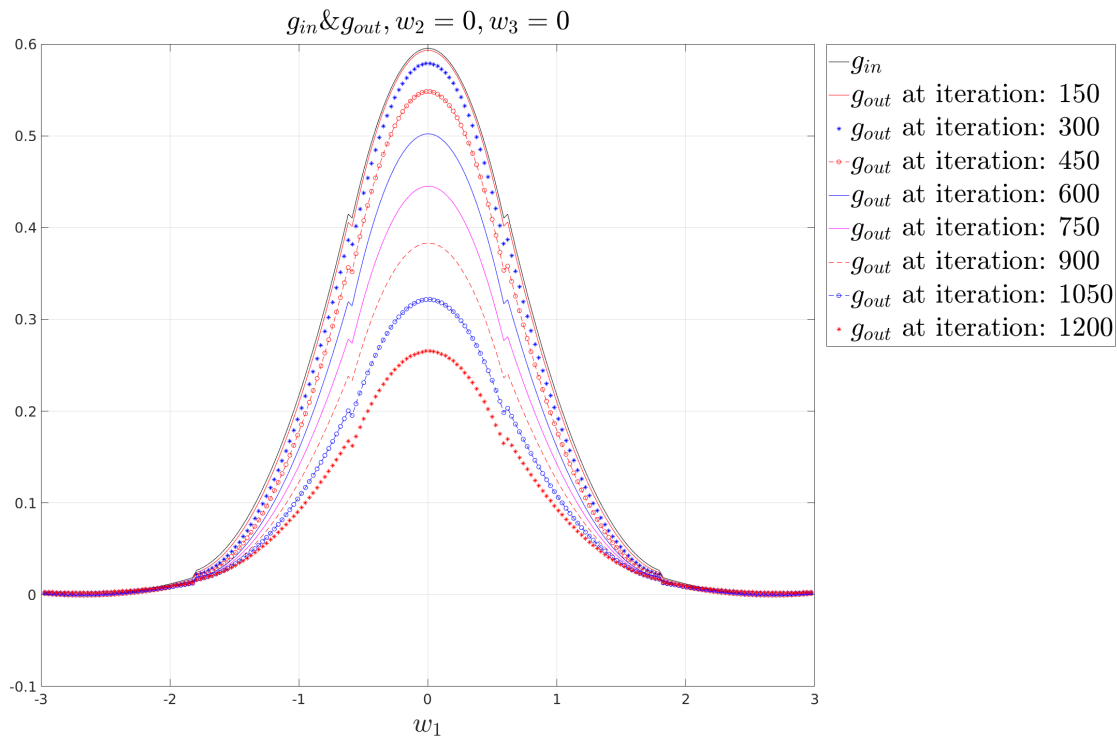


Figure 5.51: Experiment 3 with 125 Elements: Evolution of g with $w_2 = w_3 = 0$

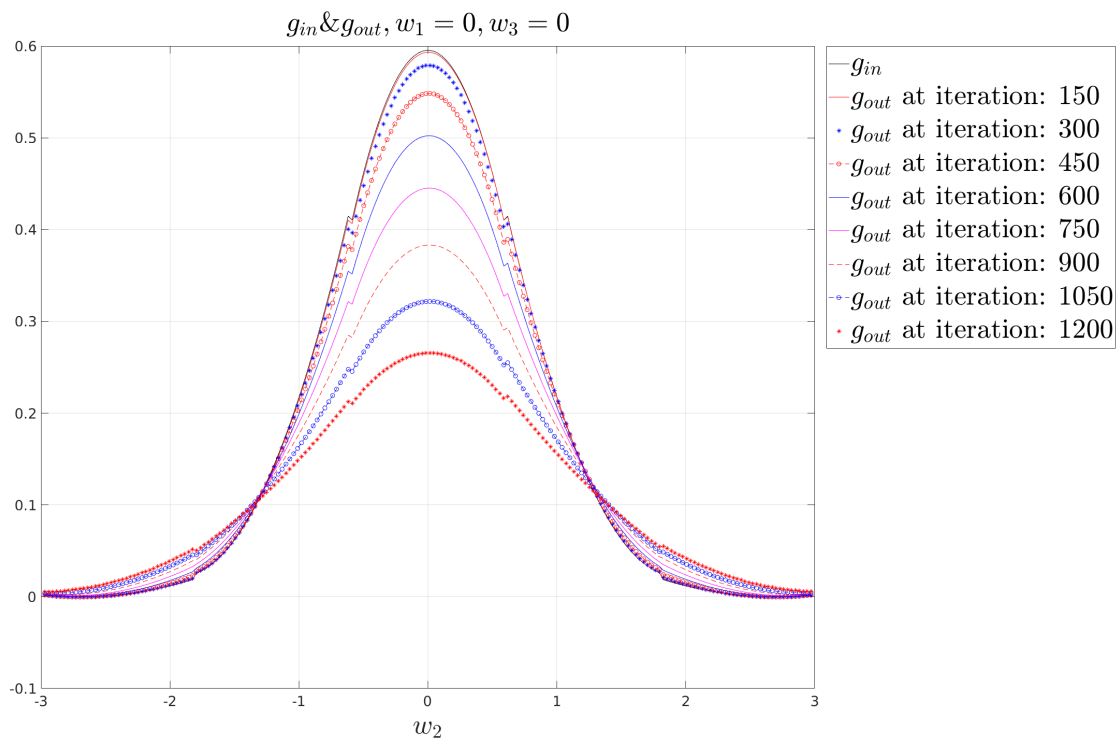


Figure 5.52: Experiment 3 with 125 Elements: Evolution of g with $w_1 = w_3 = 0$

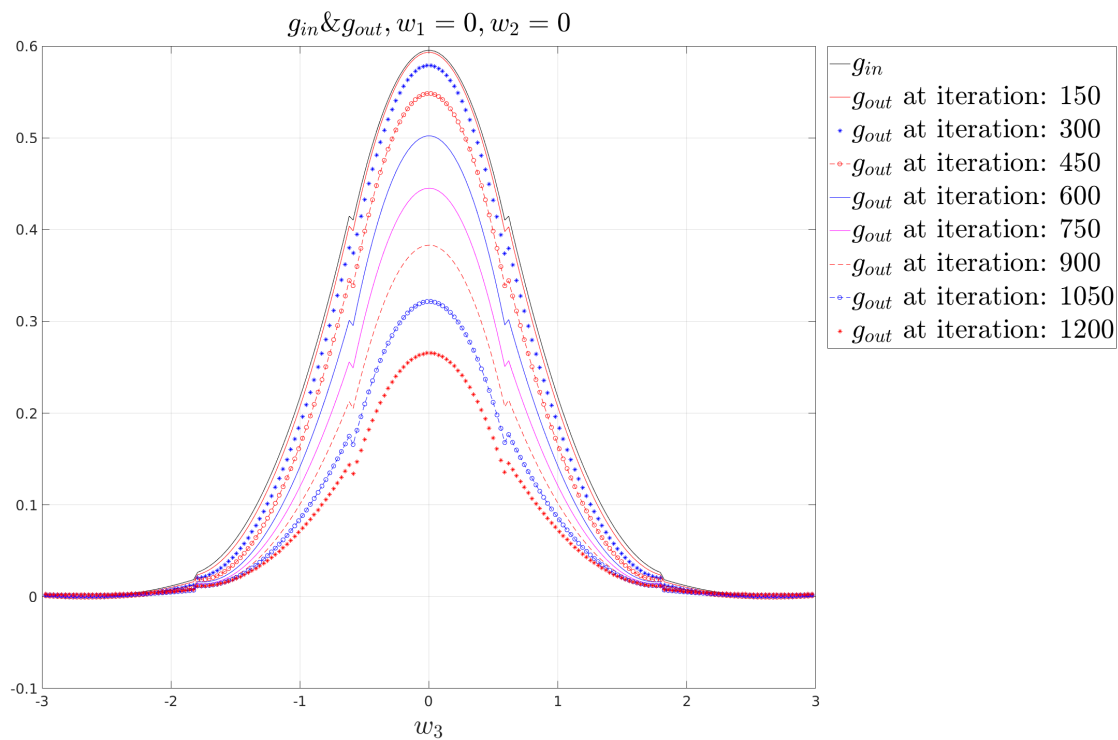


Figure 5.53: Experiment 3 with 125 Elements: Evolution of g with $w_1 = w_2 = 0$

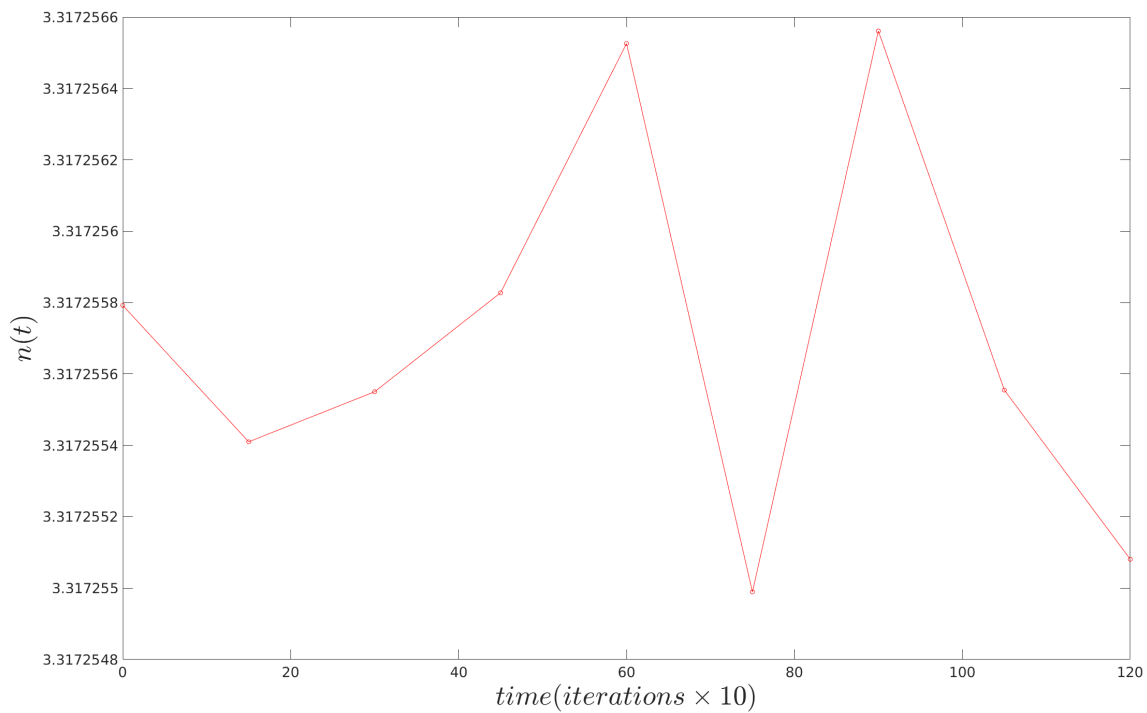


Figure 5.54: Experiment 3 with 125 Elements: Number Density

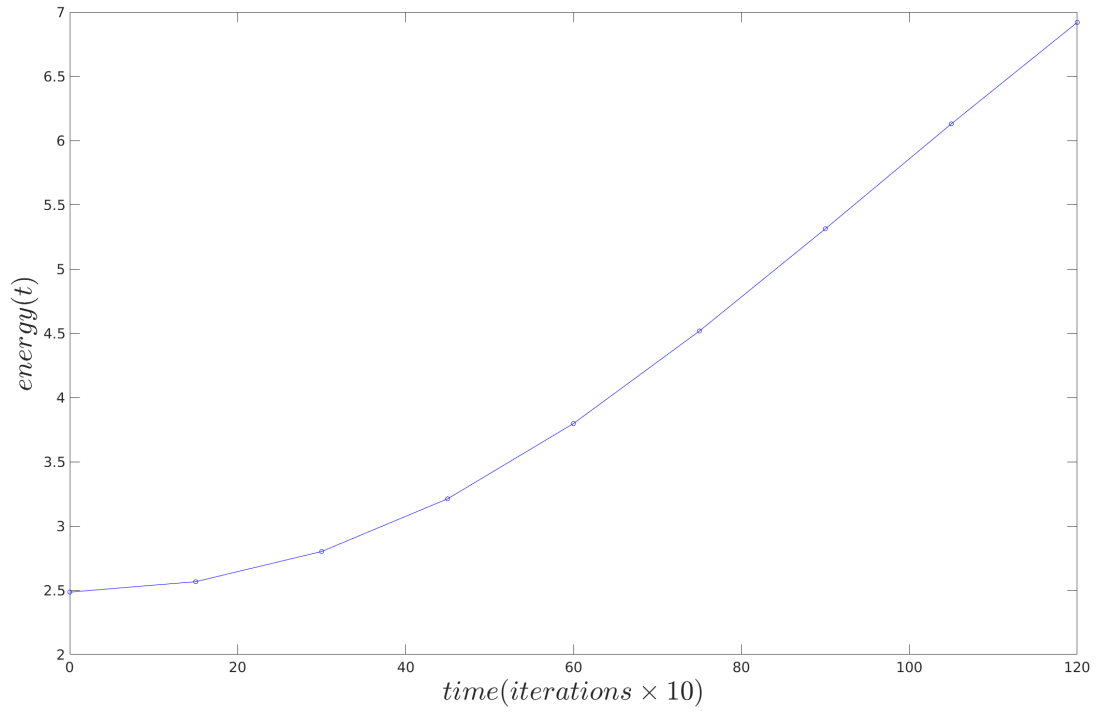
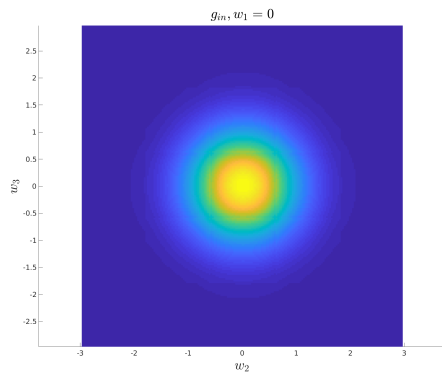
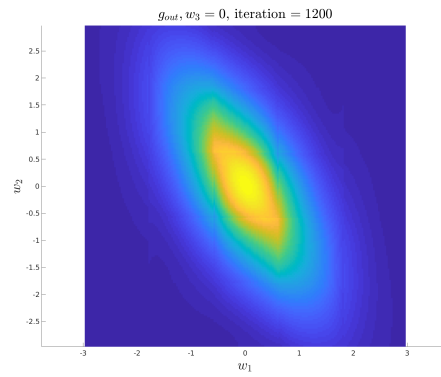


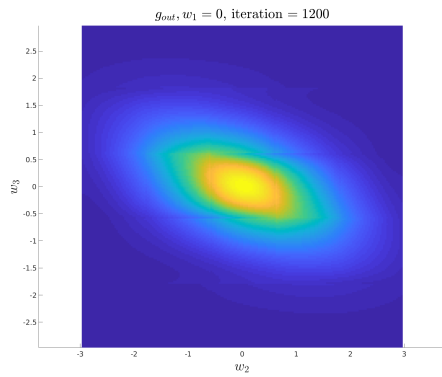
Figure 5.55: Experiment 3 with 125 Elements: Energy



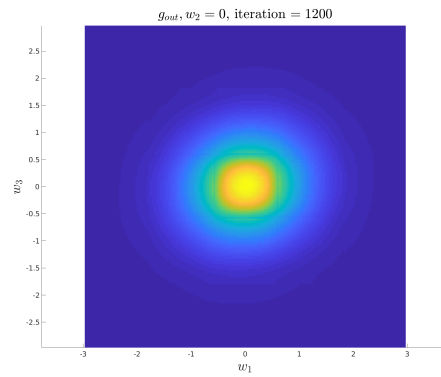
(a) Initial condition on the $w_1 = 0$ surface



(b) Converged solution on the $w_3 = 0$ surface



(c) Converged solution on the $w_1 = 0$ surface



(d) Converged solution on the $w_2 = 0$ surface

Figure 5.56: Experiment 3 with 125 Elements: Input and output on different surfaces

5.6 Parallelization Scaling

All the non-equilibrium simulations we have run were parallelised using OpenMP with 28 processors on Pittsburgh Supercomputing Center. The computation of the forcing vector $\psi_j(t, \mathbf{g}(t))$ in (3.3.2.1) is parallelized with OpenMP. Since we use an explicit method, the bottle-neck of our simulations is the computationn of $\psi_j(t, \mathbf{g}(t))$ at every time-step. We obtain excellent parallelization efficiency. It is almost linear upto 28 processor.

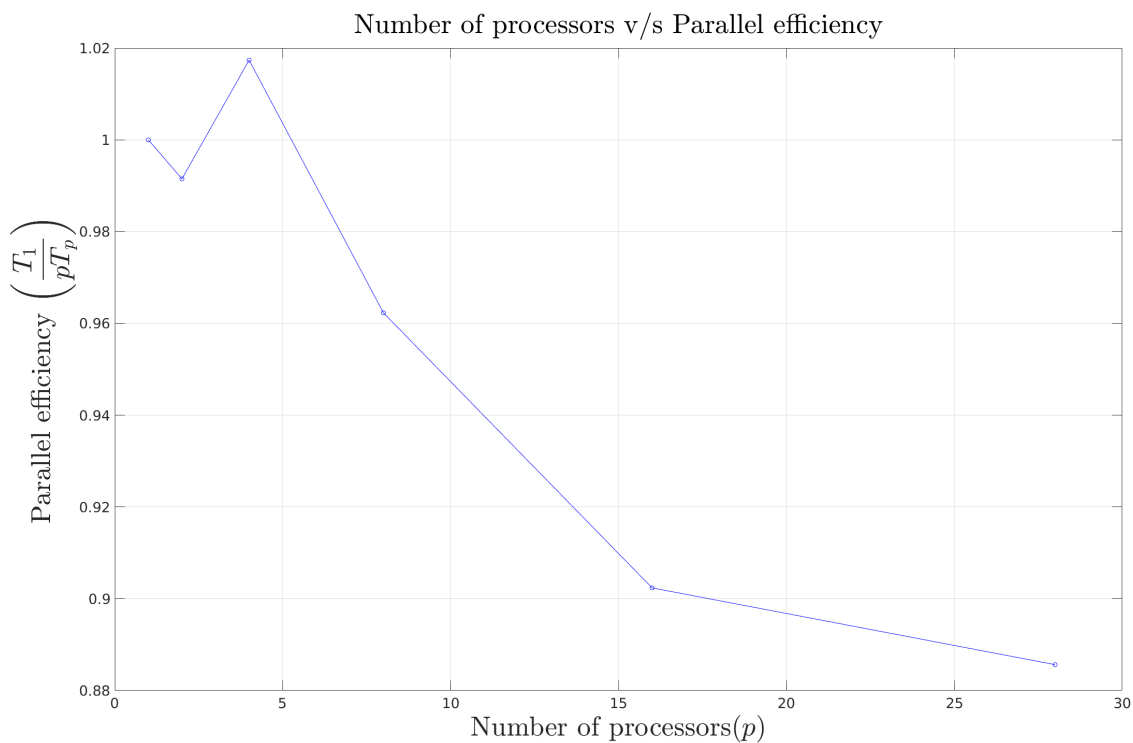


Figure 5.57: Efficiency

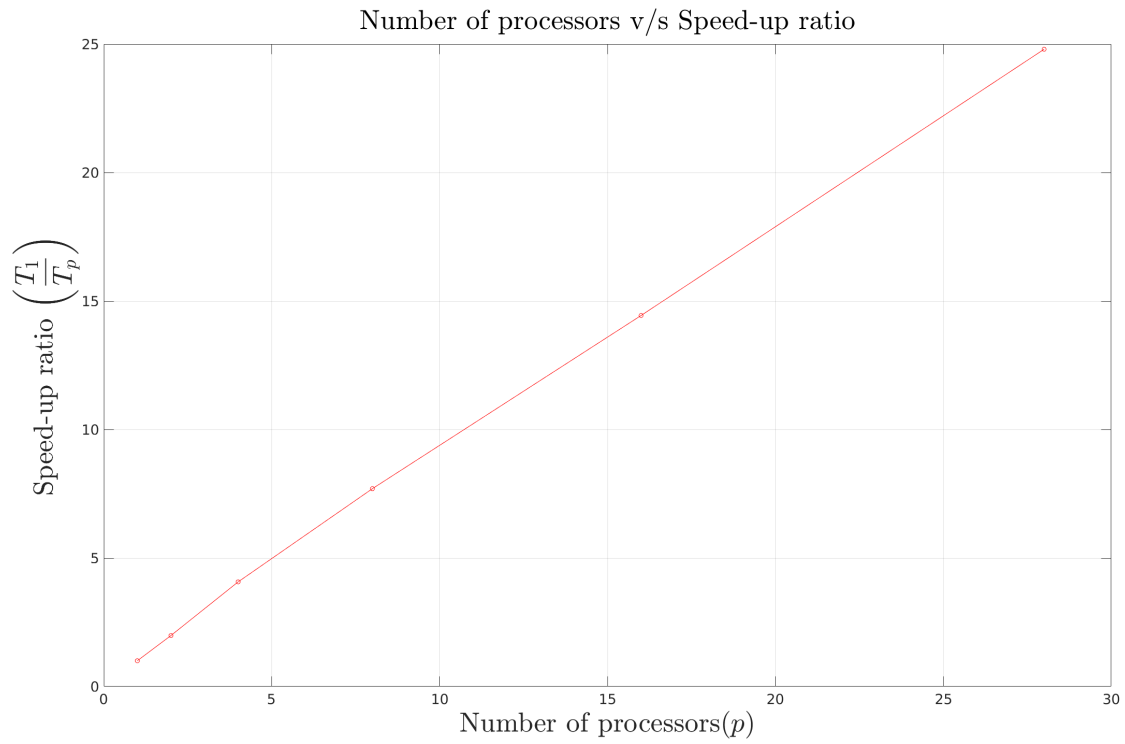


Figure 5.58: Speed Up

5.7 Discussion

- A big limitation of the simulation that we have performed with the Boltzmann equation is domain truncation. Our simulation gas needs to have a temperature low enough so that it does not reach the boundary of the translated velocity domain we have considered in our calculations. In the above experiments, all the simulations were run until the velocity distribution function g reached the edges of our truncated domain. Beyond that point, the simulation starts to produce spurious results. The solution and the energy of the particles start converging even though energy is being supplied to the system constantly. The constraint on the number density in the form of Lagrange multiplier at every time step might be the reason why this happens. However, all our observations and results illustrated above are only upto to the point until the solution reaches the truncated boundary of our translated velocity domain.
- We could compute the collision operator for 27 and 125 elements only and thus have run our experiments for these two cases only. Mesh refinement in every experiment has smoothed our solution as expected and they are in close agreement with each other.
- The energy rise patterns in the molecular dynamics and the simulation with Boltzmann equation are in agreement only with an introduction of a viscous damping in the molecular dynamics simulation. The simulations done in the verification experiments are implemented with an imposition of constraints on number density, momentum, and energy with the help of the Lagrange multiplier method. In case of the non-equilibrium simulations, we want to observe a rise in the total energy since we are adding it in the form of shear force and hence they are not constrained but the number density, which is possibly why we observe a lossy energy curve in the Boltzmann simulation as compared to the molecular dynamics ones. Mesh refinement could be a possible method of improving the solution with Boltzmann simulation as we observe the 125 element simulation is a bit closer to the LAMMPS solution as compared to the 27 element solution. Improving the accuracy of the collision operator would be able to conserve the different moments of the velocity distribution function, which would prevent the leakage of energy. A development

of a better algorithm to compute the Collision Operator more accurately is a proposal of future work to improve the results that we have observed.

Chapter 6

Appendix

6.1 Symmetry property of The Collision Operator

The collision integral appearing on the right of the Boltzmann equation :

$$J(t, x, v) = \int (f' f'_* - f f_*) g b \, db \, d\epsilon \, dv_* \quad (6.1.0.1)$$

where $g = \mathbf{v} - \mathbf{v}_*$. This function $J(t, x, v)$ is often integrated with a weighting function of velocity $\phi(v)$:

$$I_\phi = \int \phi(v) J(t, x, v) \, dv = \int \phi(v) (f' f'_* - f f_*) g b \, db \, d\epsilon \, dv_* \, dv \quad (6.1.0.2)$$

This integral is equal to

$$I_\phi = I_{\phi'} = \int \phi(v') (f_* f - f'_* f') g' b' \, db' \, d\epsilon' \, dv'_* \, dv' \quad (6.1.0.3)$$

Now, by the assumption that the potential of the molecules is spherically symmetric it can be stated that $g = g', b = b', \epsilon = \epsilon'$ where primes denote the post collisional properties. Also by the conservation

of phase volume $dv dv_* = dv' dv'_*$, $I_{\phi'}$ may be written as:

$$I_{\phi'} = - \int \phi(v') (f'_* f' - f_* f) gb db d\epsilon dv_* dv \quad (6.1.0.4)$$

On adding equations (6.1.0.2) and (6.1.0.4) we get,

$$I_{\phi} = \frac{1}{2} \int (\phi - \phi') (f'_* f' - f_* f) gb db d\epsilon dv_* dv \quad (6.1.0.5)$$

The integral (6.1.0.1) is symmetrical w.r.t. v and v_* . Thus,

$$\begin{aligned} I_{\phi_*} &= \int \phi(v_*) J(t, x, v_*) dv_* = I_{\phi} \\ &= \frac{1}{2} \int (\phi_* - \phi'_*) (f'_* f' - f_* f) gb db d\epsilon dv_* dv \end{aligned} \quad (6.1.0.6)$$

On adding equations (6.1.0.5) and (6.1.0.6) we get,

$$I_{\phi} = \frac{1}{4} \int (\phi + \phi_* - \phi' - \phi'_*) (f'_* f' - f_* f) gb db d\epsilon dv_* dv \quad (6.1.0.7)$$

From symmetry properties we obtain the relations :

$$\int (\phi_* - \phi'_*) f_* f gb db d\epsilon dv_* dv = \int (\phi'_* - \phi_*) f'_* f' g'b' db' d\epsilon' dv'_* dv' \quad (6.1.0.8)$$

and

$$\int (\phi + \phi_* - \phi' - \phi'_*) f_* f gb db d\epsilon dv_* dv = \int (\phi' + \phi'_* - \phi - \phi_*) f'_* f' g'b' db' d\epsilon' dv'_* dv' \quad (6.1.0.9)$$

Now substituting (6.1.0.8) and (6.1.0.9) into (6.1.0.5) and (6.1.0.7), respectively, using the properties of spherically symmetric potential and conservation of phase volume we obtain :-

$$I_{\phi} = \int (\phi'_* - \phi_*) f_* f gb db d\epsilon dv_* dv \quad (6.1.0.10)$$

and

$$I_\phi = \frac{1}{2} \int (\phi' + \phi'_* - \phi - \phi_*) (f'_* f' - f_* f) g b \, db \, d\epsilon \, dv_* \, dv \quad (6.1.0.11)$$

6.2 Notation

\mathbf{v}	Velocity vector
\mathbf{x}	Position vector
t	Time
f	Probability distribution of particles with velocity \mathbf{v} at \mathbf{x}
f_*	Probability distribution of particles with velocity \mathbf{v}_* at \mathbf{x}
f'	Post-collision probability distribution of particles with velocity \mathbf{v} at \mathbf{x}
f'_*	Post-collision probability distribution of particles with velocity \mathbf{v}_* at \mathbf{x}
\mathbf{w}	Translated velocity field
g	Molecular density function at translated velocity field \mathbf{w}
g_*	Molecular density function at translated velocity field \mathbf{w}_*
g'	Post-collision Molecular density function at translated velocity field \mathbf{w}
g'_*	Post-collision Molecular density function at translated velocity field \mathbf{w}_*
S	Unit sphere for integration
\mathbf{A}	Linear transformation of matrix deciding the motion in fluid
ω, ω	Velocity and Speed of approach of particles respectively
d	Diameter of particles
θ	Polar angle for integration over spherical surface
ζ	Azimuthal angle for integration over spherical surface
\mathbf{e}	Unit vector perpendicular to the spherical surface of integration
b	Distance of closest approach of the undisturbed trajectories in the center of mass reference-frame
b_*	Maximum distance of approach
\mathbf{w}_a	Velocity of center of mass of the particles with velocities \mathbf{w} and \mathbf{w}_*
β	The projection of ω on the $w_1 - w_2$ plane
ρ_0	Reference number density of gas
t_0	Reference time
v_0	Reference speed

T_0	Reference Temperature
d_0	diameter of gas particles
R	Universal Gas constant
λ	Mean free path of molecules
K	Non-dimensionalization constant for the Boltzmann Equation
ϕ	Shape functions
s	Total number of shape functions
K_j	j^{th} shape function
$[\alpha_L^j, \alpha_R^j]$	Interval in w_1 -direction for the j^{th} element
$[\gamma_L^j, \gamma_R^j]$	Interval in w_2 -direction for the j^{th} element
$[\delta_L^j, \delta_R^j]$	Interval in w_3 -direction for the j^{th} element
$\kappa_p^{j;1}$	p^{th} node of the j^{th} element in the w_1 -direction
$\kappa_q^{j;2}$	q^{th} node of the j^{th} element in the w_2 -direction
$\kappa_r^{j;3}$	r^{th} node of the j^{th} element in the w_3 -direction
$\varphi_l^{j;1}$	Lagrange basis function at the l^{th} node along w_1 -direction in the j^{th} element
$\varphi_m^{j;2}$	Lagrange basis function at the m^{th} node along w_2 -direction in the j^{th} element
$\varphi_n^{j;3}$	Lagrange basis function at the n^{th} node along w_3 -direction in the j^{th} element
s_1, s_2, s_3	Number of nodes in the w_1, w_2 and w_3 directions respectively for the entire domain
$\Delta \mathbf{w}^j$	Volume of the j^{th} element
ξ_p	3-dimensional Gauss quadrature weight for p^{th} node
$\xi_l^{s_1}$	1-dimensinal Gauss quadrature weight for l^{th} node of order s_1
$\xi_m^{s_2}$	1-dimensinal Gauss quadrature weight for m^{th} node of order s_2
$\xi_n^{s_3}$	1-dimensinal Gauss quadrature weight for n^{th} node of order s_3
δ_{pq}	Kronecker delta
h	Test function for the numerical approximation
M_i	Part of the Collision operator to be integrated over the spherical surface
F_i	i^{th} equation of the discretized Collision operator
$\mathbf{w}^j, \mathbf{w}_*^k$	j^{th} and k^{th} Gauss quadrature points for integration in \mathbf{w} and \mathbf{w}_*

ψ_j	RHS for the j^{th} equation for time-stepping
\mathbf{l}_i	orthonormal basis
α, v_i	coefficients determining the characteristics of incompressible flow
\mathcal{F}	approximate solution function
Φ	collisionn invariants
\mathbf{Q}	constraint matrix
\mathbf{F}_c	minimizer of the problem to preserve moments
\mathcal{L}	objective function for the minimization problem
Λ	Lagrange multiplier vector
\mathbf{D}	differential operator
$\hat{\Omega}$	chosen function for manufactured solution with sufficient differentiability, satisfying boundary, and initial conditions
\mathbf{S}_Ω	source term manufactured because of assumed solution

Bibliography

- [1] Alekseenko, A. (2011). Numerical properties of high order discrete velocity solutions to the bgk kinetic equation. *Applied Numerical Mathematics*, 61(4):410–427.
- [2] Alekseenko, A., Gimelshein, N., and Gimelshein, S. (2012). An application of discontinuous galerkin space and velocity discretisations to the solution of a model kinetic equation. *International Journal of Computational Fluid Dynamics*, 26(3):145–161.
- [3] Alekseenko, A. and Josyula, E. (2014). Deterministic solution of the spatially homogeneous boltzmann equation using discontinuous galerkin discretizations in the velocity space. *Journal of Computational Physics*, 272:170–188.
- [4] Aristov, V. (2001). Methods of direct solving the boltzmann equation and study of non-equilibrium.
- [5] Aristov, V. V. (2012). *Direct methods for solving the Boltzmann equation and study of nonequilibrium flows*, volume 60. Springer Science & Business Media.
- [6] Bellomo, N. and Schiavo, M. L. (1997). From the boltzmann equation to generalized kinetic models in applied sciences. *Mathematical and Computer Modelling*, 26(7):43–76.
- [7] Bird, G. (1994). Molecular gas dynamics and the direct simulation monte carlo of gas flows. *Clarendon, Oxford*, 508:128.
- [8] Biswas, R., Devine, K. D., and Flaherty, J. E. (1994). Parallel, adaptive finite element methods for conservation laws. *Applied Numerical Mathematics*, 14(1-3):255–283.
- [9] Boltzmann, L. (1974). On a thesis of schopenhauer’s. In *Theoretical Physics and Philosophical Problems*, pages 185–198. Springer.
- [10] Burden, R. L., Faires, J. D., et al. (2001). Numerical analysis.
- [11] Cercignani, C. (1995). Aerodynamical applications of the boltzmann equation. *La Rivista del Nuovo Cimento (1978-1999)*, 18(7):1–40.

- [12] Chapman, S., Cowling, T. G., and Burnett, D. (1990). *The mathematical theory of non-uniform gases: an account of the kinetic theory of viscosity, thermal conduction and diffusion in gases*. Cambridge university press.
- [13] Coleman, B. D., Markovitz, H., and Noll, W. (2012). *Viscometric flows of non-Newtonian fluids: theory and experiment*, volume 5. Springer Science & Business Media.
- [14] Dayal, K. and James, R. D. (2010). Nonequilibrium molecular dynamics for bulk materials and nanostructures. *Journal of the Mechanics and Physics of Solids*, 58(2):145–163.
- [15] Dayal, K. and James, R. D. (2012). Design of viscometers corresponding to a universal molecular simulation method. *Journal of Fluid Mechanics*, 691:461–486.
- [Dayal et al.] Dayal, K., James, R. D., and Elliott, R. Objective formulas (in preperation).
- [17] Filbet, F., Mouhot, C., and Pareschi, L. (2006). Solving the boltzmann equation in $n \log^2 n$. *SIAM Journal on Scientific Computing*, 28(3):1029–1053.
- [18] Filbet, F. and Russo, G. (2003). High order numerical methods for the space non-homogeneous boltzmann equation. *Journal of Computational Physics*, 186(2):457–480.
- [19] Gamba, I. M. and Tharkabhushanam, S. H. (2009). Spectral-lagrangian methods for collisional models of non-equilibrium statistical states. *Journal of Computational Physics*, 228(6):2012–2036.
- [20] Gamba, I. M. and Tharkabhushanam, S. H. (2010). Shock and boundary structure formation by spectral-lagrangian methods for the inhomogeneous boltzmann transport equation. *Journal of Computational Mathematics*, pages 430–460.
- [21] Gustafsson, B., Kreiss, H.-O., and Olinger, J. (1995). *Time dependent problems and difference methods*, volume 24. John Wiley & Sons.
- [22] Haack, J. R. and Gamba, I. M. (2012). High performance computing with a conservative spectral boltzmann solver. In *AIP Conference Proceedings*, volume 1501, pages 334–341. AIP.
- [23] Haller, G. (2005). An objective definition of a vortex. *Journal of fluid mechanics*, 525:1–26.

- [24] Hesthaven, J. S. and Warburton, T. (2007). *Nodal discontinuous Galerkin methods: algorithms, analysis, and applications*. Springer Science & Business Media.
- [25] Huang, K. (1967). *Statistical mechanics*. John Wiley & Sons.
- [26] Hughes, T. J. (2012). *The finite element method: linear static and dynamic finite element analysis*. Courier Corporation.
- [27] James, R. D. (2006). Objective structures. *Journal of the Mechanics and Physics of Solids*, 54(11):2354–2390.
- [28] Kirsch, R. and Rjasanow, S. (2007). A weak formulation of the boltzmann equation based on the fourier transform. *Journal of Statistical Physics*, 129(3):483–492.
- [29] Kogan, M. (1969). Rarefied gas dynamics. *Plenum Press, New York*, 2:1.
- [30] Lees, A. and Edwards, S. (1972). The computer study of transport processes under extreme conditions. *Journal of Physics C: Solid State Physics*, 5(15):1921.
- [31] LeVeque, R. J. (2002). *Finite volume methods for hyperbolic problems*, volume 31. Cambridge university press.
- [32] Mohamad, A. A. (2011). *Lattice Boltzmann method: fundamentals and engineering applications with computer codes*. Springer Science & Business Media.
- [33] Mouhot, C. and Pareschi, L. (2004). Fast methods for the boltzmann collision integral. *Comptes Rendus Mathematique*, 339(1):71–76.
- [34] Mouhot, C. and Pareschi, L. (2006). Fast algorithms for computing the boltzmann collision operator. *Mathematics of computation*, 75(256):1833–1852.
- [35] Pareschi, L. (2003). Computational methods and fast algorithms for boltzmann equations. *SERIES ON ADVANCES IN MATHEMATICS FOR APPLIED SCIENCES*, 63:159–202.

- [36] Pareschi, L. and Perthame, B. (1996). A fourier spectral method for homogeneous boltzmann equations. *Transport Theory and Statistical Physics*, 25(3-5):369–382.
- [37] Pareschi, L. and Russo, G. (2000a). Numerical solution of the boltzmann equation i: Spectrally accurate approximation of the collision operator. *SIAM journal on numerical analysis*, 37(4):1217–1245.
- [38] Pareschi, L. and Russo, G. (2000b). On the stability of spectral methods for the homogeneous boltzmann equation. *Transport Theory and Statistical Physics*, 29(3-5):431–447.
- [39] Reed, W. H. and Hill, T. (1973). Triangular mesh methods for the neutron transport equation. Technical report, Los Alamos Scientific Lab., N. Mex.(USA).
- [40] Shunn, L. and Ham, F. (2007). Method of manufactured solutions applied to variable-density flow solvers. *Annual Research Briefs-2007, Center for Turbulence Research*, pages 155–168.
- [41] Strang, G. and Fix, G. J. (1973). *An analysis of the finite element method*, volume 212. Prentice-hall Englewood Cliffs, NJ.
- [42] Struchtrup, H. (2005). *Macroscopic transport equations for rarefied gas flows*. Springer.
- [43] Tcheremissine, F. (2006). Solution to the boltzmann kinetic equation for high-speed flows. *Computational Mathematics and Mathematical Physics*, 46(2):315–329.
- [44] Titarev, V. (2012). Efficient deterministic modelling of three-dimensional rarefied gas flows. *Communications in Computational Physics*, 12(1):162–192.
- [45] Toro, E. F. (2013). *Riemann solvers and numerical methods for fluid dynamics: a practical introduction*. Springer Science & Business Media.
- [46] Truesdell, C. and Muncaster, R. (1980). Fundamentals of maxwell’s kinetic theory of a simple monatomic gas. *Academic, New York*.
- [47] Xu, Y. and Shu, C.-W. (2010). Local discontinuous galerkin methods for high-order time-dependent partial differential equations. *Communications in Computational Physics*, 7(1):1.

[ZHANG and GAMBA] ZHANG, C. and GAMBA, I. M. A conservative discontinuous galerkin solver for homogeneous boltzmann equation.

[49] Zienkiewicz, O. and Taylor, R. (1991). The finite element method. volume 1: Basic formulation and linear problems. volume 2: Solid and uid mechanics and nonlinearity.